

Washington University in St. Louis
Washington University Open Scholarship

All Theses and Dissertations (ETDs)

January 2010

Remote Sensing and Terramechanics Study of Mars using Orbital and Rover Data Sets

Kimberly Lichtenberg
Washington University in St. Louis

Follow this and additional works at: <https://openscholarship.wustl.edu/etd>

Recommended Citation

Lichtenberg, Kimberly, "Remote Sensing and Terramechanics Study of Mars using Orbital and Rover Data Sets" (2010). *All Theses and Dissertations (ETDs)*. 203.
<https://openscholarship.wustl.edu/etd/203>

This Dissertation is brought to you for free and open access by Washington University Open Scholarship. It has been accepted for inclusion in All Theses and Dissertations (ETDs) by an authorized administrator of Washington University Open Scholarship. For more information, please contact digital@wumail.wustl.edu.

WASHINGTON UNIVERSITY IN ST. LOUIS

Department of Earth and Planetary Sciences

Dissertation Examination Committee:

Raymond Arvidson, Chair

Jeffrey Catalano

David Fike

Charles Hohenberg

Kenneth Kelton

Randy Korotev

REMOTE SENSING AND TERRAMECHANICS STUDY OF MARS USING
ORBITAL AND ROVER DATA SETS

by

Kimberly Ann Lichtenberg

A dissertation presented to the
Graduate School of Arts and Sciences
of Washington University in
partial fulfillment of the
requirements for the degree
of Doctor of Philosophy

May 2010

Saint Louis, Missouri

Copyright by
Kimberly Ann Lichtenberg
2010

ABSTRACT OF THE DISSERTATION

Remote Sensing and Terramechanics Study of Mars

using Orbital and Rover Data Sets

by

Kimberly Ann Lichtenberg

Doctor of Philosophy in Earth and Planetary Sciences

Washington University in St. Louis, 2010

Professor Raymond Arvidson, Chairperson

Orbital observations, rover-based remote-sensing and in-situ observations, and terramechanics modeling can be used collaboratively to examine the interplay between material properties, scientific setting, and mobility issues facing rovers on other worlds. In this thesis, these types of observations are used concurrently to identify the surface properties on a regional scale for the Gusev Crater Spirit landing site, to understand how the rover interacted with these materials while driving, and as a look ahead to a candidate new landing site, Aram Chaos, with exposed materials that contain key evidence for past environmental conditions.

Comparison of rover-based and orbital spectral reflectance data over Spirit's traverses show that cratered plains in Gusev Crater are dominated by nanophase ferric-oxide-rich dust covering weakly altered basaltic sands. Comparison of Mars Odyssey THEMIS-derived thermal inertia values with Mars Express OMEGA-derived spectral parameters shows that although the dust cover can be optically thick (0.4 to 2.5 μm

wavelength region) in some areas, it is not thick enough (~1 cm) to mask the thermal inertia of the underlying substrate.

Mobility in the above materials with a five-wheeled rover—Spirit's right front drive actuator is non-functioning—is analyzed in a modeling environment to assess mobility issues facing current and future rovers, specifically how to minimize the effect of an inoperable wheel on rover mobility and determining the rolling resistance of an embedded rover. This includes generation and use of mobility hazard maps as a tactical planning tool.

A detailed stratigraphic and mineralogical description of a candidate new landing site, Aram Chaos (~3°N, 339°E), is presented based on orbital data primarily from the Mars Reconnaissance Orbiter. Two sedimentary units overlie the basement chaos material representing the original plains fill in Aram Crater: the first and oldest is comprised of ferric hydroxysulfate intercalated with monohydrated-sulfate-bearing materials, monohydrated sulfates, and a capping unit with nanophase ferric oxides and monohydrated sulfates. After a period of wind erosion, these deposits were partially and unconformably covered by the second sedimentary unit, a discontinuous unit containing crystalline hematite and polyhydrated sulfate material. These sedimentary deposits were formed by evaporite deposition during at least two distinct rising groundwater episodes fed by regional-scale recharge.

ACKNOWLEDGEMENTS

Many thanks to my advisor, R. E. Arvidson, for his excellent guidance and mentoring. The McDonnell Center for Space Sciences provided support through a McDonnell Center Fellowship and funding was also provided by NASA through the MER project. Thanks also to the OMEGA and CRISM teams for their collaboration and my use of data from those instruments. I'd also like to thank friends both near and far, my Mom and Dad for all their support, and last but not least Kristin and Scott, without whom I'd probably still be working on this thesis.

TABLE OF CONTENTS

Abstract	ii
Acknowledgements	iv
List of Figures	vi
List of Tables	viii
Chapter 1—Introduction	1
Figures	5
Tables	8
References	11
Chapter 2—Coordinated Analyses of Orbital and Spirit Rover Data to Characterize Surface Materials on the Cratered Plains of Gusev Crater, Mars	12
2.1 Introduction	12
2.2 Previous Work	13
2.3 Comparison of OMEGA and Pancam Spectra From 0.4 to 1.0 Micrometers	16
2.4 Analysis of OMEGA Spectra Covering 0.4 to 2.5 Micrometers	21
2.5 Combined Analysis of Spectral and Thermophysical Properties	23
2.6 Conclusions	25
Figures	26
Tables	42
References	44
Chapter 3—Rover Mobility: A Modeling Perspective	56
3.1 Introduction	56
3.2 Spirit Mobility	57
3.3 Modeling and Application to Mobility	59
3.3.1 Modeling Software: MSC Adams	60
3.3.2 Wheel-Soil Contact	60
3.3.3 Assessing Impaired Mobility with Spirit	62
3.4 Spirit’s Embedding in Troy	63
3.5 Looking Forward	64
Figures	66
Tables	81
References	82
Chapter 4—Stratigraphy of Hydrated Sulfates in the Sedimentary Deposits of Aram Chaos, Mars	85
4.1 Introduction	85
4.2 Geologic setting	86
4.3 Methodology	87
4.3.1 Orbital Datasets	87
4.3.2 Laboratory Measurements	91
4.4 Stratigraphy and Mineralogy of Sedimentary Deposits	93
4.4.1 Ferric Hydroxysulfate, Monohydrated Sulfate, and Nanophase Ferric Oxide Unit	93
4.4.2 Polyhydrated Sulfates, Hydrated Materials, and Hematite Deposits	97
4.5 Summary and Implications	99
Figures	101
Tables	119
References	122

LIST OF FIGURES

Figure 1.1	Diagram of the Mars Exploration Rover	5
Figure 1.2	Pancam images of Spirit wheel tracks.....	6
Figure 1.3	Pancam image of Spirit wheel tracks in a poor mobility situation.....	7
Figure 2.1	Footprints of OMEGA data coverage.....	26
Figure 2.2	False-color mosaic of OMEGA data	27
Figure 2.3	Navcam image from Sol 127 looking west	28
Figure 2.4	Locations of Spirit Pancam 13-filter foreground stares	30
Figure 2.5	Pancam foreground stare from Sol 128.....	31
Figure 2.6	Pancam false-color images p2556 and p2574	32
Figure 2.7	DISORT-retrieved Lambert Albedos	33
Figure 2.8	Pancam R* with OMEGA Lambert Albedos	34
Figure 2.9A	OMEGA VNIR and C data from orbit 24	35
Figure 2.9B	OMEGA VNIR and C data from orbit 72	36
Figure 2.9C	OMEGA VNIR and C data from orbit 976	37
Figure 2.9D	OMEGA VNIR and C data from orbit 1313	38
Figure 2.10	Images of thermal inertia from THEMIS and TES data.....	39
Figure 2.11	Thermal inertia, spectral slope, and BD530c band depth vs. 1.01- μ m albedo	41
Figure 3.1	Map of Spirit's traverse from landing through sol 2158	67
Figure 3.2	Pancam images of Spirit wheel tracks.....	68
Figure 3.3	HiRISE image with Spirit's path from the Winter Haven 3	69
Figure 3.4	Navcam showing the disturbed area "Edmund Hamilton".....	70
Figure 3.5	Navcam from sol 1869 showing Scamander Crater	71
Figure 3.6	Example of a Hazard Map.....	72
Figure 3.7	Model of MER in Adams/View	73
Figure 3.8	Stribeck curve.....	74
Figure 3.9	Normal forces on the right-front wheel.....	75
Figure 3.10	Frictional forces on the right-front wheel.....	76
Figure 3.11	Topographic map for the Scamander Crater area.....	77
Figure 3.12	Front Hazcam showing the severity of embedding in Troy	78
Figure 3.13	Schematic showing the rover-spring set-up in Adams	79
Figure 3.14	Force exerted on the spring by the rover	80
Figure 4.1	MOC-based mosaic of northern Xanthe Terra	101
Figure 4.2a	The extent of the layered sedimentary deposits in Aram Chaos	103
Figure 4.2b	The extent of the layered sedimentary deposits in Aram Chaos	105
Figure 4.3	Schematic cross-section.....	107
Figure 4.4	Spectral reflectance characteristics of the sedimentary deposits.....	109
Figure 4.5	VNIR and Mössbauer spectra.....	110
Figure 4.6	Locations of monohydrated sulfate and ferric hydroxysulfate.....	112
Figure 4.7	Subset of HiRISE image PSP_006953_1840	113
Figure 4.8	CTX mosaic over an area with strong 2.1 and 2.4 μ m absorptions indicative of monohydrated sulfate	114
Figure 4.9	HiRISE image PSP_003406.....	116

Figure 4.10 Detections of monohydrated sulfate, polyhydrated material, and enhanced hydration in CRISM.....	117
Figure 4.11 Subset of HiRISE image PSP_010025_1835	118

LIST OF TABLES

Table 1.1	Rover statistics as of 01-15-2010.....	8
Table 2.1	Date/time and viewing geometries for OMEGA and Spirit data.....	42
Table 2.2	Lat/Lon coordinates of spectra shown in Figure 2.9	43
Table 3.1	Contact parameters used in Adams and typical values.....	81
Table 4.1	Summary parameter mineral indicators.....	119
Table 4.2	CRISM targeted observations used.....	120
Table 4.3	Unit characteristics	121

Chapter 1. Introduction

Prior to 2004, exploration of Mars was done using flyby and orbiting spacecraft, together with two Viking landers and the relatively short-lived Pathfinder mission with the Sojourner microrover [Matijevic and Shirley, 1997]. The 2003 Mars Exploration Rovers (MER), Spirit and Opportunity, were designed to dramatically change the nature of Mars exploration, with placement of two capable rovers with extensive scientific payloads onto the surface for extensive roving and measurements (Figure 1.1) [Squyres *et al.*, 2003]. Spirit and Opportunity landed in January 2004 and have greatly exceeded expectations in mission duration, traverse distance, and nature/number of scientific measurements (Table 1.1). The scientific results from the MER mission led to a paradigm shift in our understanding of Mars and have become the foundation for the next generation of surface missions.

Two new orbiting spacecraft began returning data from Mars while Spirit and Opportunity were exploring the surface: ESA's Mars Express and NASA's Mars Reconnaissance Orbiter (MRO). Data from hyperspectral imagers on both spacecraft have shown that hydration on Mars—mostly in the form of hydrated sulfates and phyllosilicates—is much more prevalent on the surface than previously thought [Bibring *et al.*, 2005b; Gendrin *et al.*, 2005b; Langevin *et al.*, 2005; Murchie *et al.*, 2009]. With the development of a new delivery method (SkyCrane) for new and heavier rovers (e.g. the Mars Science Laboratory, to be launched in 2011), many regions with these hydrated minerals, unreachable with the airbag landing system, are now candidate landing sites.

In this thesis, orbital observations, rover-based remote sensing and in-situ observations, and terramechanics modeling—the study of how vehicles interact with terrains and how those interactions can be used to understand terrain properties—are used to examine the interplay between material properties, scientific setting, and mobility issues. Specifically, the above observations are used concurrently to identify the surface properties on a regional scale for the Gusev Crater Spirit landing site, to understand how the rover interacted with these materials while driving, and as a look ahead to a candidate new landing site, Aram Chaos, with exposed rocks that contain key evidence for past environmental conditions. The results presented in this thesis have both scientific import and relevance for mobility issues facing future Mars rovers such as the Mars Science Laboratory (MSL) and ESA's ExoMars (2018 mission) as they explore areas of Mars that have only been seen from orbit.

Orbital observations and remote-sensing observations from Spirit over the plains in Gusev Crater are used in Chapter 2 to determine that these surfaces are covered with loose basaltic sand and a thin cover of dust. In Chapter 3, it is shown that Spirit had no mobility issues in the flat, sandy terrain of these plains (Figure 1.2) as a fully-capable (i.e. all 6 wheels functioning) rover. With 5 wheels, however—Spirit's right-front wheel drive actuator stopped working around sol 787—navigating sand-covered slopes greater than 3 degrees became challenging. In materials such as the sulfate-rich sands unearthed in Tyrone or Troy, mobility was severely impaired (Figure 1.3).

To quantify mobility performance, analyses were conducted using commercially-available software and a model of Spirit to explore: 1. the effect of material properties on rover mobility using Coulomb and Stribeck theory to model the contacts between wheels

and soil, 2. operating in unusual mobility circumstances such as driving with five wheels, and 3. the magnitude of the rolling resistance not taken into account in the Coulomb/Stribeck contact model. In addition, the recognition of potential mobility issues is addressed through the generation and use of hazard maps in support of drive planning.

The problematic sulfate-rich materials in both Tyrone and Troy were not detected with either orbital data or with Spirit's instruments prior to their unearthing, yet the discovery of these materials is widely accepted as one of the most important scientific achievements of either rover to date. This indicates that despite careful analysis of orbital data over future landing sites, the surface below the top few centimeters must be treated as an unknown quantity when attempting to forecast a rover's drive performance. In addition, the most scientifically interesting locations within the landing ellipse may prove to be the most difficult to traverse.

The detailed stratigraphic analysis of a potential future landing site, Aram Chaos, is presented in Chapter 4. The depositional unit within Aram Chaos is of interest because of the concentrations of hematite and hydrated Mg- and Fe-bearing sulfates exposed in the depositional unit, indicating past presence of water [*Gendrin et al.*, 2005b; *Glotch and Christensen*, 2005; *Masse et al.*, 2008]. Analyses of orbital data from the Compact Reconnaissance Imaging Spectrometer for Mars (CRISM), the High Resolution Imaging Science Experiment (HiRISE), and the Context Imager (CTX) instruments aboard MRO show that the mono- and poly-hydrated sulfates were deposited in two separate depositional events with a period of erosion between. In addition, a new mineral or phase on Mars was discovered via comparison of visible/near infrared spectra on the edges of

the depositional unit to spectra of a laboratory sample of ferric hydroxysulfate, $\text{Fe}^{+3}(\text{OH})\text{SO}_4$ [Morris *et al.*, 2009].

With the scientific rationale for exploration laid out in Chapter 4, the SkyCrane for delivery, and a relatively small landing error ellipse, Aram Chaos is an attractive and scientifically viable target for future missions. The slopes and soil properties are expected to be navigable with a MER-class rover, but a detailed investigation of the traversability of the surface materials is beyond the scope of this thesis. However, in Chapter 3 we address the methodology and tools that would be used for such investigations both prior to landing and during tactical operations.

The work in these chapters was led by K. A. Lichtenberg with guidance from her academic advisor, R. E. Arvidson, and input from relevant co-authors. Chapter 2 has previously been published in the Journal of Geophysical Research [Lichtenberg *et al.*, 2007], Chapter 3 is being prepared for publication, and Chapter 4 is in press in the Journal of Geophysical Research [Lichtenberg *et al.*, 2010a]. The hazard maps discussed in Chapter 3 were conceived, implemented, and generated on a tactical basis for use by the MER team by K. A. Lichtenberg.

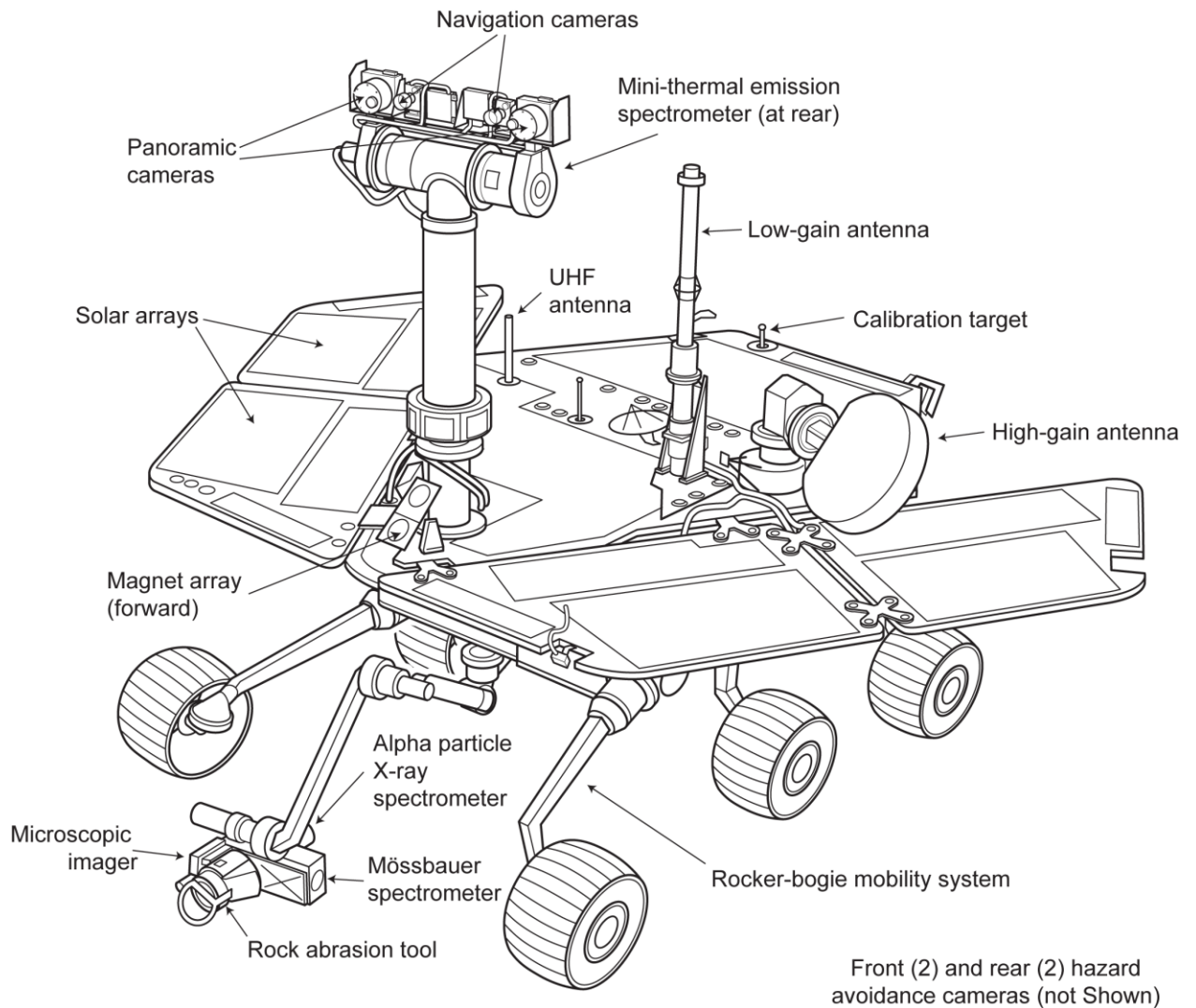


Figure 1.1 Diagram of the Mars Exploration Rover. Spirit’s right front wheel—just below the text “Magnet array (forward)” —lost its drive actuator around sol 787. The Athena Science payload includes the Panoramic cameras, Mini Thermal Emission Spectrometer, Alpha Particle X-ray Spectrometer, Mössbauer spectrometer, Rock Abrasion Tool, and Microscopic Imager.

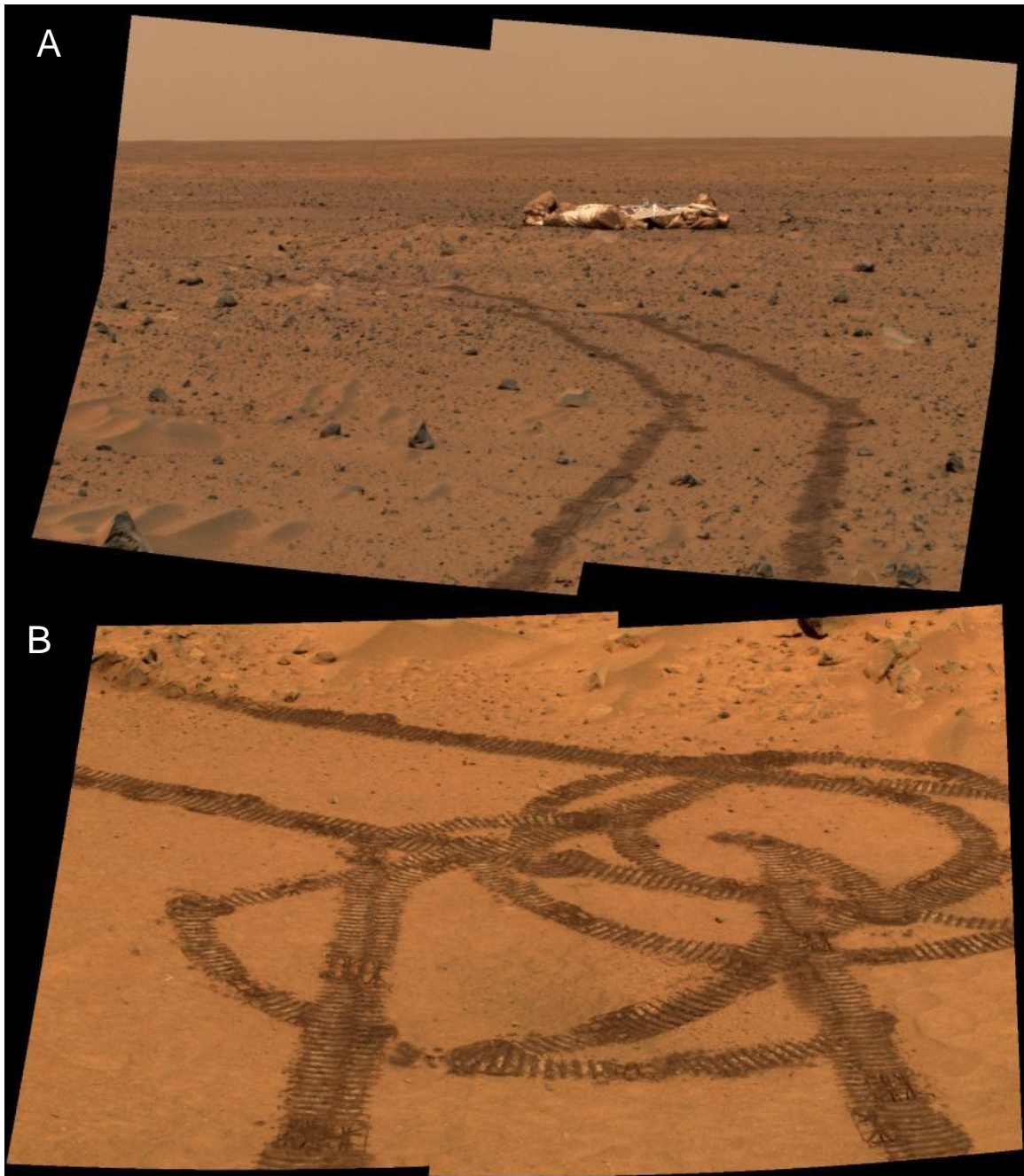


Figure 1.2 Pancam images of Spirit wheel tracks in good mobility situations (all 6 wheels; flat, sandy terrain). The top image (A) was acquired on sol 42 and shows the lander with deflated airbags. The bottom image (B) was taken on sol 58 and shows the tracks from a “turn in place”.



Figure 1.3 Pancam image of Spirit wheel tracks in a poor mobility situation (5 wheels; soft soil). This image was taken on sol 959 looking back at “Tyrone”.

Table 1.1 Rover statistics as of 01-15-2010

	Spirit	Opportunity	Mission Goals
Sols of operation	2146	2125	90
Odometry	7730.2 meters	19,083.9 meters	600 meters
Drive Sols	563	712	N/A
IDD sols	609	683	N/A
Images Returned	123,840	130,182	N/A
Total Data Returned	22.7 Gbytes	23.5 Gbytes	N/A

References

- Bibring, J.-P., Y. Langevin, A. Gendrin, B. Gondet, F. Poulet, M. Berthe, A. Soufflot, R.E. Arvidson, N. Mangold, J.F. Mustard, P. Drossart, and The OMEGA Team (2005), Mars Surface Diversity as Revealed by the OMEGA/Mars Express Observations, *Science*, 307, doi:10.1126/science.1108806.
- Gendrin, A., N. Mangold, J.-P. Bibring, Y. Langevin, B. Gondet, F. Poulet, G. Bonello, C. Quantin, J.F. Mustard, R.E. Arvidson, and S. Le Mouelic (2005), Sulfate in Martian Layered Terrains: The OMEGA/Mars Express View, *Science*, 307, 1587-1591, doi: 10.1126/science.1109087.
- Glotch, T.D., and P.R. Christensen (2005), Geologic and mineralogic mapping of Aram Chaos: Evidence for a water-rich history, *J. Geophys. Res.*, 110, E09006, doi:10.1029/2004JE002389.
- Langevin, Y., F. Poulet, J.-P. Bibring, and B. Gondet (2005), Sulfates in the north polar region of Mars detected by OMEGA/Mars Express, *Science*, 307, 1584-1586, doi:10.1126/science.1109091.
- Lichtenberg, K.A., R.E. Arvidson, R.V. Morris, S.L. Murchie, J.L. Bishop, D. Fernandez-Remolar, T.D. Glotch, E.Z. Noe Dobrea, J.F. Mustard, J.C. Andrews-Hanna, and L.H. Roach (2010), Stratigraphy of Hydrated Sulfates in the Sedimentary Deposits of Aram Chaos, Mars, *J. Geophys. Res.*, In Press, doi:10.1029/2009JE003353.
- Lichtenberg, K.A., R.E. Arvidson, F. Poulet, R.V. Morris, A. Knudson, J.F. Bell III, G. Bellucci, J.-P. Bibring, W.H. Farrand, J.R. Johnson, D.W. Ming, P.C. Pinet, A.D. Rogers, and S.W. Squyres (2007), Coordinated analyses of orbital and Spirit

- Rover data to characterize surface materials on the cratered plains of Gusev Crater, Mars, *J. Geophys. Res.*, *112*, E12S90, doi:10.1029/2006JE002850.
- Masse, M., S. Le Mouelic, O. Bourgeois, J.P. Combe, L. Le Deit, C. Sotin, J.-P. Bibring, B. Gondet, and Y. Langevin (2008), Mineralogical composition, structure, morphology, and geological history of Aram Chaos crater fill on Mars derived from OMEGA Mars Express data, *J. Geophys. Res.*, *113*, E12006, doi:10.1029/2008JE003131.
- Matijevic, J., and D. Shirley (1997), The Mission and Operation of the Mars Pathfinder Microrover, *Control Engineering Practice*, *5*, 6, 827-835, doi:10.1016/S0967-0661(97)00067-1.
- Morris, R.V., D.C. Golden, D.W. Ming, T.G. Graff, R.E. Arvidson, S.M. Wiseman, and K.A. Lichtenberg (2009), Visible and Near-IR Reflectance Spectra for Smectite, Sulfate, and Perchlorate under Dry Conditions for Interpretation of Martian Surface Mineralogy, *Lunar and Planetary Science Conference XXXX*, Houston, TX.
- Murchie, S.L., L.H. Roach, F.P. Seelos, R.E. Milliken, J.F. Mustard, R.E. Arvidson, S.M. Wiseman, K.A. Lichtenberg, J.C. Andrews-Hanna, J.-P. Bibring, J.L. Bishop, M. Parente, and R.V. Morris (2009), Evidence for the origin of layered deposits in Candor Chasma, Mars, from mineral composition and hydrologic modeling, *J. Geophys. Res.*, *114*, E00D05, doi:10.1029/2009JE003343.
- Squyres, S.W., R.E. Arvidson, E.T. Baumgartner, J.F. Bell III, P.R. Christensen, S. Gorevan, K.E. Herkenhoff, G. Klingelhofer, M.B. Madsen, R.V. Morris, R.

Rieder, and R.A. Romero (2003), Athena Mars rover science investigation, *J. Geophys. Res.*, *108*, E12, doi:10.1029/2003JE002121.

Chapter 2. Coordinated Analyses of Orbital and Spirit Rover Data to Characterize Surface Materials on the Cratered Plains of Gusev Crater, Mars

Journal of Geophysical Research, 112, E12S90, doi:10.1029/2006JE002850

© Copyright 2007 by the American Geophysical Union

2.1 Introduction

The Mars Exploration Rovers (MER) Spirit and Opportunity have traversed more than 15 km across the surface of Mars [Squyres *et al.*, 2004a; Squyres *et al.*, 2004b; Arvidson *et al.*, 2006b]. Three spacecraft have orbited the planet during the time period when these traverses were accomplished: Mars Global Surveyor (MGS) [Albee *et al.*, 2001], Mars Odyssey [Saunders *et al.*, 2004], and Mars Express (MEx) [Bibring *et al.*, 2005a]. A fourth orbiter, the Mars Reconnaissance Orbiter (MRO) [Johnston *et al.*, 2005] was launched in 2005 and began returning data in 2006. The plethora of orbital and rover-based observations allows for comprehensive, coordinated analyses of data from both orbital and landed platforms. An analysis comparing orbital and Opportunity Rover observations was previously conducted by Arvidson *et al.* [2006a] for the Meridiani region of Mars. In this paper we adopt a similar approach, focusing on comparisons of the Mars Express Observatoire pour la Mineralogie l'Eau, les Glaces et l'Activite (OMEGA) [Bibring *et al.*, 2005a] spectrometer data and Spirit data over the rover's traverses and surrounding areas for the plains in Gusev Crater. We begin with a review of previous work, then focus on reduction and analysis of OMEGA data and correlations with Spirit observations, and end with an extrapolation of results to regions

beyond the immediate vicinity of the traverse sites by the addition of Thermal Emissions Imaging System (THEMIS)-based thermal inertia estimates and inferences derived from OMEGA data.

OMEGA acquired data over Gusev Crater during eight orbits—24, 72, 976, 1313, 1529, 1879, 1890, and 2249—between January 2004 and October 2005. In this paper, we present data from four orbits (24, 72, 976, and 1313) that have either high spatial resolution coverage of the Spirit landing site and traverses (24, 72, and 976) or extended coverage over Gusev Crater (1313) (Fig. 2.1 and Table 2.1). The OMEGA instrument consists of three spectrometers: a visible/near-infrared (VNIR) spectrometer with 96 bands from 0.36 to 1.07 μm and two shortwave infrared (SWIR) spectrometers: one with 128 spectral bands from 0.93 to 2.7 μm (SWIR-C), and one with 128 bands from 2.6 to 5.2 μm (SWIR-L) [Bibring *et al.*, 2005a]. Because of the complex interaction between reflected and emitted radiation in the 4 to 5 μm wavelength region and complications with the calibration of the SWIR-L spectrometer, we focus on data between 0.4 and 2.5 μm from the VNIR and SWIR-C spectrometers.

2.2 Previous Work

Gusev Crater is a 160 km wide crater of Noachian age centered at 175°E, 14.5°S [e.g., Kuzmin *et al.*, 2000]. The crater is filled with Hesperian-age plains material interpreted to be dominated by basaltic flows and modified by impact and aeolian processes [Golombek *et al.*, 2006]. Two northwest-southeast trending low-albedo streaks of aeolian origin dominate the southwest and middle of the crater. Spirit landed on the eastern streak. Dust devils have been shown to dominate the redistribution of surface

materials and in aggregate are interpreted to be responsible for streak generation by removal of bright surface dust [Greeley *et al.*, 2006].

Thermal Emission Spectrometer (TES) and THEMIS analyses of plains within Gusev Crater show a range of thermal inertia values that correspond to a continuum between (1) low thermal inertia, high-albedo areas, and (2) low-albedo, high thermal inertia areas. TES-based thermal inertia values within the crater range from ~ 150 to $500 \text{ J m}^{-2} \text{ K}^{-1} \text{ s}^{-1/2}$ [Christensen *et al.*, 2005]. Specific units mapped by Martinez-Alonso *et al.* [2005] on the basis of TES-derived thermal inertia include a low thermal inertia unit in the northwest of the crater ($\sim 150 \text{ J m}^{-2} \text{ K}^{-1} \text{ s}^{-1/2}$), a plains unit ($\sim 220 \text{ J m}^{-2} \text{ K}^{-1} \text{ s}^{-1/2}$), a transitional unit surrounding the two low-albedo streaks (no thermal inertia reported), a high thermal inertia unit (morphologically rough) ($300\text{-}450 \text{ J m}^{-2} \text{ K}^{-1} \text{ s}^{-1/2}$), a high thermal inertia unit (smooth) ($300\text{-}550 \text{ J m}^{-2} \text{ K}^{-1} \text{ s}^{-1/2}$), and a low-albedo unit that corresponds to the locations of the two dark streaks. These units are generally consistent with the units mapped by Jakosky *et al.* [2006] and Milam *et al.* [2003]. Our study area covers the plains, transitional, high thermal inertia (smooth), and low-albedo units. The high thermal inertia (rough) and low thermal inertia units are not covered by the OMEGA data analyzed in this paper. TES- and THEMIS-based thermal inertia values have been shown to be in general agreement, although values can differ by $30\text{-}100 \text{ J m}^{-2} \text{ K}^{-1} \text{ s}^{-1/2}$ for the MER and Beagle 2 landing sites [Jakosky *et al.*, 2006], and THEMIS thermal inertia values have been shown to be higher than TES by $\sim 50 \text{ J m}^{-2} \text{ K}^{-1} \text{ s}^{-1/2}$ for Gusev Crater [Martinez-Alonso *et al.*, 2005]. Along Spirit's traverses in the plains, THEMIS-derived thermal inertia values range from 280 to $\sim 330 \text{ J m}^{-2} \text{ K}^{-1} \text{ s}^{-1/2}$ [Ferguson *et al.*, 2006a], whereas thermal inertia values from Spirit's Mini-Thermal Emission Spectrometer (Mini-

TES) on the plains vary between $175 \pm 20 \text{ J m}^{-2} \text{ K}^{-1} \text{ s}^{-1/2}$ (Columbia Memorial Station) and $380 \pm 45 \text{ J m}^{-2} \text{ K}^{-1} \text{ s}^{-1/2}$ (ejecta around Bonneville Crater) [Fergason *et al.*, 2006b]. These values generally correspond to sand sized materials as opposed to rocks or bedrock exposures.

Analysis of Mini-TES spectra for soils disturbed by the rover wheels indicate a basaltic composition of ~45% pyroxene (25% pigeonite and 20% clinopyroxene), ~40% plagioclase, and ~15% olivine [Christensen *et al.*, 2004a; Yen *et al.*, 2005]. The mineral composition of undisturbed soils is difficult to determine from emission spectra due to the small grain size of the ubiquitous dust cover evident from Spirit's observations [Christensen *et al.*, 2004a]. From the Mössbauer (MB) instrument, the Fe mineralogical composition of both the basaltic sand and dust is dominated by olivine, pyroxene, magnetite, and nanophase ferric oxide (npOx) [Morris *et al.*, 2006a]. Nanophase ferric oxide is a ferric alteration product whose abundance is highest in dust and undisturbed soils [Morris *et al.*, 2006a; Morris *et al.*, 2006b]. A dominance of nanophase iron oxides, pyroxenes, and olivine in the basaltic sand is also consistent with analyses of Spirit's Pancam 13-filter spectra [Bell *et al.*, 2004; Yen *et al.*, 2005] and inferences from Alpha Particle X-Ray Spectrometer (APXS) data [Gellert *et al.*, 2004; Ming *et al.*, 2006].

Soils imaged with Spirit's Microscopic Imager (MI) reveal a wide variation in grain sizes, from 1.4 mm down to the 100 μm resolution limit of the MI [Herkenhoff *et al.*, 2004]. The ability of the soil to retain shape after compression by the Mössbauer plate indicates that the soil is poorly-sorted and implies a fairly high fraction of grain sizes below the 100 μm spatial detection limit of the MI instrument [Arvidson *et al.*, 2004; Arvidson *et al.*, 2006b]. Rocks on the plains cover about 7% of the surface

[*Golombek et al.*, 2006] and are variably covered by dust and thin alteration rinds or coatings [*McSween et al.*, 2004]. Rock interiors are dominated by olivine, pyroxene, and plagioclase with small amounts of magnetite, chromite, ilmenite, and apatite according to normative calculations from APXS data [*McSween et al.*, 2004; *McSween et al.*, 2006]. Given the low areal abundance of rocks and outcrop as observed by Spirit on the plains, basaltic soils and the ubiquitous dust cover will dominate spectral signatures of the plains as observed from orbit.

The data thus summarized support the conclusion that the plains traversed by Spirit through Sol 200 are dominated by a fine-grained dust cover over unaltered or weakly-altered basaltic sands. The basaltic sand is relatively uniform in composition across Spirit's traverses to date and the dust component seems to have been mixed on a global scale as multiple measurements at different locations around the planet reveal similar compositions [e.g., *Yen et al.*, 2005].

2.3 Comparison of OMEGA and Pancam Spectra From 0.4 to 1.0 Micrometers

In this section we pursue comparisons between Pancam- and OMEGA-derived spectra for regions along Spirit's plains traverses to test the hypothesis that both data sets have been properly reduced to surface reflectance and observe the same spectral properties, adjusted appropriately for the relevant spatial sampling scales. Pancam acquires spectra over 13 "geology" filters spanning a wavelength range of 0.43 to 1.01 μm [*Bell et al.*, 2004]. Surface I/F values for Pancam are commonly called R^* and are derived by removing atmospheric effects through use of the calibration target and

normalizing to the cosine of the incidence angle [Bell *et al.*, 2006]. R^* spectra are essentially Lambert Albedos.

OMEGA data from orbit 24 was chosen for comparison with Pancam data based on the combination of high spatial resolution and favorable lighting, i.e., relatively low solar incidence angle of 25.3 degrees (Table 2.1). The traverses across the plains from Bonneville Crater to just before the West Spur, Columbia Hills, covered ~2 km. Data from orbit 24 only cover the western half of the traverse, or ~2-3 400 meter pixels (Fig. 2.2 and Table 2.1). Two pixels over Spirit's traverses were located by latitude and longitude coordinates derived from spacecraft position and pointing information. Although we cannot be certain that these two pixels cover only the traverse (i.e. the pixels might be shifted due to spacecraft pointing error), the area within 5 pixels of the Spirit rover's traverses across the plains are homogenous on the scale of the orbit 24 observation (~400 meters/pixel) to within $\pm 2.1\%$ based on the 0.805 μm band Lambert Albedo. Thus even with ~1 km of pointing error, we should properly sample what Spirit has seen in the western half of the plains traverse. A Navcam image from Sol 127 (Fig. 2.3) shows typical terrain in the plains between Bonneville crater and the Columbia Hills, along with the darker surface of weakly altered basaltic sands revealed when the rover wheels disturbed the surface dust.

To adjust for the difference in spatial scales between Pancam and OMEGA, we used twenty-two Pancam foreground stares taken at relatively regular intervals along the plains between Sols 75 and 191. These foreground stares provide a random sampling of undisturbed plains surfaces over a spatial scale that is on the order of the OMEGA orbit 24 data. Of the twenty-four stares taken between Sols 75 and 191, two were rejected

because of either poor image quality (Sol 88) or the presence of rover shadow in the scene (Sol 159). The other twenty-two are used in this paper and show no systematic variation in average albedo from west to east (Fig. 2.4 and Table 2.1). The Pancam foreground stare from Sol 128 shown in Figure 2.5 is typical and illustrates the fact that the surface is dominated by bright and less bright soils, together with bright rock clasts. We also identified a very dusty surface on the plains—‘White Elephant’, Sol 72 (Fig. 2.6)—in order to compare Pancam and OMEGA spectra of dusty surfaces. The ‘White Elephant’ target was selected because it had one of the highest Pancam albedos on the plains, signifying a relatively thick dust cover.

During the OMEGA measurement periods, Spirit acquired atmospheric optical depth measurements using the Pancam images of the sun at 400 and 800 nm [*Lemmon et al.*, 2004], and Mini-TES spectra of the lower atmosphere at multiple elevation angles [*Wolff et al.*, 2006]. These observations, together with dust and ice aerosol radiative properties based on historical trends from TES data [*Smith et al.*, 2006] and estimates of atmospheric pressure and temperature profiles, were used with the DISORT radiative transfer code [*Stamnes et al.*, 1988] to model OMEGA spectral radiances. Atmospheric carbon dioxide, water vapor, carbon monoxide, and associated Rayleigh scattering and discrete gas bands were included in the computations, along with aerosol scattering and absorption. Procedures were implemented to retrieve surface Lambert Albedos using DISORT-based simulations and regressions for each wavelength band between modeled OMEGA radiances and a suite of input surface albedos. The retrieved surface spectra were examined for residuals associated with incomplete removal of atmospheric carbon dioxide and water vapor. Runs with updated atmospheric conditions relative to historical

trends and rover-based observations allowed us to converge on the proper atmospheric model within several iterations.

Figure 2.7 shows the comparisons among the twenty-two Pancam foreground stares, Pancam dust spectrum, and OMEGA-based Lambert Albedos of the Spirit landing site and bright plains north of the landing site (Fig. 2.2). The mismatches between the shape of the OMEGA and Pancam spectra at wavelengths shorter than 0.7 μm are not unexpected due to calibration uncertainties for OMEGA data. In addition, the dielectric function and single-scattering albedo of atmospheric dust in this wavelength region (0.35 to 0.7 μm) is at present not well constrained and so it is difficult to completely remove aerosol effects [Clancy *et al.*, 2003]. We note that the OMEGA and Pancam reflectance data are better matches in the 0.7 to 0.9 μm region. Specifically, the OMEGA Bright Plains North spectrum matches the Pancam dust spectrum and the average OMEGA spectrum for the traverses falls within the foreground stare spectral envelope. The overall trends among the Pancam and OMEGA spectra for the relatively well-calibrated and modeled (i.e. aerosol removal) longer wavelength (0.7-0.9 μm) data indicate that OMEGA and Pancam are both observing the same surfaces, albeit on different length scales. In addition, analyses from Spirit data as already noted indicate that both Spirit Pancam data and OMEGA data over the rover traverses are observing dust-covered basaltic sand.

In order to extend our analyses over a wider range of regions that incorporate the dust and basaltic-sand end-members, we extracted Pancam reflectance data from Sol 343 observations on the West Spur of the Columbia Hills (Figs. 2.4 and 2.6). Figure 2.8 shows both (1) Pancam spectra of undisturbed, dust-covered surfaces (Sols 72 and 343)

and disturbed areas within rover wheel tracks (Sol 343) and (2) Lambert Albedos derived from orbit 24 data. The OMEGA Lambert Albedos span a range of surface types, from a low-albedo surface within the dark plains to regions within the bright plains both north and south of the Spirit landing site (see Fig. 2.2). A spectrum from Apollinaris Patera ~300 km north of Gusev Crater is included because thermal inertia values as mapped by *Putzig and Mellon* [2007] suggest it is covered with a dust layer thick enough (≥ 1 cm) to dominate thermal properties [e.g., *Arvidson et al.*, 1989]. In all OMEGA data presented, dark-plains spectra were extracted from regions within the low-albedo streaks with the lowest 1 μm reflectance values as observed in C data. Bright-plains spectra were selected visually by locating bright, relatively uniform regions in areas north and south of the dark swath in order to ensure consistent results between orbital data. The Spirit Landing Site and Spirit Traverse spectra were located based on both cross correlations between the latitude and longitudes provided by OMEGA ancillary files and the locations derived from Spirit radio science and traverse statistics [*Li et al.*, 2004]. The bright plains spectra occur within the “Plains” unit of *Milam et al.* [2003] as defined by THEMIS IR data whereas the Spirit Landing Site/Traverse spectra and Dark Plains spectra are from their “Low Albedo” unit. We also provide an Apollinaris Patera spectrum for each orbit since, as noted, the albedo and thermal inertia of this region is consistent with the presence of a dust-dominated surface [*Putzig and Mellon*, 2007]. The locations of the spectra are given in Table 2.2.

The combined OMEGA and Pancam surface reflectances presented in Figure 2.8 are again consistent with variable amounts of dust overlying basaltic sand. The spectra

show a gradation of albedos between the dust-dominated Apollinaris Patera and Sol 72 Pancam spectra and the basaltic soil-dominated Pancam Wheel Track spectrum.

2.4 Analysis of OMEGA Spectra Covering 0.4 to 2.5 Micrometers

Having shown that Spirit and OMEGA produce self-consistent data sets and that spectra over a large region indicate a variation in the thickness of the dust cover over basaltic sand, we move to using the full spectral and regional coverage from OMEGA to map surface materials. We did not use DISORT to retrieve surface reflectances in this section because processing this amount of data would be computationally intensive. Instead, OMEGA radiance data were converted to I/F (radiance-on-sensor divided by solar radiance) and absorptions due to atmospheric gas bands were removed by normalizing to a gas transmission spectrum. This spectrum was obtained by acquiring data over Olympus Mons, where the surface spectra are dominated by dust signatures and the atmospheric path length varies from the top to the base of the volcano. Dividing I/F values at the base to the values at the summit produces a transmission spectrum which can then be used to remove gas features from other spectra. In practice, what is done is to scale the transmission spectrum by the depth of the 2-micrometer carbon dioxide band for the observation of interest. This method has been used extensively in reduction of OMEGA data, as described in the works of *Mustard et al.* [2005] and *Langevin et al.* [2005] and used in the works of *Gendrin et al.* [2005a] and *Poulet et al.* [2005]. We note that this method has only been applied to data from the SWIR-C spectrometer because shortward of 1 μm , atmospheric effects are dominated by aerosols.

OMEGA data are shown for various regions including the low-albedo streaks and surrounding bright plains in Figure 2.9. The locations of the spectra are shown in Figure 2.2 and described in Table 2.2. All of the retrieved OMEGA spectra have an absorption edge between 0.4 and 0.75 μm resulting from charge transfer and electronic transitions associated with ferric iron, although, as noted, the exact shape of the spectra in this wavelength region is uncertain because of calibration issues. The generally featureless nature of the edge and the absence of well-defined minima in the region between 0.7 and 1.2 μm imply a dominance of Fe^{3+} in nanophase ferric oxide (npOx) relative to Fe^{3+} in well-crystalline ferric oxides (e.g., hematite and goethite) [Bell *et al.*, 1993; Morris *et al.*, 1993; Morris *et al.*, 1997; Morris *et al.*, 2000; Morris *et al.*, 2006a]. Spectra from orbits 72, 976, and 1313 show a shallow dip at ~ 1.0 μm and a broad reflectance peak centered at 1.4 μm consistent with the presence of pyroxene bands near 1 and 2 μm . In orbit 24 data, the detector was saturated between 1.37 and 1.63 μm and so identification of the 1.4 μm local reflectivity maximum in spectra from orbit 24 data is impossible.

Low-albedo spectra for our study areas show negative overall slopes between 1.5 to 2.5 μm (e.g., Fig. 2.9). Although a negative spectral slope can result from the presence of a glassy varnish, the low glass content seen in the Mini-TES and MB observations of disturbed soils make that interpretation unlikely [Christensen *et al.*, 2004a; Yen *et al.*, 2005; Morris *et al.*, 2006a]. In addition, we have shown that dust-covered basaltic sand satisfies both the observations from Spirit and the short wavelength OMEGA data. Optically thin bright dust coatings over dark surfaces in fact produce negative slopes from 1.0 to 2.5 μm as observed by Johnson and Grundy [2001] and Graff [2003]. Johnson and Grundy [2001] provide two explanations for these negative slopes with

weak absorption features in spectra of dust-covered dark substrates: (1) dust becomes translucent at longer wavelengths, and (2) the single-scattering phase function of the dust is wavelength dependent, with dust becoming more forward-scattering at longer wavelengths. Both phenomena result in the incorporation of the spectral signature of the basaltic sand into the spectra between 1.5 and $\sim 2.7 \mu\text{m}$ as the wavelength increases. As the cover of dust-like material becomes thicker, the underlying substrate and its spectral features become masked. *Johnson et al.* [2002] and *Graff* [2003] show that dust coatings on the order of 100-120 μm thick are sufficient to mask the spectral features of an underlying dark substrate.

2.5 Combined Analysis of Spectral and Thermophysical Properties

In this section, we explore correlations between dust-sensitive spectral parameters derived from OMEGA data and THEMIS-based thermal inertia. The intent is to evaluate the extent to which dust becomes thick enough ($\sim 1 \text{ cm}$) to influence the soil thermal properties derived from diurnal temperature variations. Specifically, we compute BD530c band depth, spectral slope, and $1.01 \mu\text{m}$ albedo (Fig. 2.10) from OMEGA orbit 1313 data because of the wide area covered by this data set. A thermal inertia map of Gusev Crater was generated using the method developed by *Mellon et al.* [2000] and *Piatek and Moersch* [2007] in which a look-up table of diurnal temperature cycles is computed for variations in time-of-day, season, latitude, albedo, surface pressure, dust opacity, and thermal inertia. Thermal inertia was then interpolated based on THEMIS predawn brightness temperature estimates and TES bolometric albedo.

A map of the depth of the ferric absorption at 0.53 μm (BD530c) was calculated from OMEGA orbit 1313 data using the following algorithm: $1 - I/F(0.524 \mu\text{m})/[0.5 \cdot I/F(0.42 \mu\text{m}) + 0.5 \cdot I/F(0.63 \mu\text{m})]$. This algorithm is similar to the BD530b parameter used by *Morris et al.* [2000] and the same as the equivalent parameter used by *Poulet et al.* [2007]. The $\sim 0.53 \mu\text{m}$ ferric absorption feature results from intense Fe^{3+} electronic field transitions centered between 0.5 and 0.6 μm [*Morris et al.*, 2000]. Although OMEGA calibration issues preclude quantitative comparisons of BD530c results to lab spectra, relative trends within the OMEGA data should still be viable. The BD530c map in Figure 2.10 shows that the bright plains to the north and south of the landing site have larger BD530c values than the dark plains, indicating higher proportions of Fe^{3+} materials for these bright surfaces. Maps of the magnitude of the spectral slope between 1.5 to 2.5 μm and the albedo at 1.01 μm were created to evaluate the extent of the dust cover. Dusty regions should have flat spectral slopes between 1.5 and 2.5 μm (i.e., small magnitude of spectral slope) and high 1- μm albedos.

To explore relationships among spectral slope, albedo, BD530c, and thermal inertia, we plotted the 1.01 μm albedo vs. thermal inertia, spectral slope, and BD530c values for the area shown in Figure 2.10 (Fig. 2.11). Results show that the Bright Plains have relatively high albedos and BD530c values along with spectral slopes that are relatively flat. This is consistent with a fairly extensive cover of nanophase iron-oxide-rich dust. The Dark Plains 1 and 2, which include the Spirit landing site, have lower albedos, lower BD530c band depths, and more negative spectral slopes, indicating that the dust cover in these regions is thin enough to reveal the dark basaltic sand spectral signature at long wavelengths.

Comparison of the 1.01 μm albedo and thermal inertia shows that Bright Plains North and South are relatively bright and have low thermal inertias. TES-based thermal inertia values for Apollinaris Patera, a highly dust-covered region just to the north of Gusev Crater, are $\sim 50 \text{ J m}^{-2} \text{ K}^{-1} \text{ s}^{-1/2}$ [Putzig and Mellon, 2007]. This value is a factor of 3 less than those observed for the bright plains regions and indicates that the dust cover in the bright plains is not thick enough to dominate the diurnal thermal wave depth of $\sim 1 \text{ cm}$ [Arvidson *et al.*, 1989], i.e. the underlying basaltic sand dominates the thermal signature even though the spectral properties of the substrate are masked between 0.35 and 2.5 μm .

The notable stand-out in the plots shown in Figure 2.11 is the Dark Plains 3 region. This area has low albedos and BD530c band depths, negative spectral slopes, and relatively high ($>400 \text{ J m}^{-2} \text{ K}^{-1} \text{ s}^{-1/2}$) thermal inertia values. We interpret the high thermal inertia values in this region to indicate that it has larger basaltic sand grain sizes than the other two low-albedo regions, consistent with the conclusions of Christensen *et al.* [2005].

2.6 Conclusions

Combined analyses of OMEGA and Spirit data for the Gusev Crater plains show that surface covers are dominated by nanophase iron-oxide-rich dust deposits that cover and partially obscure underlying weakly-altered basaltic sands. OMEGA spectra indicate that plains beyond the Spirit site have a dust cover thick enough to mask the spectral signature (0.4 to 2.5 μm) of the underlying basaltic sands, but not thick enough ($<1 \text{ cm}$) to influence the thermal properties.

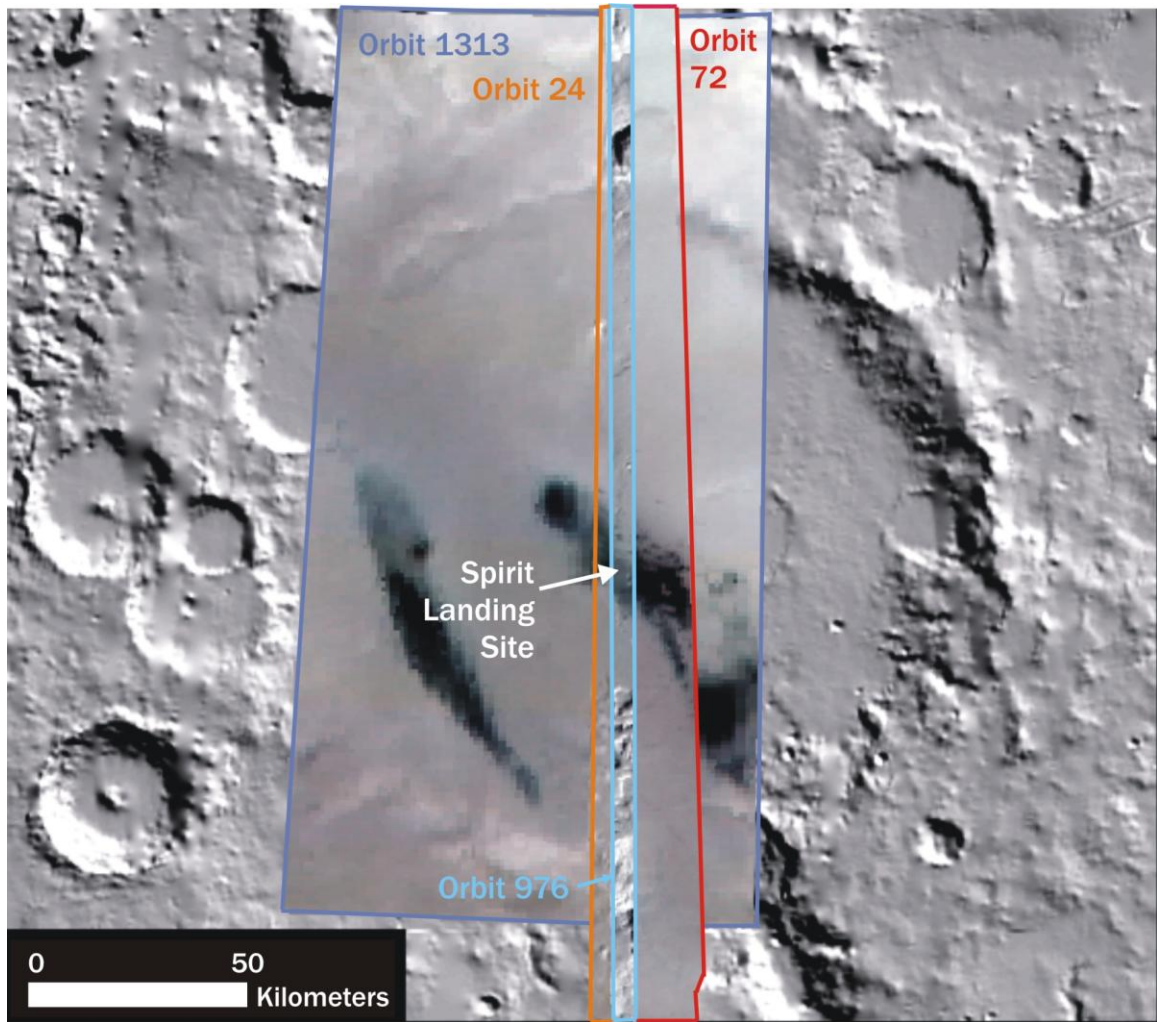


Figure 2.1: Footprints of OMEGA data coverage for orbits 24, 72, 976, and 1313 over Gusev Crater, with the Spirit landing site shown. Background is MOLA data shown as shaded relief at 128 pixels/degree. Simulated illumination is from the northeast at 30°.

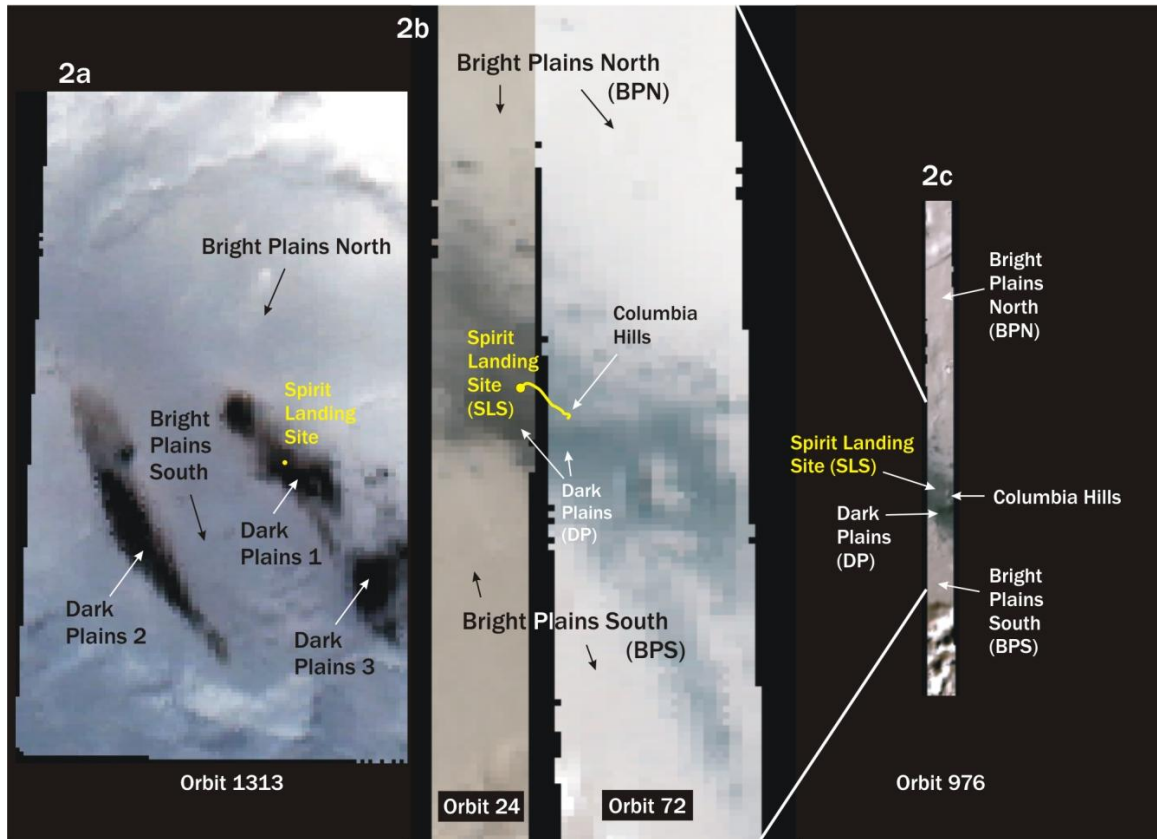


Figure 2.2: False-color mosaic of OMEGA data for orbits 1313 (2a), 24, 72 (2b), and 976 (2c) annotated with locations of the spectra shown in Figure 9. The Spirit landing site and traverse (yellow) are located in the eastern of two low-albedo swaths. Bright plains bound the low-albedo areas to the north and south. The Columbia Hills are visible as bright patches in the dark swath in orbit 976. Images are false-color IR with band assignments of $2.31 \mu\text{m}$ to red, $1.78 \mu\text{m}$ to green, and $1.22 \mu\text{m}$ to blue. Sun illumination is from the northeast in orbits 1313 and 72 and from the west in orbits 24 and 976.

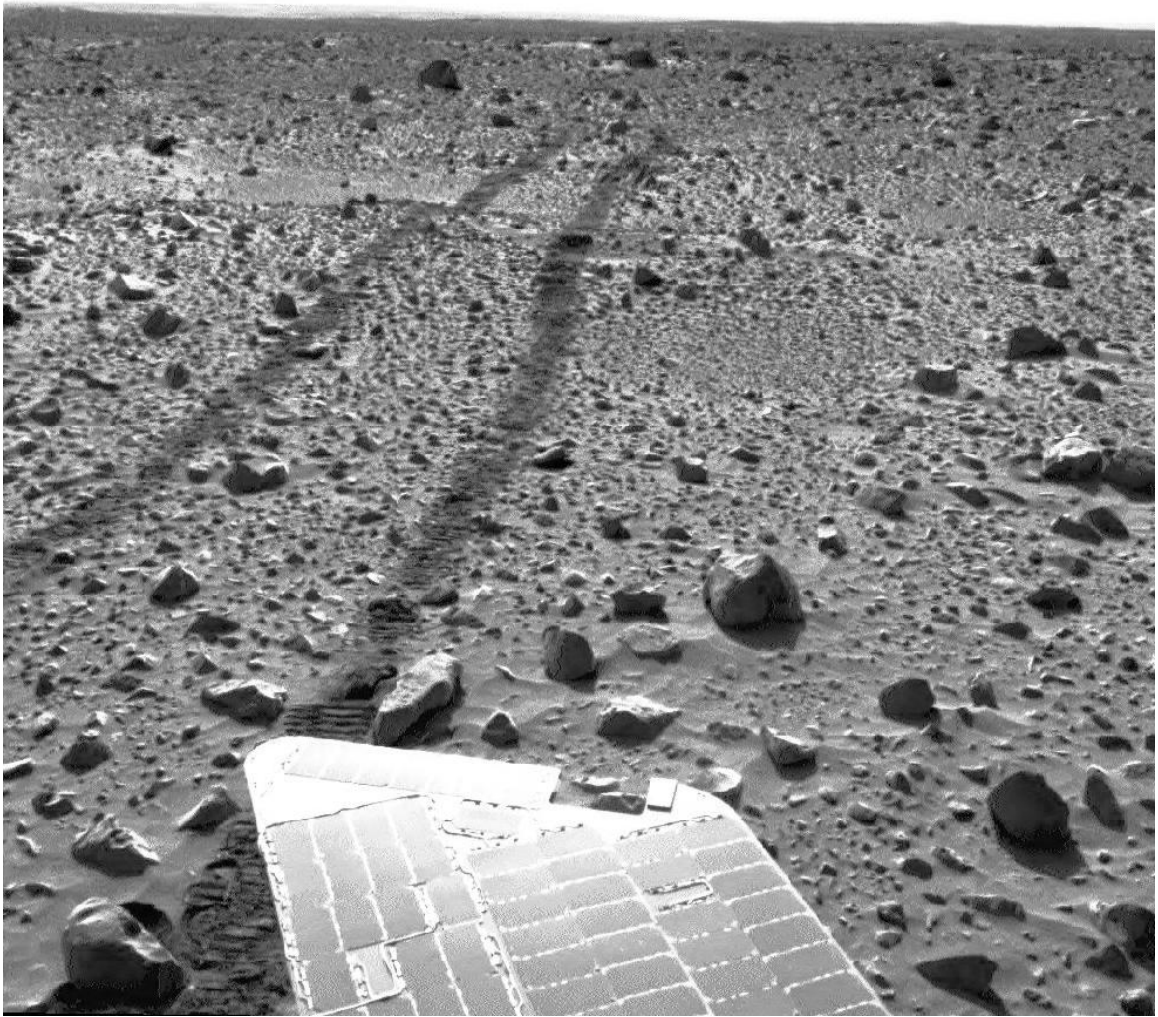
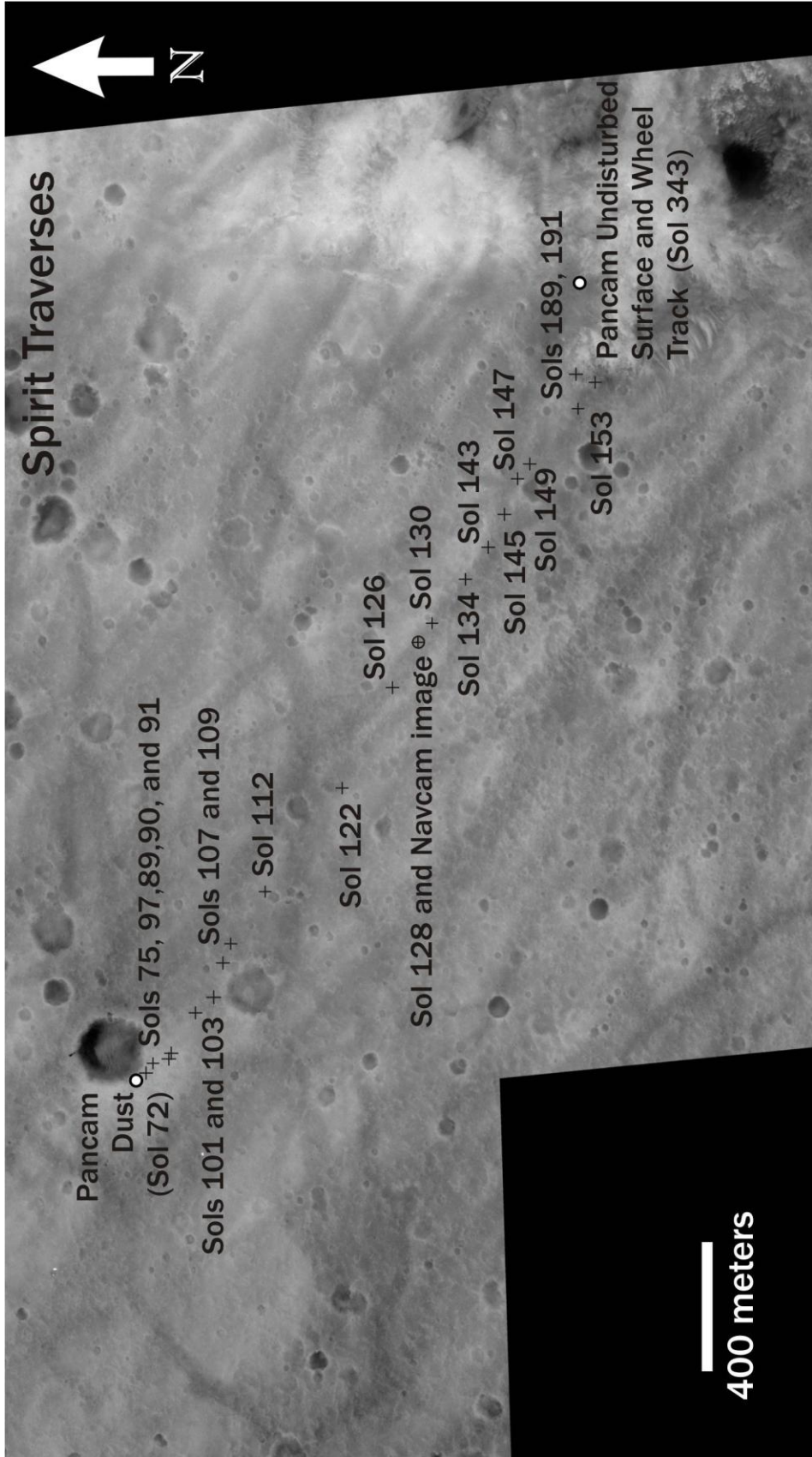


Figure 2.3: Navcam image (2N137650599MRL4800P1846R0M1) from Sol 127 looking west. Visible are the dark rover tracks caused by disturbance of the bright dust cover.



Spirit Traverses

Pancam

Dust

(Sol 72) + Sols 75, 97, 89, 90, and 91

Sols 101 and 103 + Sols 107 and 109

+ Sol 112

Sol 122 +

+ Sol 126

Sol 128 and Navcam image + Sol 130

Sol 134 + Sol 143

Sol 145 + Sol 147

Sol 149 + Sols 189, 191

Sol 153 + Pancam Undisturbed
Surface and Wheel
Track (Sol 343)



400 meters

Figure 2.4: Locations of 22 Spirit Pancam 13-filter foreground stares along the plains traverse (Background: mosaic of MOC narrow angle frames R1301467 and R1303051); Pancam foreground stare locations used in this paper are identified with crosses. Also shown are the locations of the Navcam image in Figure 2.3 (open circle) and the Pancam images shown in Figure 2.6 (closed circles).



Figure 2.5: Pancam foreground stare from Sol 128 (ancillary information in Table 2.1).

This is a representative sampling of the plains surface. Image width is ~50 cm. Band assignments are 0.602 μm to red, 0.530 μm to green, and 0.440 μm to blue.



Figure 2.6: Pancam false-color images p2556 -Sol 72 (left) and p2574-Sol 343 (right).

The arrow denoting Pancam Dust in the left image shows where the 'Pancam Dust' R* spectrum shown in Figures 2.7 and 2.8 was acquired. The arrows in the right image show where the 'Pancam Undisturbed Surface' and 'Pancam Wheel Track' R* spectra shown in Figure 2.8 were acquired. The band/color assignments are 0.602 μm to red, 0.530 μm to green, and 0.440 μm to blue.

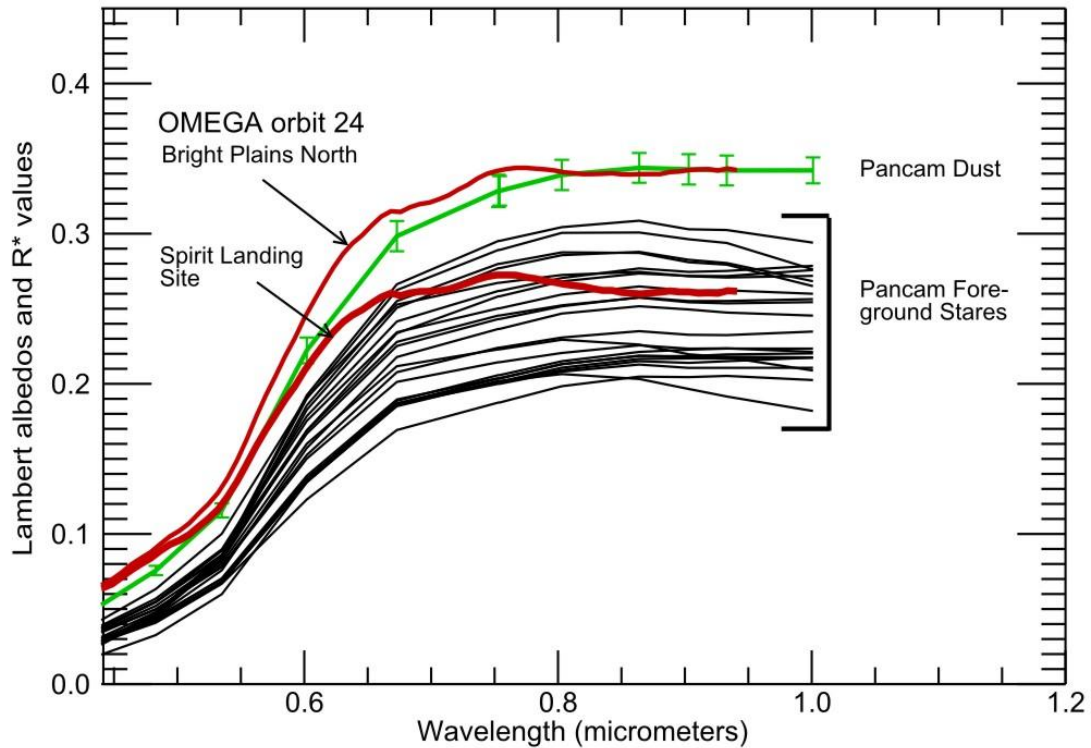


Figure 2.7: DISORT-retrieved Lambert Albedo of the Bright Plains North and Spirit Landing Site locations in OMEGA orbit 24 (red), plotted with 22 Pancam foreground stares that occurred between Sol 75 and Sol 191 (black) and a ‘Pancam Dust’ spectrum from Sol 72 (green). Ancillary information can be found in Table 2.1. Pancam foreground stares are plotted without $1-\sigma$ error bars. The ‘Pancam Dust’ spectrum is of the ‘White Elephant’ target within Serpent Drift and was one of the highest albedos we found along the plains, signifying a very dusty surface. The OMEGA Bright Plains North spectrum was obtained from an area to the north of the Spirit Landing Site (Figure 2.2; Table 2.2). The discrepancy between the shapes of the Pancam and OMEGA spectra is addressed in the text.

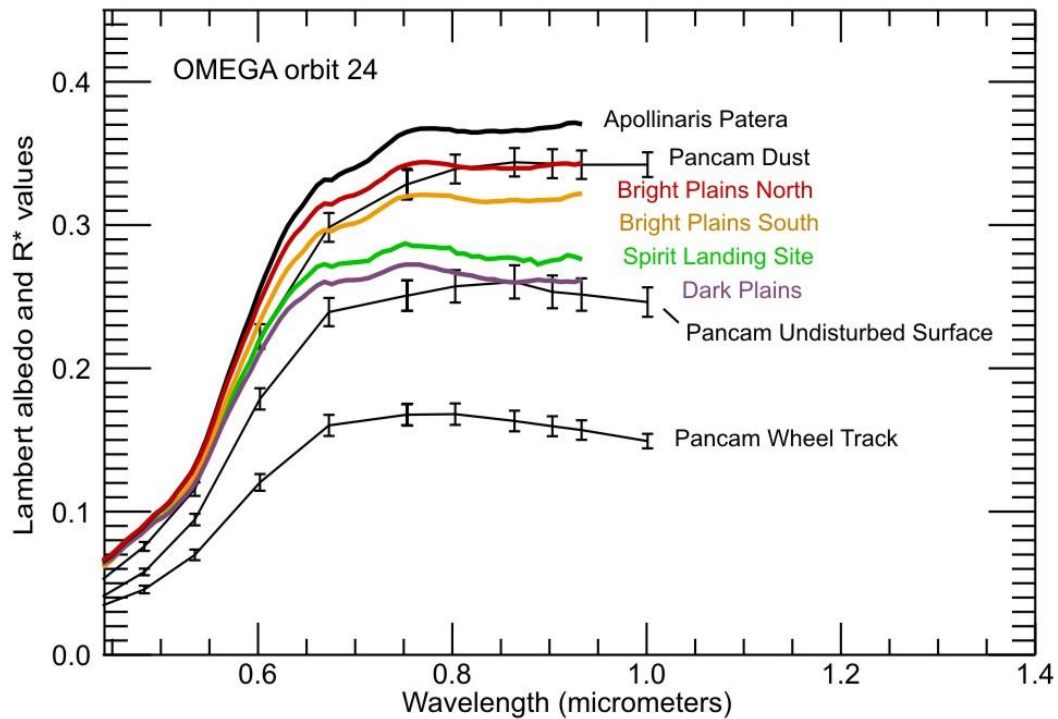


Figure 2.8: Pancam R^* with OMEGA Lambert Albedo spectra from orbit 24 data. OMEGA locations are shown in Figure 2b except for the Apollinaris Patera surface Lambert Albedo, which is located ~300km north of Gusev Crater. The Pancam R^* spectra locations are shown in Figure 2.6. Error bars on the Pancam spectra are 1- σ standard deviation. The combination of the OMEGA spectra and Pancam spectra covers the full range of surface types from completely dust-covered to mainly basaltic sand with minor amounts of ferric-rich dust.

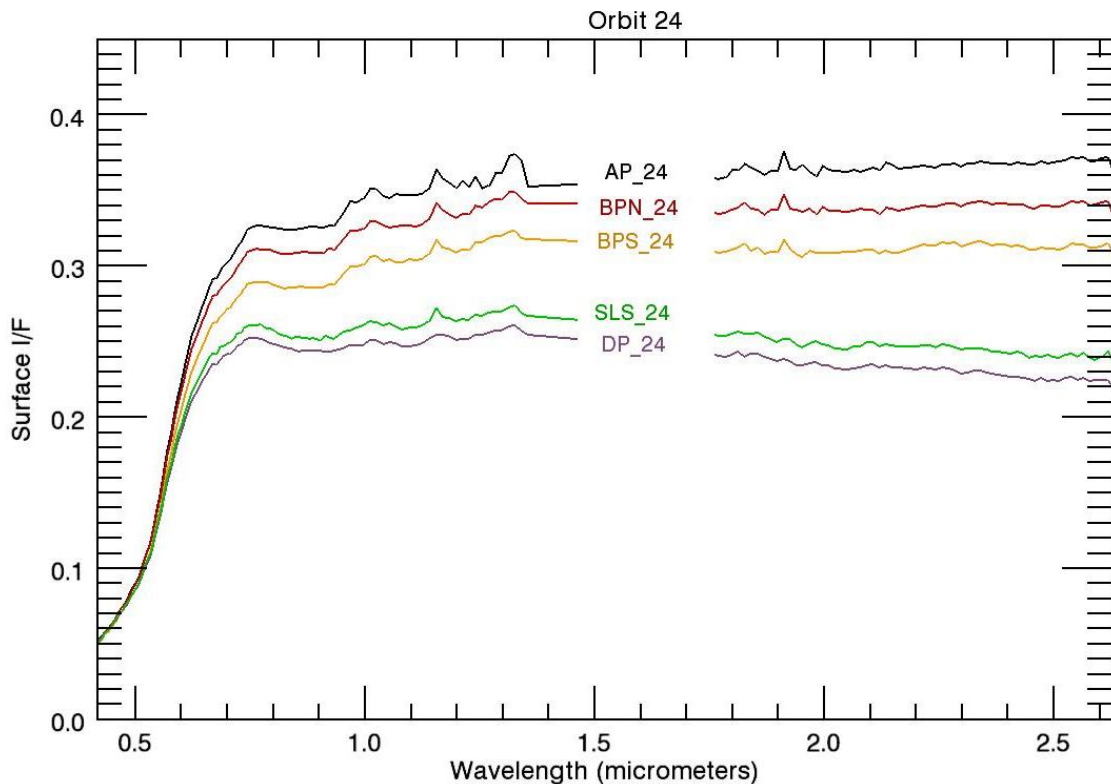


Figure 2.9A: OMEGA VNIR and C spectrometer data from orbit 24. Retrieved surface I/F values are shown for the Spirit landing site (SLS_24; two 400 m pixels), dark plains (DP_24; average of 3x3 pixels), and bright plains areas (BPN_24 and BPS_24; average of 5x5 pixels). An additional spectrum from Apollonaris Patera (areocentric lat=-8.5°N, lon=176°E) north of Gusev Crater (areocentric lat=-14.5°N, lon=175°E) is shown to represent a dust-rich spectral end-member (5x5 pixels). Data between 1.37 and 1.63 μm are saturated in orbit 24 observations and are not shown. Ancillary information can be found in Table 2.2.

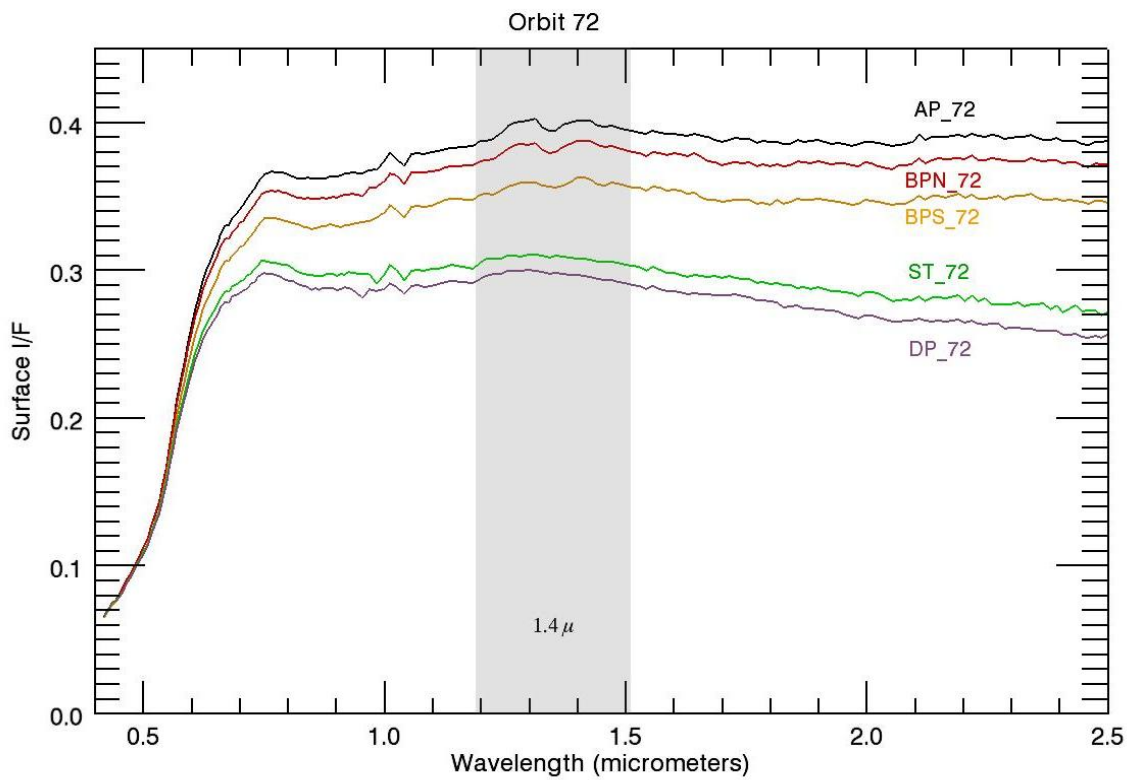


Figure 2.9B: OMEGA VNIR and C spectrometer data from orbit 72. The dark-plains surface I/F (DP_72) is an average of 3x3 pixels, and the bright-plains north and south (BPN_72 and BPS_72) and Apollinaris Patera (AP_72) are averages of 5x5 pixels. The Spirit traverse (ST_72) spectrum is a single 840-m pixel covering the eastern half of Spirit's traverses in the plains.

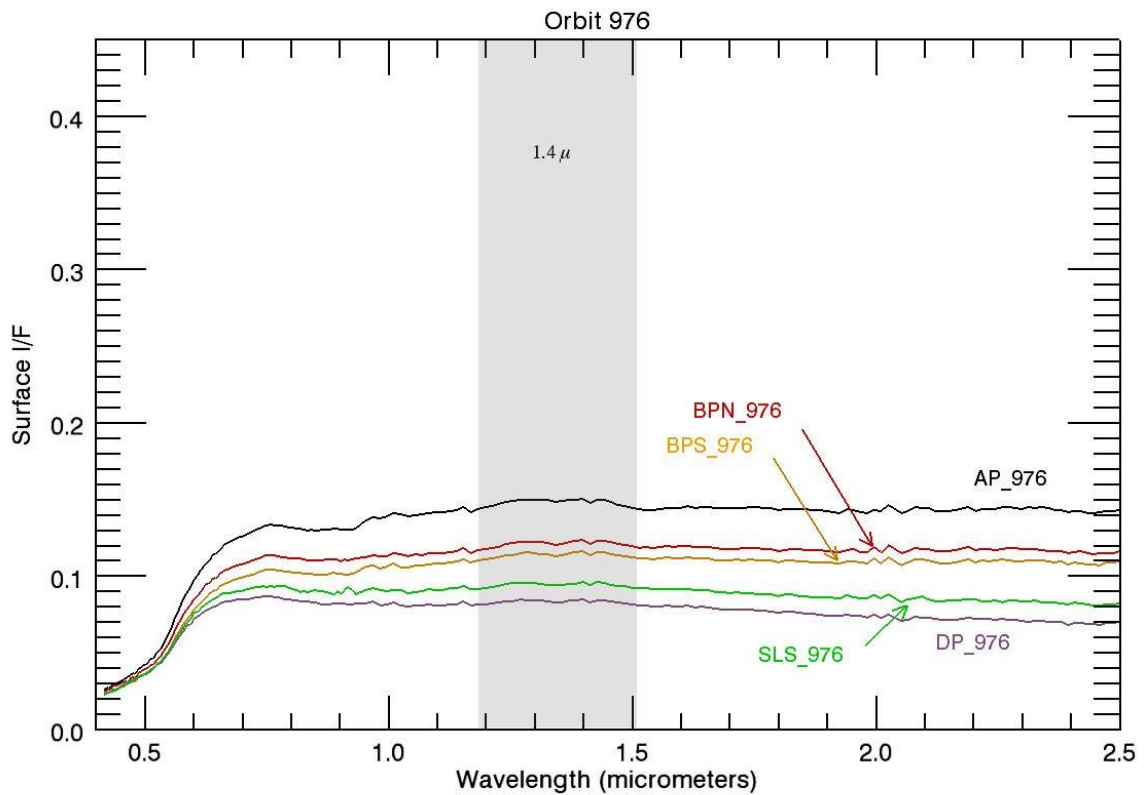


Figure 2.9C: OMEGA VNIR and C spectrometer data from orbit 976. The Spirit Landing Site (SLS_976) is a single 375 m pixel. The dark-plains (DP_976) spectrum is an average of 3x3 pixels whereas the bright-plains north (BPN_976), bright-plains south (BPS_976), and Apollinaris Patera (AP_976) are averages of 5x5 pixels. The magnitude of the albedos from orbit 976 is less than that of the other orbits because of the high incidence angle (see Table 2.1).

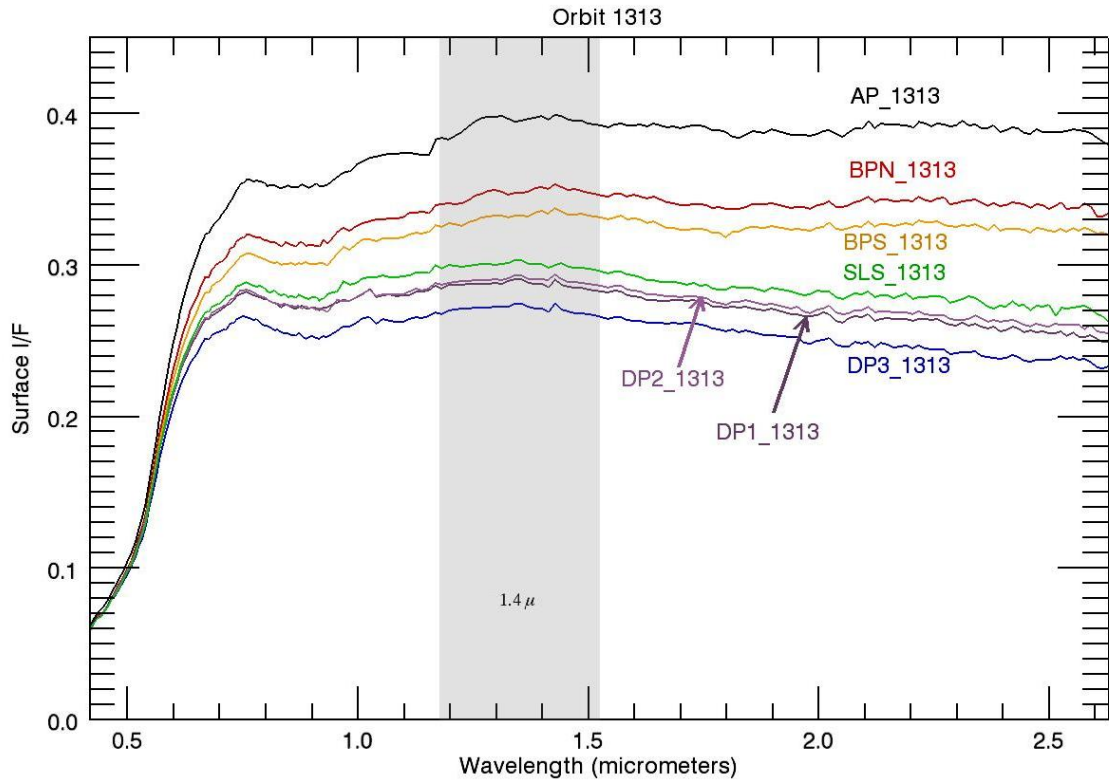


Figure 2.9D: OMEGA VNIR and C spectrometer data from orbit 1313. All are 2x2 pixel averages except the single-pixel Spirit Landing Site (SLS_1313) spectrum. Spectral features (e.g. rise in reflectance centered around 1.4 μm) are discussed in the text.

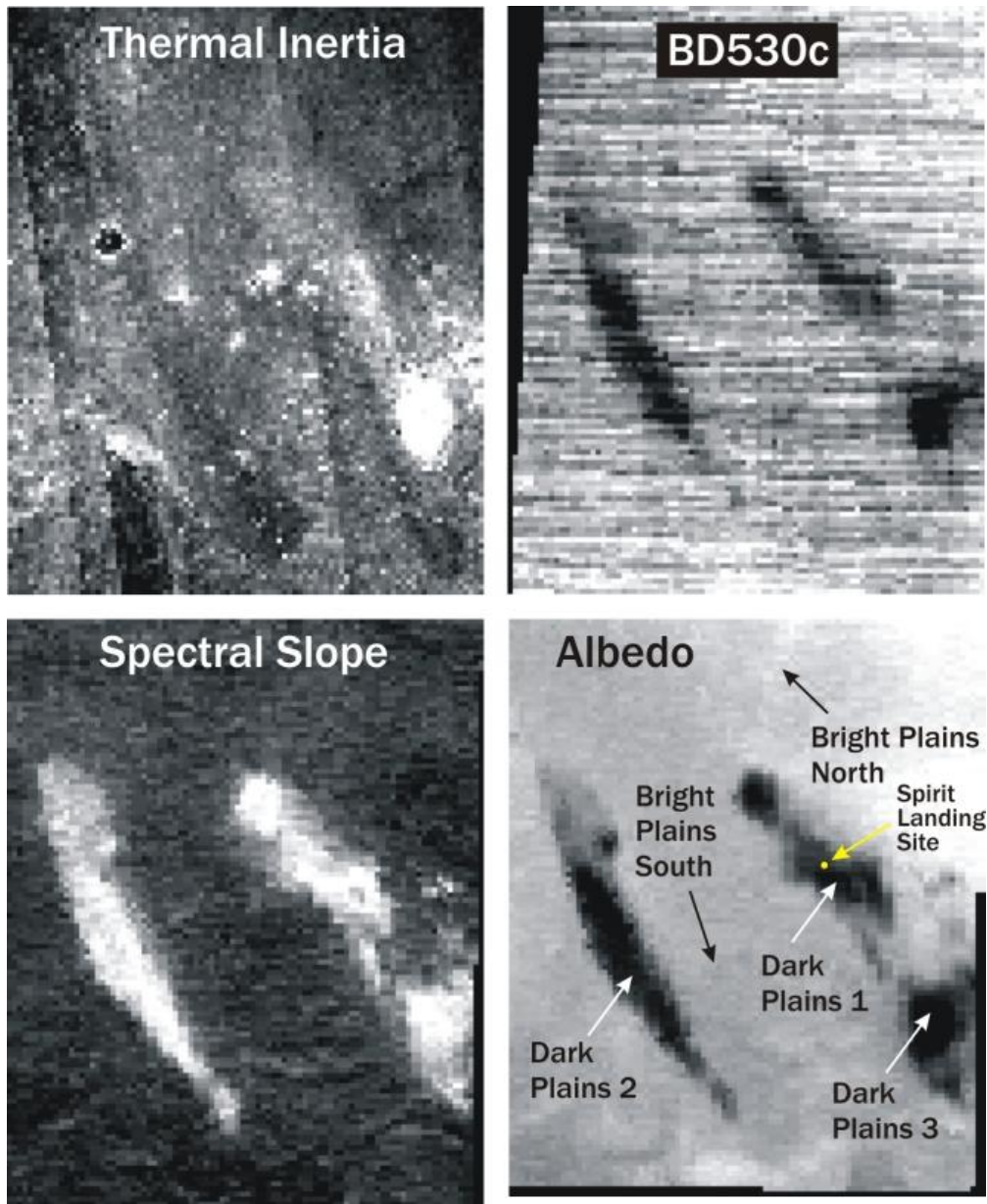


Figure 2.10: Images of thermal inertia derived from THEMIS and TES data, 0.53 μm band depth (BD530c), magnitude of spectral slope, and albedo derived from OMEGA orbit 1313 data. BD530c, spectral slope, and 1.01 μm albedo use Lambert Albedos retrieved from radiative models of atmospheric and surface radiance. Locations identified in the albedo map are for OMEGA orbit 1313 spectral reflectance data shown in Figure 2.9.

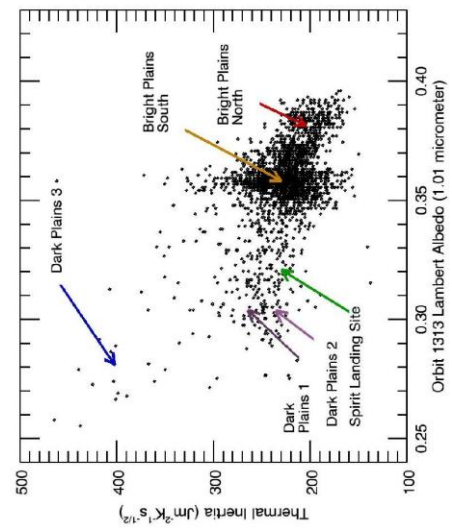
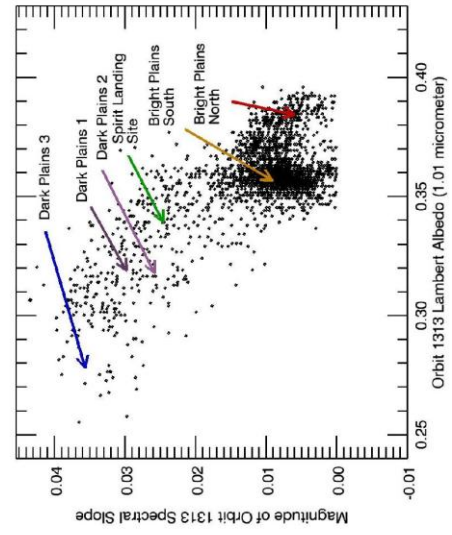
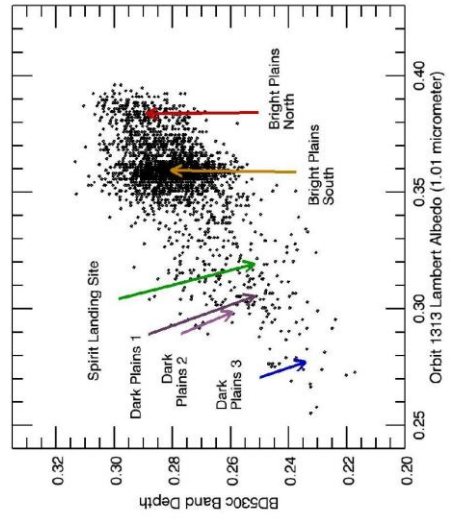


Figure 2.11: Plots of thermal inertia, magnitude of spectral slope, and BD530c band depth vs. 1.01- μm albedo. Arrows indicate the locations from which spectra shown in Figure 2.9d were derived. Trends support the hypothesis of two end-members: a nanophase iron-oxide-rich dust and a weakly-altered basaltic soil that is possibly mixed with a minor amount of dust.

Tables

Table 2.1. Date/time and viewing geometries for OMEGA and Spirit data shown in paper. i = Indicence Angle in degrees, e = Emission Angle in degrees, and g = Phase Angle in degrees.

Frame/Orbit	UTC ^a	LTST ^b	(i)	(e)	(g)	meters/pixel
OMEGA 0024_2	2004-01-16	Sol 13	25.3	23.5	48.5	403
	T11:44:13.031	13:50:06				
OMEGA 0072_1	2004-02-01	Sol 19	25.2	54.4	30.7	840
	T22:08:15.030	13:40:59				
OMEGA 0976_6	2004-10-23	Sol 286	70.5	4.5	66.8	375
	T00:56:31.045	14:53:18				
OMEGA 1313_2	2005-01-25	Sol 378	27.6	2.5	28.6	1076
	T09:42:09.010	11:03:13				
Pancam p2420, “Laguna Hollow”	2004-02-34	Sol 50	18	21		
Pancam p2556	2004-03-17	Sol 72	26.4	29		
Pancam p2575	2004-05-15	Sol 130	43.5	72.5		
Pancam p2574	2004-12-20	Sol 343	40	65		
Pancam p2536, “El Dorado”	2006-01-02	Sol 711	12.5	53.5		
Pancam p2460	2004-03-20	Sol 75	42.7	49.8		
Pancam p2460	2004-04-01	Sol 87	59.4	46.1		
Pancam p2460	2004-04-03	Sol 89	39.3	48.7		
Pancam p2460	2004-04-04	Sol 90	37.7	43.9		
Pancam p2460	2004-04-05	Sol 91	36.5	48.7		
Pancam p2460	2004-04-15	Sol 101	25.6	47.9		
Pancam p2460	2004-04-18	Sol 103	59.5	48.1		
Pancam p2460	2004-04-21	Sol 107	31.4	50		
Pancam p2460	2004-04-24	Sol 109	27.1	44.2		
Pancam p2460	2004-04-27	Sol 112	26.6	50.6		
Pancam p2460	2004-05-07	Sol 122	27	36.3		
Pancam p2460	2004-05-11	Sol 126	37.2	39		
Pancam p2460	2004-05-13	Sol 128	37.6	38.4		
Pancam p2460	2004-05-15	Sol 130	45.7	39.6		
Pancam p2460	2004-05-19	Sol 134	37.2	41.6		
Pancam p2460	2004-05-28	Sol 143	38	45.4		
Pancam p2460	2004-05-30	Sol 145	38	35.7		
Pancam p2460	2004-06-02	Sol 147	39.1	36.5		
Pancam p2460	2004-06-04	Sol 149	40.5	37.8		
Pancam p2460	2004-06-08	Sol 153	40.5	41.3		
Pancam p2460	2004-07-15	Sol 189	39.6	48.2		
Pancam p2460	2004-07-17	Sol 191	49.4	44.8		

^aUTC = Coordinated Universal Time

^bLTST = Local True Solar Time

Table 2.2. Lat/Lon coordinates of spectra shown in Figure 2.9.

Spectrum	OMEGA Orbit number	Identifier	Number of Pixels averaged	Latitude (degrees North)	Longitude (degrees East)
Apollinaris Patera	24	AP_24	5x5	-8.26	175.51
Bright Plains North	24	BPN_24	5x5	-13.41	175.47
Bright Plains South	24	BPS_24	5x5	-14.86	175.43
Spirit Landing Site	24	SLS_24	2x1	-14.57	175.47
Dark Plains	24	DP_24	3x3	-14.59	175.43
Apollinaris Patera	72	AP_72	5x5	-9.32	175.65
Bright Plains North	72	BPN_72	5x5	-13.51	175.67
Bright Plains South	72	BPS_72	5x5	-15.04	175.60
Spirit Traverse	72	ST_72	1x1	-14.61	175.52
Dark Plains	72	DP_72	3x3	-14.65	175.56
Apollinaris Patera	976	AP_976	5x5	-9.93	175.51
Bright Plains North	976	BPN_976	5x5	-14.04	175.49
Bright Plains South	976	BPS_976	5x5	-14.92	175.48
Spirit Landing Site	976	SLS_976	1x1	-14.63	175.49
Dark Plains	976	DP_976	3x3	-14.71	175.50
Apollinaris Patera	1313	AP_1313	2x2	-8.72	175.86
Bright Plains North	1313	BPN_1313	2x2	-13.92	175.29
Bright Plains South	1313	BPS_1313	2x2	-14.97	175.09
Spirit Landing Site	1313	SLS_1313	1x1	-14.59	175.47
Dark Plains (1)	1313	DP1_1313	2x2	-14.68	175.52
Dark Plains (2)	1313	DP2_1313	2x2	-14.97	174.79
Dark Plains (3)	1313	DP3_1313	2x2	-15.15	175.87

References

- Albee, A.L., R.E. Arvidson, F. Palluconi, and T. Thorpe (2001), Overview of the Mars Global Surveyor mission, *J. Geophys. Res.*, *106*(E10), 23291-23316.
- Arvidson, R.E., E. Guinness, M.A. Dale-Bannister, J.B. Adams, M. Smith, P.R. Christensen, and R.B. Singer (1989), Nature and distribution of surficial deposits in Chryse Planitia and vicinity, Mars, *J. Geophys. Res.*, *94*(B2), 1573-1587.
- Arvidson, R.E., R.C. Anderson, P. Bartlett, J.F. Bell III, D. Blaney, P.R. Christensen, P. Chu, L. Crumpler, K. Davis, B.L. Ehlmann, R.L. Fergason, M. Golombek, S. Gorevan, F.D. Grant, R. Greeley, E. Guinness, A.F.C. Haldemann, K.E. Herkenhoff, J.R. Johnson, G. Landis, R. Li, R. Lindemann, H.Y. McSween, D.W. Ming, T. Myrick, L. Richter, F. Seelos IV, S.W. Squyres, R. Sullivan, A. Wang, and J. Wilson (2004), Localization and physical properties experiments conducted by Spirit at Gusev Crater, *Science*, *305*, doi:10.1126/science.1099922.
- Arvidson, R.E., F. Poulet, R.V. Morris, J.-P. Bibring, J.F. Bell III, S.W. Squyres, P.R. Christensen, G. Bellucci, B. Gondet, B.L. Ehlmann, W.H. Farrand, R.L. Fergason, J.L. Griffes, J. Grotzinger, E. Guinness, K.E. Herkenhoff, J.R. Johnson, G. Klingelhofer, Y. Langevin, D.W. Ming, K. Seelos, R. Sullivan, J. Ward, S.M. Wiseman, and M. Wolff (2006a), Nature and Origin of the Hematite-Bearing Plains of Terra Meridiani Based on Analysis of Orbital and Mars Exploration Rover Data Sets, *J. Geophys. Res.*, *111*, E12S08, doi:10.1029/2006JE002728.
- Arvidson, R.E., S.W. Squyres, R.C. Anderson, J.F. Bell III, D. Blaney, J. Bruckner, N.A. Cabrol, W.M. Calvin, M.H. Carr, P.R. Christensen, B.C. Clark, L. Crumpler, D.J.

Des Marais, P.A. de Souza Jr., C. d'Uston, T. Economou, J. Farmer, W.H. Farrand, W. Folkner, M. Golombek, S. Gorevan, J.A. Grant, R. Greeley, J. Grotzinger, E. Guinness, B.C. Hahn, L. Haskin, K.E. Herkenhoff, J.A. Hurowitz, S. Hviid, J.R. Johnson, G. Klingelhofer, A.H. Knoll, G. Landis, C. Leff, M. Lemmon, R. Li, M.B. Madsen, M.C. Malin, S.M. McLennan, H.Y. McSween, D.W. Ming, J. Moersch, R.V. Morris, T. Parker, J.W. Rice Jr, L. Richter, R. Rieder, D.S. Rodionov, C. Schroder, M. Sims, M. Smith, P. Smith, L.A. Soderblom, R. Sullivan, S.D. Thompson, N.J. Tosca, A. Wang, H. Wanke, J. Ward, T. Wdowiak, M. Wolff, and A. Yen (2006b), Overview of the Spirit Mars Exploration Rover mission to Gusev Crater: Landing site to Backstay Rock in the Columbia Hills, *J. Geophys. Res.*, *111*, E02S01, doi:10.1029/2005JE002499.

Bell, J.F., R.V. Morris, and J.B. Adams (1993), Thermally altered palagonitic tephra - A spectral and process analog to the soil and dust of Mars, *J. Geophys. Res.*, *98*(E2), 3373-3385.

Bell, J.F., S.W. Squyres, R.E. Arvidson, H.M. Arneson, D. Bass, D. Blaney, N.A. Cabrol, W.M. Calvin, J. Farmer, W.H. Farrand, W. Goetz, M. Golombek, J.A. Grant, R. Greeley, E. Guinness, A. Hayes, M.Y.H. Hubbard, K.E. Herkenhoff, M.J. Johnson, J.R. Johnson, J. Joseph, K.M. Kinch, M. Lemmon, R. Li, M.B. Madsen, J.N. Maki, M.C. Malin, E. McCartney, S.M. McLennan, H.Y. McSween, D.W. Ming, J. Moersch, R.V. Morris, E.Z. Noe Dobrea, T. Parker, J. Proton, J.W. Rice Jr, F. Seelos IV, J. Soderblom, L.A. Soderblom, J.N. Sohl-Dickstein, R. Sullivan, M. Wolff, and A. Wang (2004), Pancam Multispectral Imaging Results from the

Spirit Rover at Gusev Crater, *Science*, 305, 800-806,

doi:10.1126/science.1100175.

Bell, J.F., J. Joseph, J.N. Sohl-Dickstein, H.M. Arneson, and M.J. Johnson (2006), In-flight calibration and performance of the Mars Exploration Rover Panoramic Camera (Pancam) instruments, *J. Geophys. Res.*, 111, E02S03, doi:10.1029/2005JE002444.

Bibring, J.-P., Y. Langevin, A. Gendrin, B. Gondet, F. Poulet, M. Berthe, A. Soufflot, R.E. Arvidson, N. Mangold, J. Mustard, P. Drossart, and The OMEGA team (2005), Mars Surface Diversity as Revealed by the OMEGA/Mars Express Observations, *Science*, 307, 1576-1581, doi:10.1126/science.1108806.

Christensen, P.R., S.W. Ruff, R.L. Fergason, A.T. Knudson, S. Anwar, R.E. Arvidson, J.L. Bandfield, D. Blaney, C. Budney, W.M. Calvin, T.D. Glotch, M. Golombek, N. Gorelick, T.G. Graff, V.E. Hamilton, A. Hayes, J.R. Johnson, H.Y. McSween, G.L. Mehall, L.K. Mehall, J. Moersch, R.V. Morris, A.D. Rogers, M. Smith, S.W. Squyres, M. Wolff, and M.B. Wyatt (2004a), Initial Results from the Mini-TES Experiment in Gusev Crater from the Spirit Rover, *Science*, 305, 837-842, doi:10.1126/science.1100564.

Christensen, P.R., S.W. Ruff, R.L. Fergason, N. Gorelick, B.M. Jakosky, M.D. Lane, A.S. McEwen, H.Y. McSween, G.L. Mehall, K.A. Milam, J. Moersch, S.M. Pelkey, A.D. Rogers, and M.B. Wyatt (2005), Mars Exploration Rover candidate landing sites as viewed by THEMIS, *Icarus*, 176, 12-43, doi:10.1016/j.icarus.2005.01.004.

- Clancy, R.T., M. Wolff, and P.R. Christensen (2003), Mars aerosol studies with the MGS TES emission phase function observations: Optical depths, particle sizes, and ice cloud types versus latitude and solar longitude, *J. Geophys. Res.*, *108*(E9), 5098, doi:10.1029/2003JE002058.
- Ferguson, R.L., P.R. Christensen, and H.H. Kieffer (2006a), High-resolution thermal inertia derived from the Thermal Emission Imaging System (THEMIS): Thermal model and applications, *J. Geophys. Res.*, *111*, E12004, doi:10.1029/2006JR002735.
- Ferguson, R.L., P.R. Christensen, J.F. Bell III, M. Golombek, K.E. Herkenhoff, and H.H. Kieffer (2006b), Physical properties of the Mars Exploration Rover landing sites as inferred from Mini-TES-derived thermal inertia, *J. Geophys. Res.*, *111*, E02S21, doi:10.1029/2005JE002583.
- Gellert, R., R. Reider, R.C. Anderson, J. Bruckner, B.C. Clark, G. Dreibus, T. Economou, G. Klingelhofer, G.W. Lugmair, D.W. Ming, S.W. Squyres, C. d'Uston, H. Wanke, A. Yen, and J. Zipfel (2004), Chemistry of Rocks and Soils in Gusev Crater from the Alpha Particle X-ray Spectrometer, *Science*, *305*, 829-832, doi:10.1126/science.1099913.
- Gendrin, A., N. Mangold, J.-P. Bibring, Y. Langevin, B. Gondet, F. Poulet, G. Bonello, C. Quantin, J. Mustard, R.E. Arvidson, and S. MeMouelic (2005), Sulfates in Martian layered terrains: The OMEGA/Mars Express view, *Science*, *307*, 1587-1591, doi:10.1126/science.1109087.
- Golombek, M., L. Crumpler, J.A. Grant, R. Greeley, N.A. Cabrol, T. Parker, J.W. Rice Jr, J. Ward, R.E. Arvidson, J. Moersch, R.L. Ferguson, P.R. Christensen, A.

- Castano, A.F.C. Haldemann, R. Li, J.F. Bell III, and S.W. Squyres (2006),
Geology of the Gusev cratered plains from the Spirit rover traverse, *J. Geophys. Res.*, *111*, E02S07, doi:10.1029/2005JE002503.
- Graff, T.G. (2003), Effects of Dust Coatings on Visible, Near-Infrared, Thermal
Emission and Mossbauer Spectra: Implications for Mineralogical Remote Sensing
of Mars, Masters thesis, Arizona State University, Tempe, AZ.
- Greeley, R., R.E. Arvidson, P.W. Barlett, D. Blaney, N.A. Cabrol, P.R. Christensen, R.L.
Ferguson, M. Golombek, G. Landis, M. Lemmon, S.M. McLennan, J.N. Maki, T.
Michaels, J. Moersch, L.D.V. Neakrase, S.C.R. Rafkin, L. Richter, S.W. Squyres,
P.A. de Souza Jr., R. Sullivan, S.D. Thompson, and P.L. Whelley (2006), Gusev
Crater: Wind-related features and processes observed by the Mars Exploration
Rover Spirit, *J. Geophys. Res.*, *111*, E02S09, doi:10.1029/2005JE002491.
- Herkenhoff, K.E., S.W. Squyres, R.E. Arvidson, D. Bass, J.F. Bell III, P. Bertelsen, N.A.
Cabrol, L.R. Gaddis, A. Hayes, S. Hviid, J.R. Johnson, K.M. Kinch, M.B.
Madsen, J.N. Maki, S.M. McLennan, H.Y. McSween, J.W. Rice Jr, M. Sims, P.H.
Smith, L.A. Soderblom, N. Spanovich, R. Sullivan, and A. Wang (2004),
Textures of the soils and rocks at Gusev Crater from Spirit's Microscopic Imager,
Science, *305*, 824-826, doi: 10.1126/science.3050824.
- Jakosky, B.M., B.M. Hynek, S.M. Pelkey, M.T. Mellon, S. Martinez-Alonso, N.E.
Putzig, N. Murphy, and P.R. Christensen (2006), Thermophysical properties of
the MER and Beagle II landing site regions on Mars, *J. Geophys. Res.*, *111*,
doi:10.1029/2004JE002320.

- Johnson, J.R., and W.M. Grundy (2001), Visible/Near-Infrared Spectra and Two-Layer Modeling of Palagonite-Coated Basalts, *Geophys. Res. Lett.*, 28(10), 2101-2104.
- Johnson, J.R., P.R. Christensen, and P.G. Lucey (2002), Dust coatings on basaltic rocks and implications for thermal infrared spectroscopy of Mars, *J. Geophys. Res.*, 107(E6), doi:10.1029/2000JE001405.
- Johnston, M.D.D., J.E. Graf, R.W. Zurek, H.J. Eisen, and B. Jai (2005), The Mars Reconnaissance Orbiter Mission, in *IEEE Conference*, pp. 447-464.
- Kuzmin, R.O., R. Greeley, R. Landheim, N.A. Cabrol, and J. Farmer (2000), Geologic Map of the MTM-15182 and MTM-15187 Quadrangles, Gusev Crater-Ma'adim Vallis Region, Mars, in *U. S. Geological Survey Geologic Investigations Series I-2666*.
- Langevin, Y., F. Poulet, J.-P. Bibring, and B. Gondet (2005), Sulfates in the north polar region of Mars detected by OMEGA/Mars Express, *Science*, 307, 1584-1586, doi:10.1126/science.1109091.
- Lemmon, M., M. Wolff, M.D. Smith, R.T. Clancy, D. Banfield, G. Landis, A. Ghosh, P.H. Smith, N. Spanovich, B. Whitney, P.L. Whelley, R. Greeley, S.D. Thompson, J.F. Bell III, and S.W. Squyres (2004), Atmospheric Imaging Results from the Mars Exploration Rovers: Spirit and Opportunity, *Science*, 306(5702), 1753-1756, doi:10.1126/science.1104474.
- Li, R., K. Di, L.H. Matthies, R.E. Arvidson, W. Folkner, and B.A. Archinal (2004), Rover localization and landing-site mapping technology for the 2003 Mars Exploration Rover mission, *Photogrammetric Engineering and Remote Sensing*, 70(1), 77-90.

- Martinez-Alonso, S., B.M. Jakosky, M.T. Mellon, and N.E. Putzig (2005), A volcanic interpretation of Gusev crater surface materials from thermophysical, spectral, and morphological evidence, *J. Geophys. Res.*, *110*, E01003, doi:10.1029/JE002327.
- McSween, H.Y., R.E. Arvidson, J.F. Bell III, D. Blaney, N.A. Cabrol, P.R. Christensen, B.C. Clark, J.A. Crisp, L. Crumpler, D.J. Des Marais, J. Farmer, R. Gellert, A. Ghosh, S. Gorevan, T.G. Graff, J.A. Grant, L. Haskin, K.E. Herkenhoff, J.R. Johnson, B.L. Joliff, G. Klingelhofer, A.T. Knudson, S.M. McLennan, K.A. Milam, J. Moersch, R.V. Morris, R. Rieder, S.W. Ruff, P.A. de Souza Jr., S.W. Squyres, H. Wanke, A. Wang, M.B. Wyatt, A. Yen, and J. Zipfel (2004), Basaltic Rocks Analyzed by the Spirit Rover in Gusev Crater, *Science*, *305*, 842-845, doi:10.1126/science.3050842.
- McSween, H.Y., M.B. Wyatt, R. Gellert, J.F. Bell III, R.V. Morris, K.E. Herkenhoff, L. Crumpler, K.A. Milam, K.R. Stockstill, L.L. Tornabene, R.E. Arvidson, P. Bartlett, D. Blaney, N.A. Cabrol, P.R. Christensen, B.C. Clark, J.A. Crisp, D.J. Des Marais, T. Economou, J. Farmer, W.H. Farrand, A. Ghosh, M. Golombek, S. Gorevan, R. Greeley, V.E. Hamilton, J.R. Johnson, B.L. Joliff, G. Klingelhofer, A.T. Knudson, S.M. McLennan, D.W. Ming, J. Moersch, R. Reider, S.W. Ruff, C. Schroder, P.A. de Souza Jr., S.W. Squyres, H. Wanke, A. Wang, A. Yen, and J. Zipfel (2006), Characterization and petrologic interpretation of olivine-rich basalts at Gusev crater, Mars, *J. Geophys. Res.*, *111*, E02S10, doi:10.1029/2005JE002477.

- Mellon, M.T., B.M. Jakosky, H.H. Kieffer, and P.R. Christensen (2000), High-Resolution Thermal Inertia Mapping from the Mars Global Surveyor Thermal Emission Spectrometer, *Icarus*, *148*, 437-455, doi:10.1006/icar.2000.6503.
- Milam, K.A., K.R. Stockstill, J. Moersch, H.Y. McSween, L.L. Tornabene, A. Ghosh, M.B. Wyatt, and P.R. Christensen (2003), THEMIS characterization of the Mer Gusev crater landing site, *J. Geophys. Res.*, *108*(E12), doi:10.1029/2002JE002023.
- Ming, D.W., D.W. Mittlefehldt, R.V. Morris, D.C. Golden, R. Gellert, A. Yen, B.C. Clark, S.W. Squyres, W.H. Farrand, S.W. Ruff, R.E. Arvidson, G. Klingelhofer, H.Y. McSween, D.S. Rodionov, C. Schroder, P.A. de Souza Jr., and A. Wang (2006), Geochemical and mineralogical indicators for aqueous processes in the Columbia Hills of Gusev crater, Mars, *J. Geophys. Res.*, *111*, E02S12, doi:10.1029/2005JE002560.
- Morris, R.V., D.C. Golden, J.F. Bell III, H.V. Lauer, and J.B. Adams (1993), Pigmenting agents in Martian soils: Inferences from spectral, Mossbauer, and magnetic properties of nanophase and other iron oxides in Hawaiian palagonitic soil PN-9, *Geochim. Cosmochim. Acta*, *57*, 4597-4609.
- Morris, R.V., D.C. Golden, and J.F. Bell III (1997), Low-temperature reflectivity spectra of red hematite and the color of Mars, *J. Geophys. Res.*, *102*(E4), 9125-9133, doi:10.1029/96JR03993.
- Morris, R.V., D.C. Golden, J.F. Bell III, T.D. Shelfer, A.C. Scheinost, N.W. Hinman, G. Furniss, S.A. Mertzman, J.L. Bishop, D.W. Ming, C.C. Allen, and D.T. Britt (2000), Mineralogy, composition, and alteration of Mars Pathfinder rocks and

soils; Evidence from multispectral, elemental, and magnetic data on terrestrial analogue, SNC meteorite, and Pathfinder samples, *J. Geophys. Res.*, *105*(E1), 1757-1817, doi:10.1029/1999JE001059.

Morris, R.V., G. Klingelhofer, C. Schroder, D.S. Rodionov, A. Yen, D.W. Ming, P.A. de Souza Jr., I. Fleischer, T. Wdowiak, R. Gellert, B. Bernhardt, E.N. Evlanov, B. Zubkov, J. Foh, U. Bonnes, E. Kankeleit, P. Gutlich, F. Renz, S.W. Squyres, and R.E. Arvidson (2006a), Mossbauer mineralogy of rock, soil, and dust at Gusev crater, Mars: Spirit's journey through weakly altered olivine basalt on the plains and pervasively altered basalt in the Columbia Hills, *J. Geophys. Res.*, *111*, E02S13, doi:10.1029/2005JE002584.

Morris, R.V., G. Klingelhofer, C. Schroder, D.S. Rodionov, A. Yen, D.W. Ming, P.A. de Souza Jr., I. Fleischer, T. Wdowiak, R. Gellert, B. Bernhardt, U. Bonnes, B.A. Cohen, E.N. Evlanov, J. Foh, P. Gutlich, E. Kankeleit, T. McCoy, D.W. Mittlefehldt, F. Renz, M.E. Schmidt, B. Zubkov, S.W. Squyres, and R.E. Arvidson (2006b), Mossbauer mineralogy of rock, soil, and dust at Meridiani Planum, Mars: Opportunity's journey across sulfate-rich outcrop, basaltic sand and dust, and hematite lag deposits, *J. Geophys. Res.*, *111*, E12S15, doi:10.1029/2006JE002791.

Mustard, J., F. Poulet, A. Gendrin, J.-P. Bibring, Y. Langevin, B. Gondet, N. Mangold, G. Bellucci, and F. Altieri (2005), Olivine and pyroxene diversity in the crust of Mars, *Science*, *307*, 1594-1597, doi:10.1126/science.1109098.

- Piatek, J.L., and J. Moersch (2007), Thermophysical Analysis of Debris Aprons in Eastern Hellas using THEMIS, in *Lunar and Planetary Science Conference XXXVIII*, 2281.
- Poulet, F., J.-P. Bibring, J. Mustard, A. Gendrin, N. Mangold, Y. Langevin, R.E. Arvidson, B. Gondet, C. Gomez, and T.O. Team (2005), Phyllosilicates on Mars and implications for early Martian climate, *Nature*, 438, 623-627, doi:10.1038/nature04274.
- Poulet, F., C. Gomez, J.-P. Bibring, Y. Langevin, B. Gondet, P.C. Pinet, G. Bellucci, and J. Mustard (2007), Martian surface mineralogy from Observatoire pour la Mineralogie, l'Eau, les Glaces et l'Activite on board the Mars Express spacecraft (OMEGA/MEx): Global mineral maps, *J. Geophys. Res.*, 112, E08S02, doi:10.1029/2006JE002840.
- Putzig, N.E., and M.T. Mellon (2007), Apparent thermal inertia and the surface heterogeneity of Mars, *Icarus*, *In press*, doi:10.1016/j.icarus.2007.05.013.
- Saunders, R.S., R.E. Arvidson, G.D. Badhwar, W.V. Boynton, P.R. Christensen, F.A. Cucinotta, W.C. Feldman, R.G. Gibbs, C. Kloss Jr., M.R. Landano, R.A. Mase, G.W. McSmith, M.A. Meyer, I.G. Mitrofanov, G.D. Pace, J.J. Plaut, W.P. Sidney, D.A. Spencer, T.W. Thompson, and C.J. Zeitlin (2004), 2001 Mars Odyssey Mission Summary, *Space Sci. Rev.*, 110, 1-36.
- Smith, M.D., M. Wolff, N. Spanovich, A. Ghosh, D. Banfield, P.R. Christensen, G. Landis, and S.W. Squyres (2006), One Martian year of atmospheric observations using MER Mini-TES, *J. Geophys. Res.*, 111, E12S13, doi:10.1029/2006JE002770.

Squyres, S.W., R.E. Arvidson, J.F. Bell III, J. Bruckner, N.A. Cabrol, W.M. Calvin, M.H. Carr, P.R. Christensen, B.C. Clark, L. Crumpler, D.J. Des Marais, C. d'Uston, T. Economou, J. Farmer, W.H. Farrand, W. Folkner, M. Golombek, S. Gorevan, J.A. Grant, R. Greeley, J. Grotzinger, L. Haskin, K.E. Herkenhoff, S. Hviid, J.R. Johnson, G. Klingelhofer, A.H. Knoll, G. Landis, M. Lemmon, R. Li, M.B. Madsen, M.C. Malin, S.M. McLennan, H.Y. McSween, D.W. Ming, J. Moersch, R.V. Morris, T. Parker, J.W. Rice Jr, L. Richter, R. Rieder, M. Sims, P. Smith, L.A. Soderblom, R. Sullivan, H. Wanke, T. Wdowiak, M. Wolff, and A. Yen (2004a), The Spirit Rover's Athena Science Investigation at Gusev Crater, Mars, *Science*, 305, 794-799.

Squyres, S.W., R.E. Arvidson, J.F. Bell III, J. Bruckner, N.A. Cabrol, W.M. Calvin, M.H. Carr, P.R. Christensen, B.C. Clark, L. Crumpler, D.J. Des Marais, C. d'Uston, T. Economou, J. Farmer, W.H. Farrand, W. Folkner, M. Golombek, S. Gorevan, J.A. Grant, R. Greeley, J. Grotzinger, L. Haskin, K.E. Herkenhoff, S. Hviid, J.R. Johnson, G. Klingelhofer, A.H. Knoll, G. Landis, M. Lemmon, R. Li, M.B. Madsen, M.C. Malin, S.M. McLennan, H.Y. McSween, D.W. Ming, J. Moersch, R.V. Morris, T. Parker, J.W. Rice Jr, L. Richter, R. Rieder, M. Sims, M. Smith, P. Smith, L.A. Soderblom, R. Sullivan, H. Wanke, T. Wdowiak, M. Wolff, and A. Yen (2004b), The Opportunity Rover's Athena Science Investigation at Meridiani Planum, Mars, *Science*, 306(5702), 1698-1703.

Stamnes, K., S.-C. Tsay, W. Wiscombe, and K. Jayaweera (1988), Numerically stable algorithm for discrete-ordinate-method radiative transfer in multiple scattering and emitting layered media, *Applied Optics*, 27(12), 2502-2509.

Wolff, M., M.D. Smith, R.T. Clancy, N. Spanovich, B. Whitney, M. Lemmon, J.L.

Bandfield, D. Banfield, A. Ghosh, G. Landis, P.R. Christensen, J.F. Bell III, and S.W. Squyres (2006), Constraints on dust aerosols from the Mars Exploration Rovers using MGS overflights and MIni-TES, *J. Geophys. Res.*, *111*, E12S17, doi:10.1029/2006JE002786.

Yen, A., R. Gellert, C. Schroder, R.V. Morris, J.F. Bell III, A.T. Knudson, B.C. Clark,

D.W. Ming, J.A. Crisp, R.E. Arvidson, D. Blaney, J. Bruckner, P.R. Christensen, D.J. Des Marais, P.A. de Souza Jr., T. Economou, A. Ghosh, B.C. Hahn, K.E. Herkenhoff, L. Haskin, J.A. Hurowitz, B.L. Joliff, J.R. Johnson, G. Klingelhofer, M.B. Madsen, S.M. McLennan, H.Y. McSween, L. Richter, R. Reider, D.S. Rodionov, L.A. Soderblom, S.W. Squyres, N.J. Tosca, A. Wang, M.B. Wyatt, and J. Zipfel (2005), An integrated view of the chemistry and mineralogy of martian soils, *Nature*, *436*, 49-54, doi:10.1038/nature03637.

Chapter 3. Rover Mobility: A Modeling Perspective

3.1 Introduction

The Mars Exploration Rover [MER] Spirit's capability as a mobile spacecraft has deteriorated as the vehicle has experienced wear and tear over its six years on the surface of Mars [Arvidson *et al.*, 2006; 2008; 2010]. The MER rovers employ a rocker-bogie suspension system designed to allow the rovers to experience 45° of tilt without overturning and to scale obstacles up to 20cm (nearly 1 wheel diameter) [Lindemann and Voorhees, 2005]. Each wheel is independently driven and the gears cannot be disengaged, so the loss of an actuator results in a dead weight that must be pushed or dragged [Lindemann and Voorhees, 2005]. After over six years of operation, two of Spirit's six drive actuators are inoperable and the current embedding in Troy means that Spirit may have reached its final resting place [Arvidson *et al.*, 2010].

The ability to recognize and mitigate mobility issues is important not only for the current MER rovers but also for future Mars rovers such as the 2011 Mars Science Laboratory and 2018 ExoMars and future lunar rovers. Here we address the recognition of potential mobility issues through the generation and use of hazard maps in support of drive planning, and quantify mobility performance using commercially-available software and a model of Spirit to: 1. explore the effect of material properties on rover mobility using Coulomb and Stribeck theory to model the contacts between wheels and soil, 2. gain insight into operating in usual mobility circumstances such as driving with five wheels, and 3. estimate the magnitude of the rolling resistance not taken into account in the Coulomb/Stribeck contact model.

During the first 156 sols of the mission, Spirit was driving across the cratered plains of Gusev Crater (Fig. 3.1) which have previously been shown to be comprised of basaltic sands covered with a thin layer of nano-phase iron oxide (dust) [Chapter 2 and *Lichtenberg et al.*, 2007]. Mobility while driving across these terrains was good as evidenced by the equally-spaced wheel tracks, including marks from the tie-down cleats, and minimal sinkage (Fig. 3.2). Testing prior to landing indicated that a six-wheeled rover would have little-to-no slippage in similar material (beach sand) on flat slopes, although there was increased slippage as the slopes increased (slopes up to 25° were tested) [*Lindemann and Voorhees*, 2005]. Spirit's scientific results and overall mobility between landing and third winter are summarized in Arvidson [2006] and Arvidson [2008]; here we focus on Spirit's mobility issues from Winter Haven 3 (~sol 1700) onward (Fig. 3.3). Arvidson et al. [2010] summarize operations and scientific results from this latter period of time.

3.2 Spirit Mobility

Spirit's right-front (RF) wheel drive actuator failed on sol 787 after descending from the Columbia Hills into the Inner Basin and, with only 5 working wheels, mobility became more challenging. Multiple attempts were made to have Spirit drive clockwise around the northeastern corner of Home Plate, which was the desired path to Goddard and Von Braun for the fourth winter. The soil covered ridges proved too much for Spirit and the rover experienced sinkage, high slip, clockwise yaw about the right front wheel, and downhill slip (e.g. Edmund Hamilton, Fig. 3.4) [*Arvidson et al.*, 2010]. After extensive discussion between the science and engineering teams, the decision was made to traverse

counter-clockwise around the northwest corner of Home Plate and drive south through the western valley.

The western valley was imaged in detail when Spirit was on the western edge of Home Plate, but there was still concern that the soil and substrate characteristics for this valley were unknown. After the mobility issues associated with driving clockwise around Home Plate, the MER project enlisted the help of the scientists to create mobility hazard maps in order to avoid driving over terrains that had potential for high slippage or sinkage [Lichtenberg *et al.*, 2010]. The goal of the hazard maps was to indicate where to expect good, fair, and poor mobility based on remote sensing from the rover with improved mapping based on actual traverses over the mapped units. These maps were iterated with MER rover drivers and were used in tactical drive planning from leaving Edmund Hamilton on sol 1837 until the embedding in Troy.

The hazard maps are intended to provide a clear, simple, and unambiguous assessment of anticipated terrain navigability by combining terrain slopes, terrain type, and experience of how the rover behaves in each to create a color map where green indicates good mobility, yellow indicates fair, and red indicates the likelihood of poor mobility. Examples of a base image and the corresponding inputs and resulting hazard map are shown in Figures 3.5 and 3.6. Specifically, terrain slopes are retrieved automatically from stereo Navcam pairs typically taken at the end of a drive in the anticipated direction of the next drive. Absolute slopes and slopes radially away from the rover are two of the available products, and both can be used depending on the terrain situation. Discussions with scientists and rover drivers resulted in the following terrain classifications: Outcrop, Soil over bedrock, Soil with embedded rock clasts, Soil with

ripple morphology, Soil no rocks, and Big rocks/Boulder fields (Fig. 3.6). Since parts of the rover and/or the sky can be present in the images, a transparent classification called Sky or Rover is also used in the analysis to mask those areas. Classifying the terrain into the constituent types is not automatic yet, so for tactical planning this was done manually in ArcMap (a GIS application) using separate shapefiles for each terrain class and the topology feature in ArcMap to insure that the classes don't overlap. Future efforts may focus on spectral properties and shape recognition to automate terrain mapping.

The experience of the team with over 1300 sols of 5-wheeled driving was utilized to create the stoplight chart in Figure 3.6. This is where the slopes are divided into classes in 4 degree increments (<0, 0-4, 4-8, 8-12, 12-16, and >16 degrees) and each intersection of slope class and terrain type is assigned a color: green for previous good mobility in that terrain type on those slopes, yellow for previous mobility challenges, and red for either previous mobility hazards or being outside rover specifications. The slopes are then input into ArcMap, classified, intersected with the terrain types, and the new shapefiles are assigned green, yellow, or red based on the stoplight chart and overlain onto the original Navcam image.

Despite the hazard maps and other analysis tools, a plethora of orbital data, and 5+ years of experience driving Spirit, the sub-surface material in Troy was not detected before being excavated by Spirit. This and other mobility-impairment situations (e.g. Tyrone; Purgatory, with Opportunity) indicate that despite early reconnaissance, challenging mobility situations cannot always be anticipated.

3.3 Modeling and Application to Mobility

Understanding mobility issues requires understanding how the wheels, suspension, and body of a rover (i.e. the overall system) interact with a surface or surfaces. For the analyses presented in the rest of this chapter, we used a modeling environment to gain insight into rover-surface interactions.

3.3.1 Modeling Software: MSC Adams

Adams/View is a commercially available software package by MSCSoftware that is used to model mechanical systems. The software's primary purpose is to model physical interactions between mechanical parts, but it also has the capability to model interactions between a mechanical system and its physical environment. A post processing application within Adams allows for easy filtering and visualization of plots and animations.

Prior to launch, the MER team at JPL created a mechanical model of Spirit and Opportunity in Adams in order to test the mechanical system, but it also enabled the team to test and characterize the rovers' response to various terrains and situations [Lindemann, 2005; Lindemann and Voorhees, 2005]. During the extrication effort, the MER model in Adams was updated to more accurately model the drive actuators and to be more visually representative of the flight models (Fig. 3.7). The analyses in this paper were conducted using this MER model in Adams/View and Adams/PostProcessor 2008 R3.

3.3.2 Wheel-Soil Contacts

The model for contacts between wheels and soil in this analysis is based on classical physics and work by Stribeck in the early 1900's [*Stribeck*, 1902a; *Stribeck*, 1902b]. Adams models contact forces using a non-linear spring-damper system to model normal forces and Stribeck theory to model frictional contacts. The normal force generated by a contact between surfaces is a combination of stiffness (spring effect) and damping (dashpot effect):

$$F = Kx^e - (c_{max} \text{ at penetration } d) \frac{dx}{dt}$$

where the stiffness (K) models the elasticity of the surface, the force exponent (e) governs the contribution of the material stiffness to the instantaneous normal force, the damping (c_{max}) models the dissipation of energy, and the max depth (d) is the depth at which the damping reaches its maximum. For friction forces, $F_f = \mu N$ and Stribeck theory is used to govern the transition between static and dynamic states of friction as shown in Figure 3.8. Numerical models have difficulty with sharp transitions between behaviors, however, so stiction and friction transition velocities specify where the transitions from no motion to static and from static to dynamic states occur (Fig. 3.8). Ideally 'no motion' is the same as static, therefore the stiction transition velocity should be as small as possible while allowing the model to remain numerically stable. Each contact between the mechanical system (e.g.. rover wheel) and its environment (e.g. the terrain) is given its own set of user-input parameters that are used to govern the contact forces (Table 3.1).

The limitations of this contact model are that it does not track the deformation of the terrain, each contact is only one single point of contact (rather than multiple contacts with individual properties or a continuum), and it does not take into account the effects of

soil compression or bulldozing. Even with these limitations, the model is adequate for exploring mobility issues.

3.3.3 Assessing Impaired Mobility with Spirit

After the right-front drive actuator failed, it became customary to drive the rover backward in order to mitigate the effect on overall rover mobility. Since the arm of the rocker suspension system that links the RF wheel to the body of the rover is angled upward toward the body (Fig. 1.1), pulling rather than pushing the wheel lessens the normal force that the inoperable wheel exerts on the terrain. This in turn decreases the friction force between the wheel and terrain since the friction force is related to the normal force and material properties in Mohr-Coulomb theory by:

$$F_{S,\max} = F_N \tan \Phi + C$$

where C is the soil cohesion, F_n is the normal shear stress due to the weight of the rover on the wheel, Φ is the soil angle of internal friction, and $\tan \Phi$ is static coefficient of friction. Values for cohesion and angle of internal friction (i.e., to determine the effective static coefficient of friction) were adopted from earlier trenching experiments done by Spirit and are 1 to 5 KPa and 30 degrees, respectively [Sullivan *et al.*, 2010]. In order to quantify the difference in normal and frictional forces on the RF wheel between driving forward and backward and between five-wheeled and six-wheeled driving, we simulated all four cases using a model of Spirit (Fig. 3.7). In all cases driving forward resulted in higher normal force (and therefore higher frictional force) on the RF wheel than driving backward, as shown in Figures 3.9 and 3.10. With the RF wheel deactivated, however, the normal and frictional forces on the RF wheel during forward driving are increased

over the 6-wheel driving case (Figs. 3.9 and 3.10). In addition, forward 5-wheel driving resulted in a periodic oscillation in the force on the RF wheel which we attribute to stick-slip motion on that wheel.

3.4 Spirit's Embedding in Troy

After successfully navigating around the northwestern corner of Home Plate and traveling some meters south, Spirit skirted the edge of a bowl-shaped depression ("Scamander Plains") (Fig. 3.11) and broke through a thin surface crust revealing a high-albedo sandy material. After a few sols of maneuvering, four of Spirit's six wheels were partially-to-completely buried and percent slip during both turning and driving was on the order of 95-98% (Fig. 3.12). Additionally, images taken of the underbelly of the rover with the Microscopic Imager on the arm showed that the warm electronics box (WEB) may have been high-centered on a rock. Realizing the severity of Spirit's situation, the team temporarily halted driving on sol 1899 to conduct ground-based testing and devise an extrication plan.

Driving resumed in November 2009 on Spirit sol 2088. On the list of possible maneuvers was to press the Instrument Deployment Device (IDD, Fig. 1.1) against the ground to help pull or push the rover while driving. However, this maneuver would risk damaging one or more of the scientific instruments at the end of the arm as well as the joints on the arm, so it would only be attempted if the team was convinced that the added force from the arm could actually have an effect on the motion of the rover.

Without a fully dynamical simulation involving deformable soils, the rolling resistance incurred by the embedded state of Spirit's left-side wheels and right-rear wheel

in Troy is impossible to simulate in the current Adams model. However, the magnitude of the rolling resistance—in other words, the force that would be needed to overcome to induce rover movement—can be estimated by providing a force opposite to the rover’s drive direction (e.g. a spring) that exactly cancels out the rover’s movement (Fig. 3.13). This estimation depends on accurately gauging the coefficients of friction for the Troy material as that will affect the force at which the rover’s wheels turn without any forward motion of the rover. Using measured angles of repose of disturbed Troy material (~32-35°) and assuming that the material is cohesionless, the static coefficient of friction of the material can be derived using Mohr-Coulomb theory which yields a coefficient of friction of ~0.6. This was the number input into the soil contacts for each of the six wheels in Adams, along with typical values governing how the normal force is generated (Table 3.1). The resulting force on the spring is ~421 N as shown in Figure 3.14; the IDD with a known frictional force of ~70 N (max. normal force of ~100 N) would not result in any rover movement.

The IDD is irreplaceable so attempting to push with the IDD, even in the testbed environment, was deemed expensive and risky. The modeling analysis presented here helped save a valuable scientific resource and gave the team confidence that it was doing the right thing by not risking the IDD in what would have been, as demonstrated above, a futile effort.

3.5 Looking Forward

The problematic sulfate-rich materials in Troy were not detected prior to their excavation with either orbital data or with Spirit's instruments. This indicates that despite

careful analysis of orbital data over future landing sites, the surface below the top few centimeters must be treated as an unknown quantity when attempting to forecast a rover's drive performance. In addition, the most scientifically interesting locations within the landing ellipse may prove to be the most difficult to traverse.

An effort to incorporate a deformable soils model with deformation history for use with Adams/View is currently underway using the semi-empirical Bekker equations and theory by Wong [*Bekker*, 1956; 1969; *Wong*, 2008]. In the long term, we anticipate that the project will become part of the overall effort in path planning and navigation for both Martian and lunar rovers.

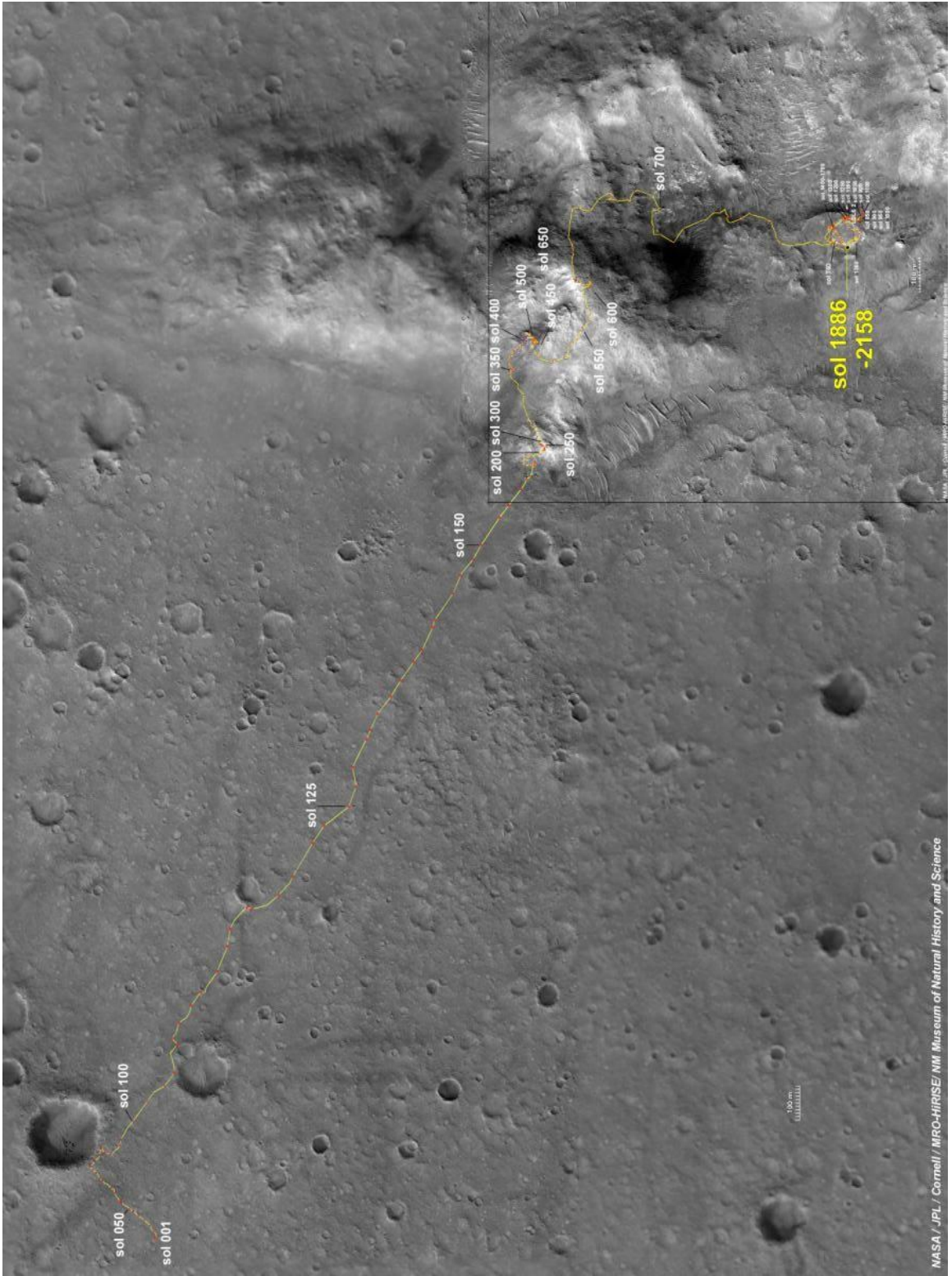


Figure 3.1: Map of Spirit's traverse from landing through sol 2158 (February 2010).

Spirit left the plains and entered the Columbia Hills around sol 180. (Image credit:

NASA/JPL/Cornell/MRO-HiRISE/NM Museum of Natural History and Science)

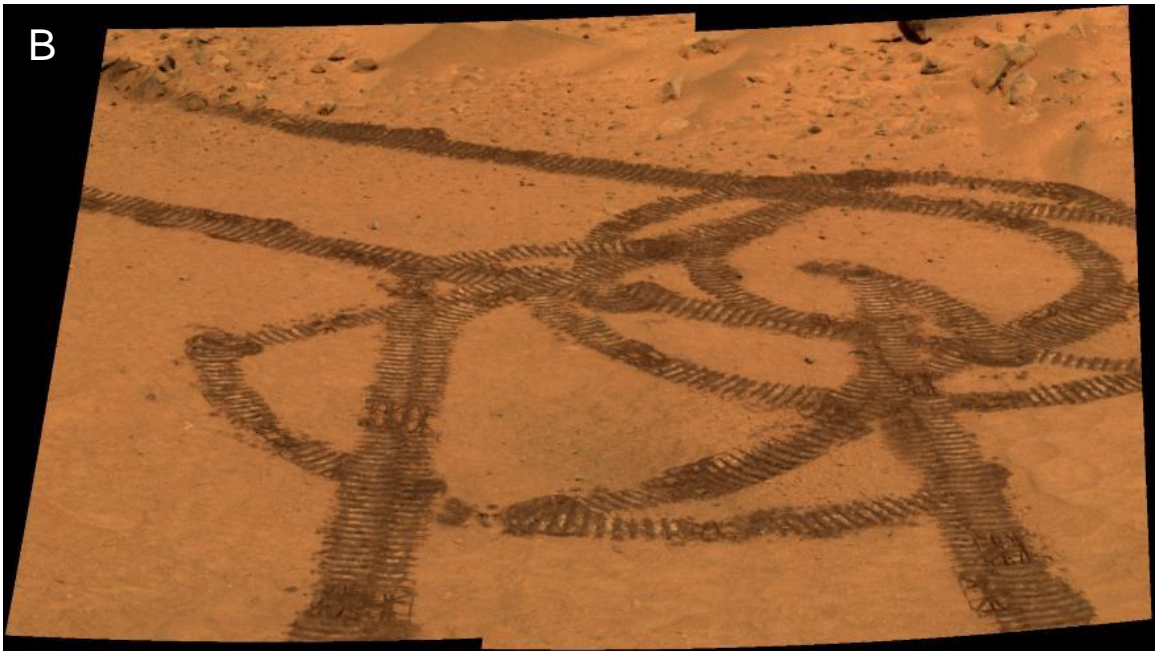
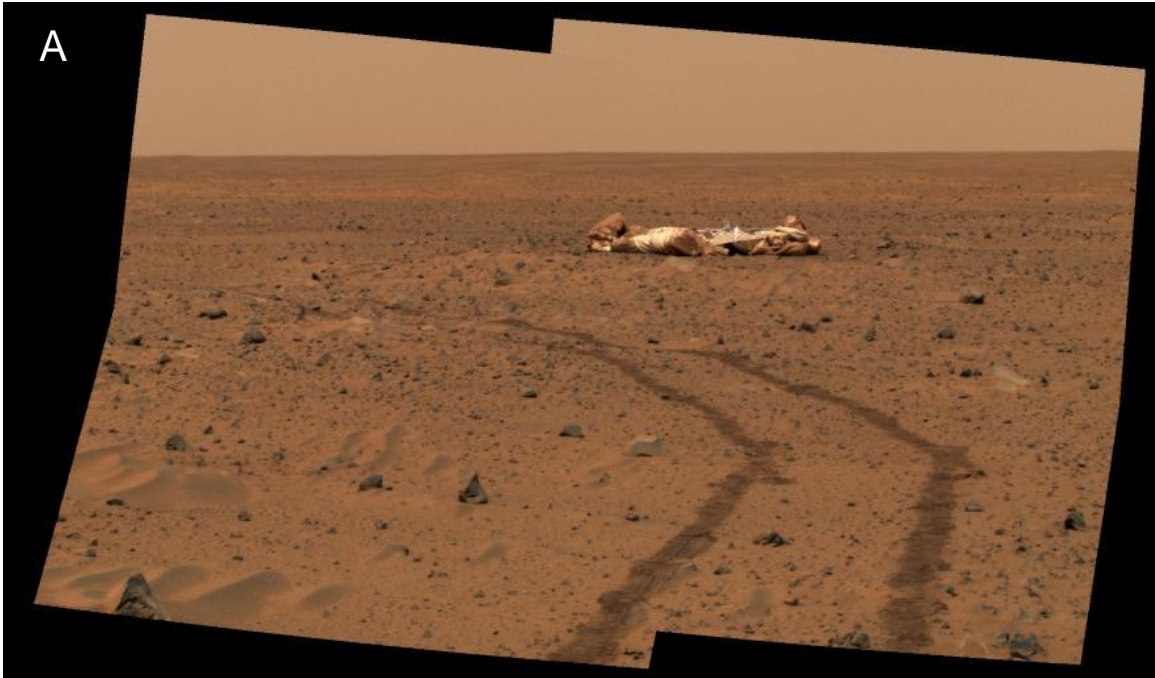


Figure 3.2: Pancam images of Spirit wheel tracks indicating good mobility. The top image (A) was acquired on sol 42 and shows the lander with deflated airbags. The bottom image (B) was taken on sol 58 and shows the tracks from a “turn in place”.

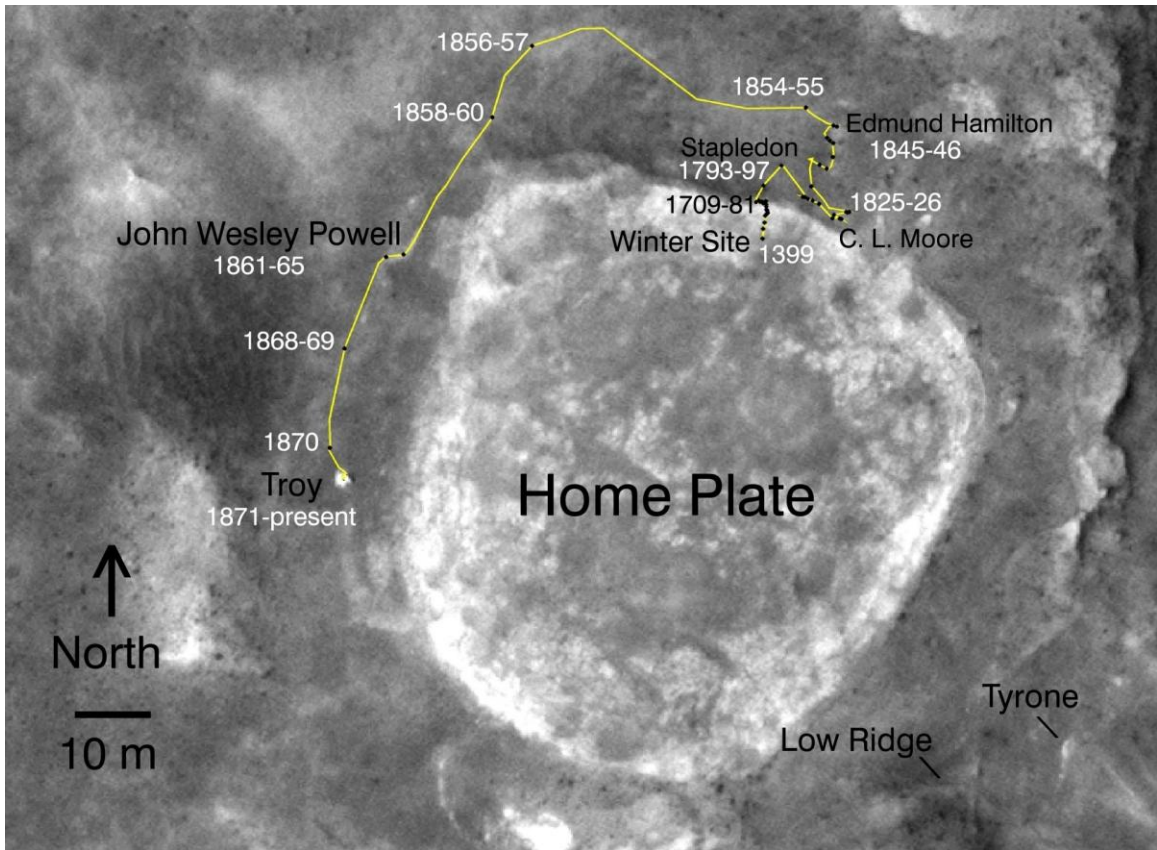


Figure 3.3: HiRISE image with Spirit's path from the Winter Haven 3 site on the north side of Home Plate to the current location in Troy overlain.

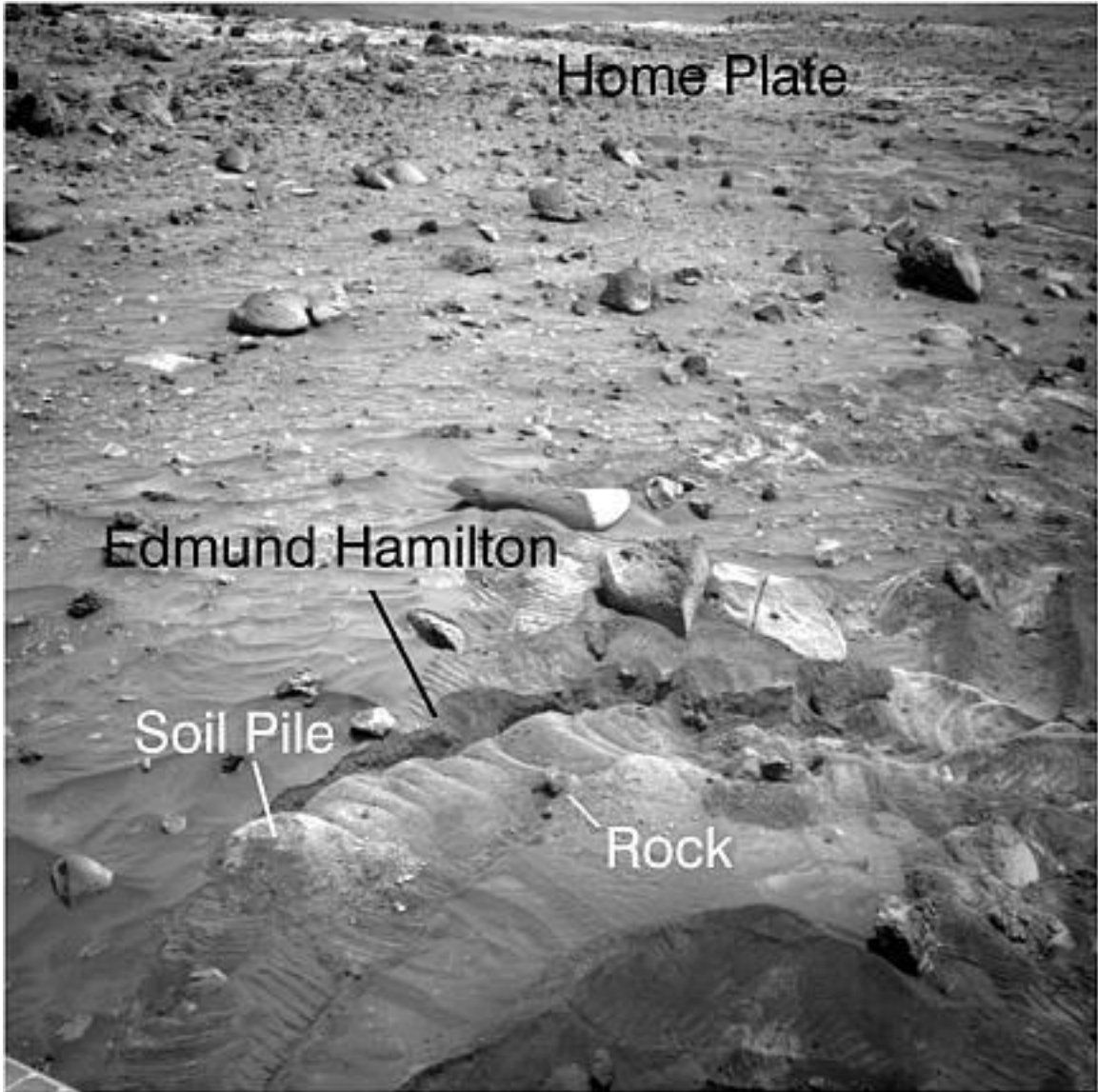


Figure 3.4: Navcam showing the disturbed area “Edmund Hamilton”. The mobility issues experienced in this area are evidenced by the lack of tie-down cleat imprints and the soil waves in the disturbed area.

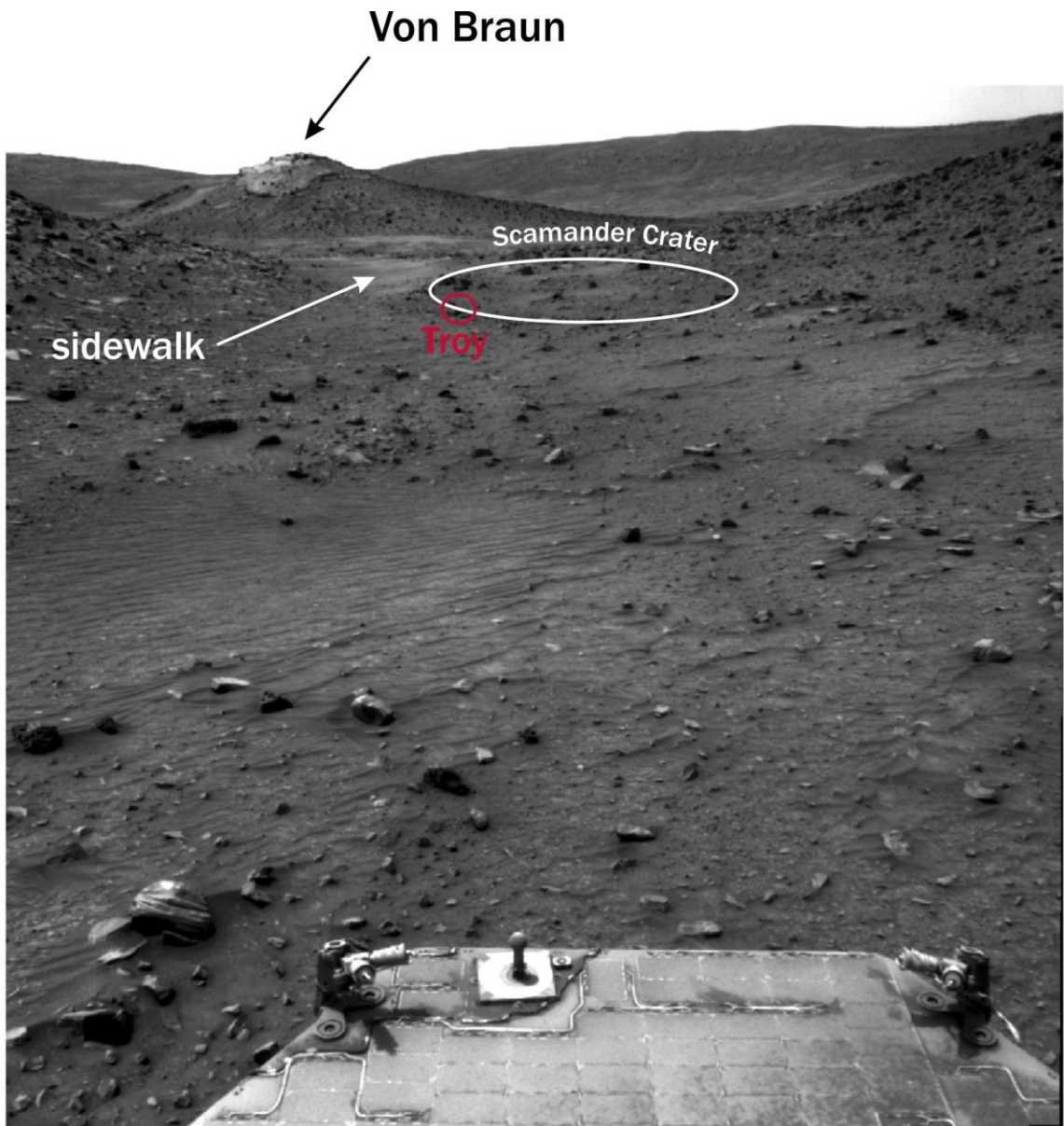


Figure 3.5: Navcam p0703 (frame 2N292280989) from sol 1869 showing Scamander Crater, the sidewalk, and Spirit's current location, Troy. This image is the basis for the Hazard Map analysis shown in Figure 3.6.

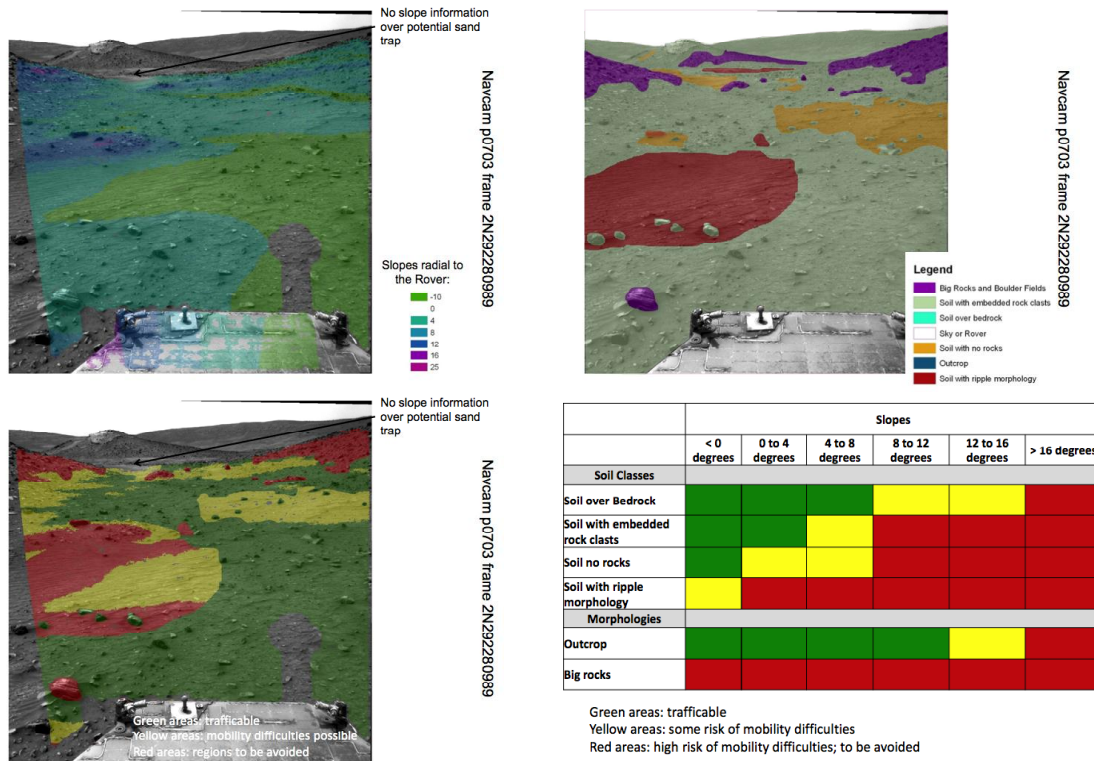


Figure 3.6: Example of a Hazard Map. The inputs to the hazard map are terrain slopes derived from stereo imaging (top left) and terrain classification/soil types (top right). The intersection of slope + terrain type results in the hazard map (bottom left), which is classified according to the stoplight chart (bottom right).

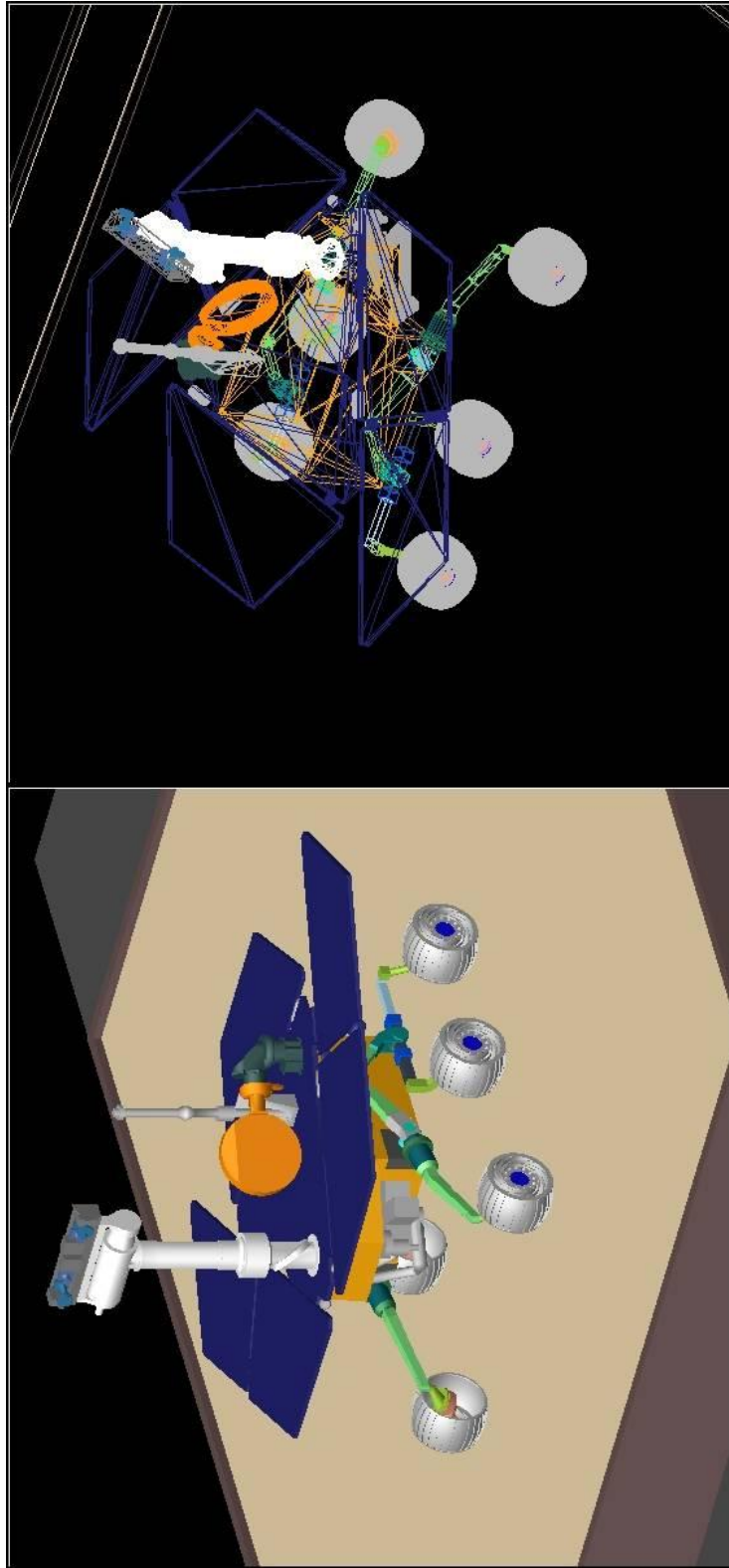


Figure 3.7: (left) Rendered model of MER in Adams/View; (right) wireframe model of MER in Adams/View.

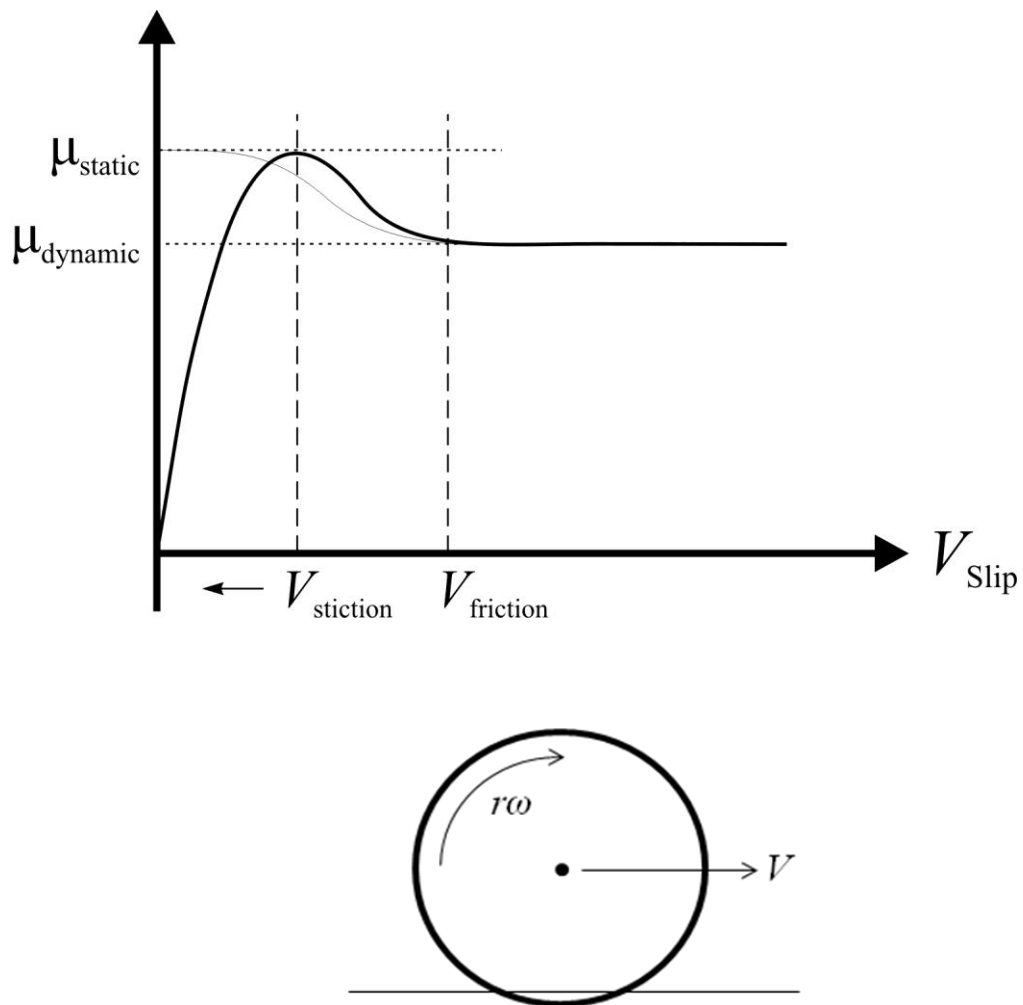


Figure 3.8: (top) "Real" Stribeck curve (light gray line, after [Stribeck, 1902a; Stribeck, 1902b]) vs. the modified Stribeck curve (black line) used in Adams. V_{stiction} should be as small as possible while allowing the model to remain numerically stable in order to come as close to the "real" Stribeck curve as possible. On the x-axis, $V_{\text{slip}} = r\omega - V$ as defined in the bottom figure.

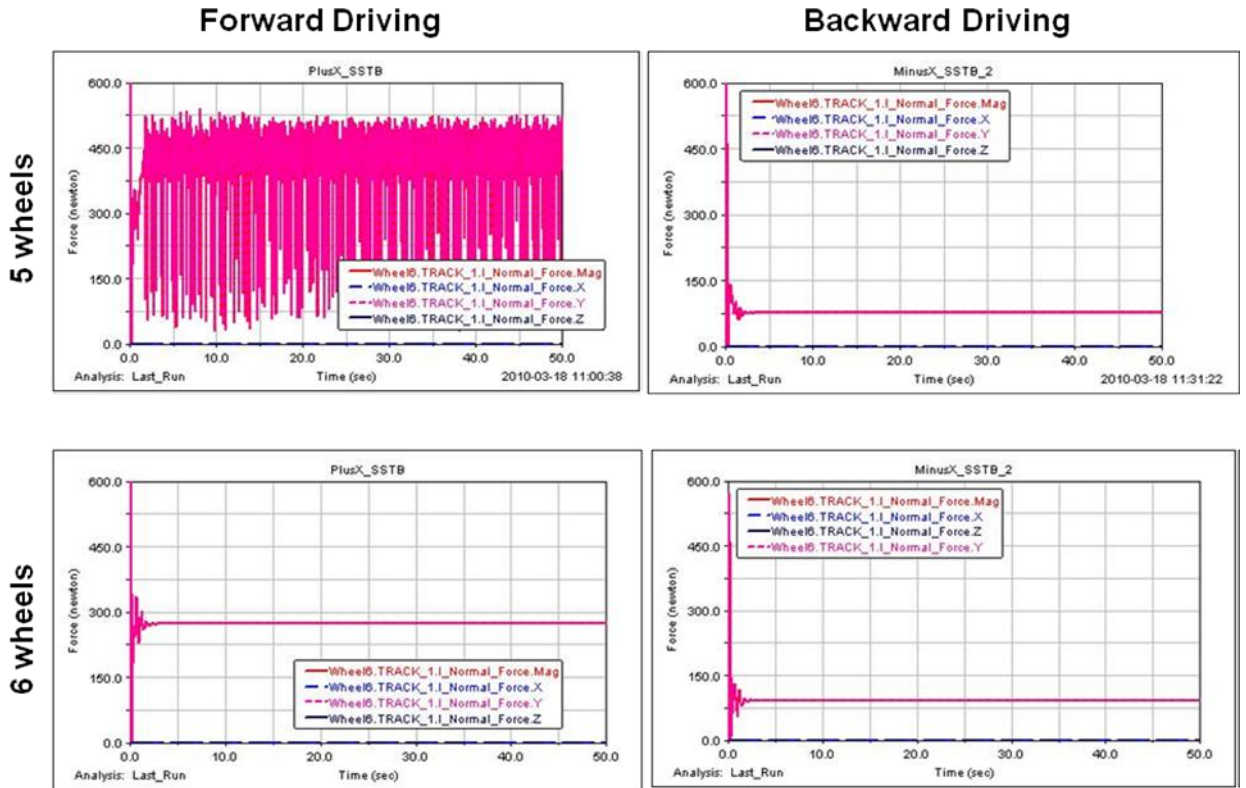


Figure 3.9: Normal forces on the right-front wheel. All drives were for 2 meters on a flat surface, with wheel velocity commanded to 3.88 cm/sec. In this coordinate system, X is in the drive direction, Y is in the direction of gravity (up/down), and Z is from side to side. Plotted are the magnitude of the normal force on the right front wheel as well as the force broken down into its constituent components.

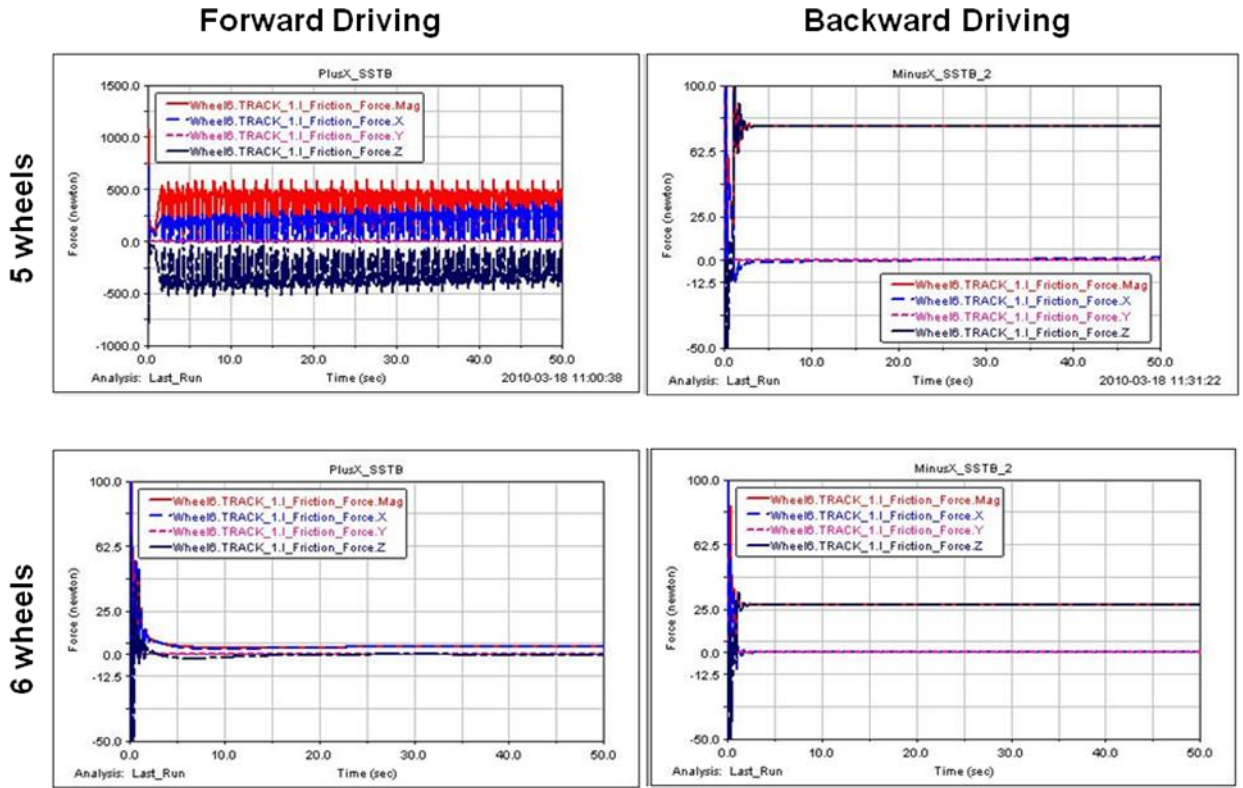


Figure 3.10: Frictional forces on the right-front wheel. Parameters are the same as in Figure 3.9. Plotted are the magnitude of the frictional force on the right front wheel as well as the force broken down into its constituent components.

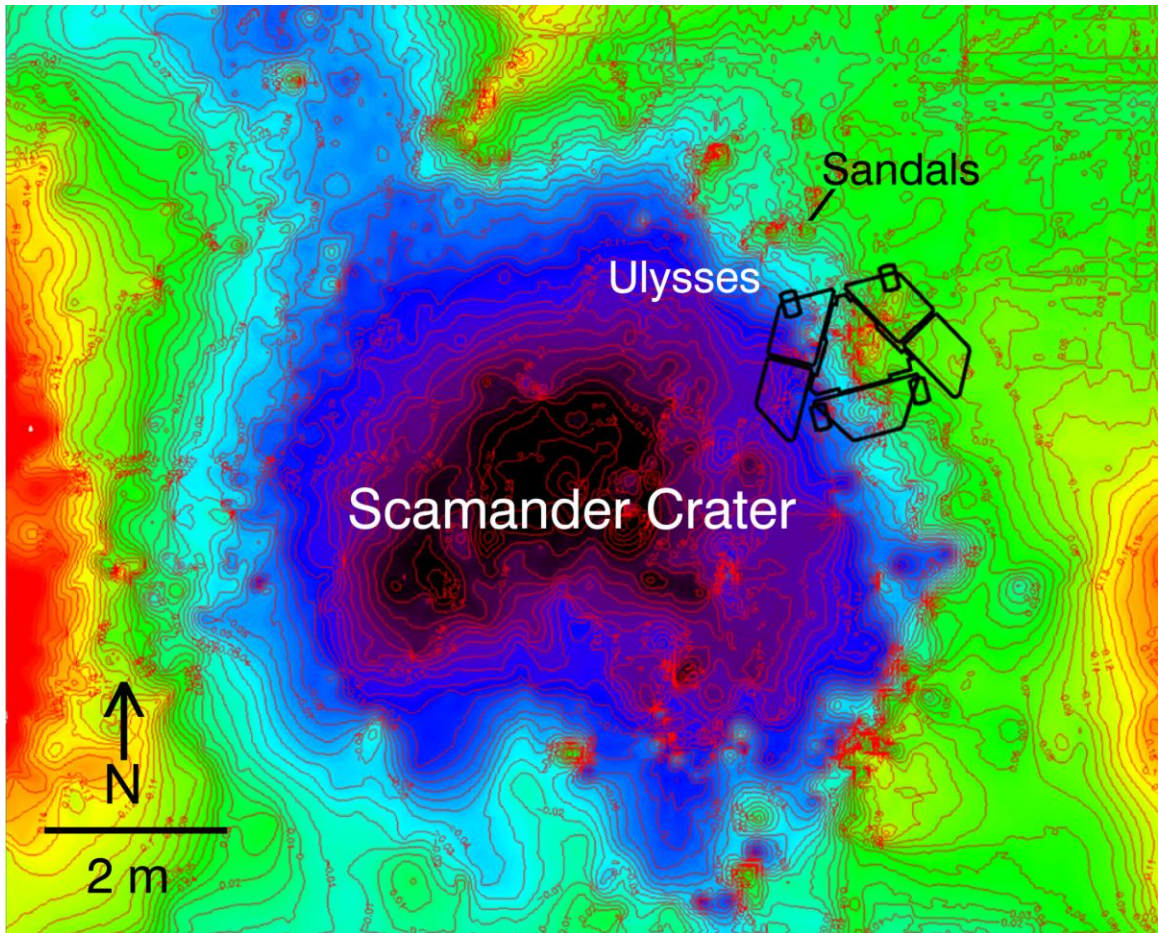


Figure 3.11: Topographic map for the Scamander Crater area generated from Navcam image mosaics in the sol 1870 drive direction. Relief is approximately 3 meters with warm colors indicating high elevations and cool colors indicating low elevations. Ulysses and the Sandals indicate where Spirit conducted an extensive scientific campaign during driving stand-down between sols 1899 and 2088 [Arvidson *et al.*, 2010].



Figure 3.12: Front Hazcam showing the severity of embedding in Troy. The left-front wheel should be visible, but it is completely buried in the trench of high-albedo cohesionless sands. This image was taken on sol 2154.

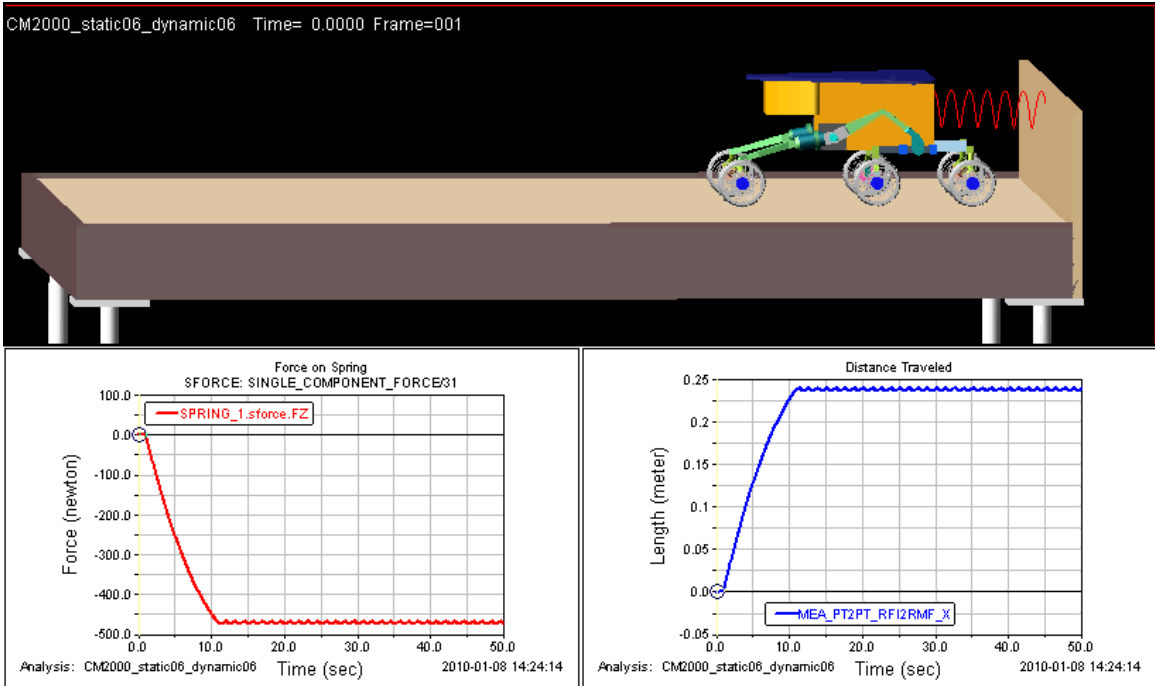


Figure 3.13: Schematic showing the rover-spring set-up in Adams. The graph on the bottom left shows the horizontal force on the spring as a function of time; negative indicates extension. The graph on the right shows rover distance driven vs. time. The graphs together show that the force on the spring reaches a maximum when the rover stops making forward progress, i.e. the wheels are still turning but the rover remains stationary.

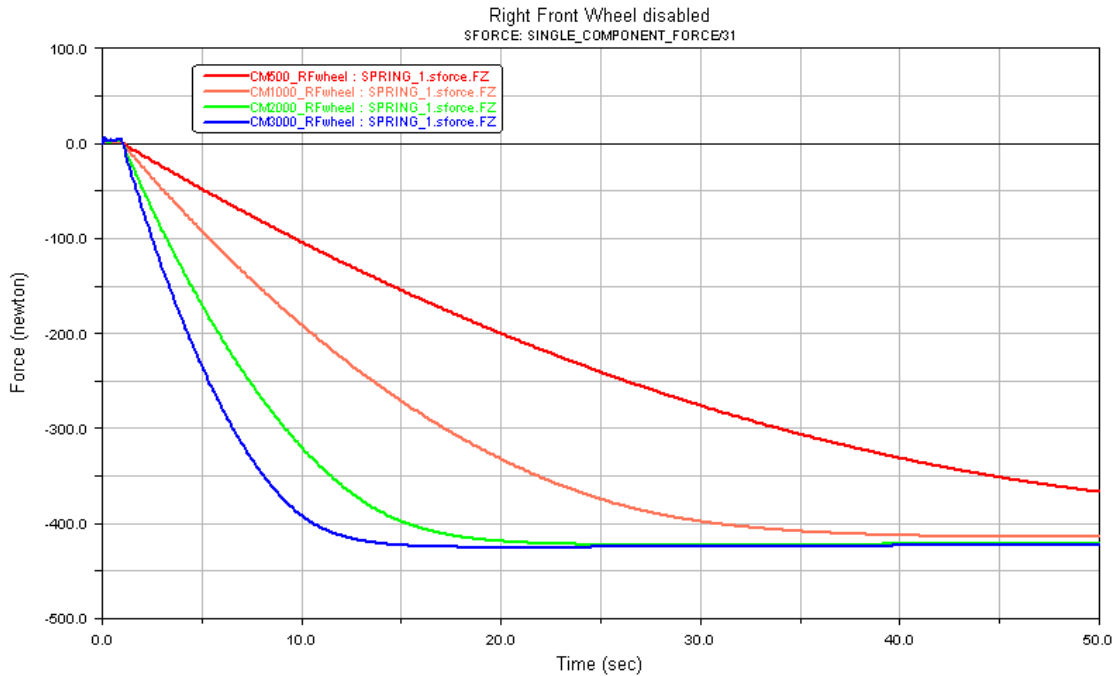


Figure 3.14: Graph showing the force exerted on the spring by the rover shown in Figure 3.13; in this experiment, the rover is driving with 5 wheels. The spring constant is varied as follows: red = 500, orange = 1000, green = 2000, and blue = 3000 N/m. The difference in spring constants translates into different distances driven before the force on the spring reaches the point at which it exactly opposes the frictional force generated between the wheels and the soil, i.e. the wheels turn but the rover no longer has any forward motion. The force on all but the red (500 N/m) spring asymptote to ~421 N; with additional drive time and distance the force on the 500 N/m spring would reach 421 N as well. For this experiment, static and dynamic coefficients of friction for all 6 wheel contacts were set to 0.6.

Tables

Table 3.1 Contact parameters used in Adams and typical values

Name	Symbol	Typical Value	Units
Coefficient of Friction (static)	μ_S	0.6	(dimensionless)
Coefficient of Friction (dynamic)	μ_D	0.3	(dimensionless)
Stiction transition velocity	V_{stiction}	0.0035	meters/sec
Friction transition velocity	V_{friction}	0.035	meters/sec
Stiffness	K	1000000	(dimensionless)
Force exponent	e	2.2	(dimensionless)
Damping	c_{max}	814.0	(dimensionless)
Penetration depth	d	0.0001	meters

References

- Arvidson, R.E., J.F. Bell III, P. Bellutta, N.A. Cabrol, L. Crumpler, T. Estlin, W.H. Farrand, R. Gellert, J.A. Grant, R. Greenberger, E. Guinness, K.E. Herkenhoff, J. Hermann, K. Iagnemma, J.R. Johnson, G. Klingelhofer, R. Li, K.A. Lichtenberg, S.A. Maxwell, D.W. Ming, R.V. Morris, M. Rice, S.W. Ruff, A. Shaw, K. Siebach, P.A. de Souza Jr., A. Stroupe, S.W. Squyres, K. Tally, J. Townsend, A. Wang, J. Wright, and A. Yen (2010), Spirit Mars Rover Mission: Overview and Selected Results from the Northern Home Plate Winter Haven to the Side of Scamander Crater, *J. Geophys. Res.*, Manuscript in preparation.
- Arvidson, R.E., S.W. Ruff, R.V. Morris, D.W. Ming, L. Crumpler, A. Yen, S.W. Squyres, R.J. Sullivan, J.F. Bell III, N.A. Cabrol, B.C. Clark, W.H. Farrand, R. Gellert, R. Greenberger, J.A. Grant, E. Guinness, K.E. Herkenhoff, J.A. Hurowitz, J.R. Johnson, G. Klingelhofer, K.W. Lewis, R. Li, T. McCoy, J. Moersch, H.Y. McSween, S.L. Murchie, M.E. Schmidt, C. Schroder, A. Wang, S.M. Wiseman, M.B. Madsen, W. Goetz, and S.M. McLennan (2008), Spirit Mars Rover Mission to the Columbia Hills, Gusev Crater: Mission overview and selected results from the Cumberland Ridge to Home Plate, *J. Geophys. Res.*, 113, E12S33, doi:10.1029/2008JE003183.
- Arvidson, R.E., S.W. Squyres, R.C. Anderson, J.F. Bell III, D.L. Blaney, J. Bruckner, N.A. Cabrol, W.M. Calvin, M.H. Carr, P.R. Christensen, B.C. Clark, L. Crumpler, D. Des Marais, P.A. de Souza Jr., D. d'Uston, T. Economou, J. Farmer, W.H. Farrand, W. Folkner, M. Golombek, S. Gorevan, J.A. Grant, R. Greeley, J.P. Grotzinger, E. Guinness, B.C. Hahn, L. Haskin, K.E. Herkenhoff, J.A. Hurowitz,

S. Hviid, J.R. Johnson, G. Klingelhofer, A.H. Knoll, G. Landis, C. Leff, M. Lemmon, R. Li, M.B. Madsen, M.C. Malin, S.M. McLennan, H.Y. McSween, D.W. Ming, J. Moersch, R.V. Morris, T. Parker, J.W. Rice Jr, L. Richter, R. Rieder, D.S. Rodionov, C. Schroder, M. Sims, M. Smith, P. Smith, L.A. Soderblom, R.J. Sullivan, S.D. Thompson, N.J. Tosca, A. Wang, H. Wanke, J.G. Ward, T. Wdowiak, M. Wolff, and A. Yen (2006), Overview of the Spirit Mars Exploration Rover Mission to Gusev Crater: Landing site to Backstay Rock in the Columbia Hills`, *J. Geophys. Res.*, *111*, E02S01, doi:10.1029/2005JE002499.

Bekker, M.G., *Theory of Land Locomotion*, University of Michigan Press, Ann Arbor, MI, 1956.

Bekker, M.G., *Introduction to Terrain-Vehicle Systems*, University of Michigan Press, Ann Arbor, MI, 1969.

Lichtenberg, K.A., R.E. Arvidson, R. Lindemann, K. Iagnemma, K. Bennett, B. Trease, L. Richter, and M. Scharringhausen (2010), Rover mobility at the "Troy" site, Mars: a modeling perspective, *41st Lunar and Planetary Conference*, Houston, TX, Abstract # 2295.

Lichtenberg, K.A., R.E. Arvidson, F. Poulet, R.V. Morris, A. Knudson, J.F. Bell III, G. Bellucci, J.-P. Bibring, W.H. Farrand, J.R. Johnson, D.W. Ming, P.C. Pinet, A.D. Rogers, and S.W. Squyres (2007), Coordinated analyses of orbital and Spirit Rover data to characterize surface materials on the cratered plains of Gusev Crater, Mars, *J. Geophys. Res.*, *112*, E12S90, doi:10.1029/2006JE002850.

- Lindemann, R. (2005), Dynamic testing and simulation of the Mars Exploration Rover, *ASME International Design Engineering Technical Conferences and Computers and Information in Engineering Conference*, Long Beach, CA.
- Lindemann, R.A., and C.J. Voorhees (2005), Mars Exploration Rover mobility assembly design, test and performance, *2005 International Conference on Systems, Man, and Cybernetics*, Hawaii.
- Stribeck, R. (1902a), Die wesentlichen Eigenschaften der Gleit- und Rollenlager -- The key qualities of sliding and roller bearings, *Zeitschrift des Vereines Deutscher Ingenieure*, 46, 38, 1342-48.
- Stribeck, R. (1902b), Die wesentlichen Eigenschaften der Gleit- und Rollenlager -- The key qualities of sliding and roller bearings, *Zeitschrift des Vereines Deutscher Ingenieure*, 46, 39, 1432-37.
- Sullivan, R.J., R.C. Anderson, J. Biesiadecki, T. Bond, L. Brock, H. Stewart, and C. Weinstein (2010), Cohesions, friction angles, and other physical properties of martian regolith from MER wheel trenches and wheel scuffs, *J. Geophys. Res.*, Manuscript in preparation.
- Wong, J.Y., *Theory of Ground Vehicles*, John Wiley & Sons, Inc., Ottawa, Canada, 2008.

Chapter 4. Stratigraphy of Hydrated Sulfates in the Sedimentary Deposits of Aram Chaos, Mars

Journal of Geophysical Research, doi:10.1029/2009JE003353, in press.

© Copyright 2010 by the American Geophysical Union

4.1 Introduction

The discovery from orbit of layered sedimentary hydrated sulfate deposits in analyses of Mars Express Observatoire pour la Minéralogie, l'Eau, les Glaces et l'Activité (OMEGA) data [Gendrin *et al.*, 2005; Arvidson *et al.*, 2006], subsequently confirmed and extended in analyses of Mars Reconnaissance Orbiter (MRO) Compact Reconnaissance Imaging Spectrometer for Mars (CRISM) data [Murchie *et al.*, 2009; Roach *et al.*, 2009], has revolutionized our understanding of the evolution of Mars. The measurements obtained by the Mars Exploration Rover Opportunity during its exploration of the top of a thick sequence of sulfate-rich deposits in Meridiani Planum provide a detailed view of the depositional environment of these types of deposits. Specifically, results point to an acid-sulfate-dominated lacustrine system alternating with more arid conditions in which aeolian deposits accumulated [Squyres *et al.*, 2004; Grotzinger *et al.*, 2005; Tosca and McLennan, 2006]. With continued groundwater rise on a regional level the deposits were cemented and preserved [Arvidson *et al.*, 2006; Andrews-Hanna *et al.*, 2007].

In this paper we build on previous studies of Aram Chaos [Gendrin *et al.*, 2005; Glotch and Christensen, 2005; Masse *et al.*, 2008b; Noe Dobra *et al.*, 2008] by

contributing (a) detailed mapping of the layered deposits using a combination of MRO Context Imager (CTX) with 5 m/pixel data [Malin *et al.*, 2007], High Resolution Imaging Science Experiment (HiRISE) data with 0.31 m/pixel observations [McEwan *et al.*, 2007], Mars Orbiter Laser Altimeter (MOLA) data at ~465 m/pixel [Smith *et al.*, 2001], and Mars Express High Resolution Stereo Camera (HRSC) topographic data at 75 m/pixel [Neukum *et al.*, 2004]; and (b) retrieval of mineral compositions for the stratigraphic units using CRISM hyperspectral targeted mode observations at ~20 and 40 m/pixel [Murchie *et al.*, 2007]. For reference, Figure 4.1 presents a regional-scale view of Aram Chaos, Figure 4.2a shows results from mapping mineralogy from OMEGA and TES data, and Figure 4.2b shows detailed mapping that we have done using the high resolution CRISM observations. Figure 4.3 summarizes the key stratigraphic and mineralogic relationships developed in this paper, including the first identification on Mars of the ferric hydroxysulfate- $\text{Fe}(\text{OH})\text{SO}_4$ -located at and near the contact between the sedimentary deposits and the underlying chaos bedrock surface.

4.2 Geologic setting

Aram Chaos (~3°N, 339°E), contained within a 280 km wide crater of Noachian age, is one of a number of chaotic regions located in Xanthe Terra. Chaos terrain is characterized by a series of plateaus and mesas separated by valleys that form a mosaic pattern (Figure 4.1) [Rodriguez *et al.*, 2005]. The likely chaos formation mechanism involved catastrophic outflow of pressurized groundwater, either through melting of subsurface ice or liquefaction [Carr, 1979; Nummedal and Prior, 1981; Rodriguez *et al.*, 2005]. The outflow of water that created the sunken chaos blocks also carved the channel

on the east side of the crater and then joined other material flowing north in Ares Vallis [Nummedal and Prior, 1981]. After the initial chaos-forming event(s), subsequent aqueous activity in the area changed from erosion to deposition, producing the layered sedimentary materials that unconformably overlie the chaos bedrock materials [Glotch and Christensen, 2005; Oosthoek et al., 2007]. At some point post-deposition the area experienced an uplift, creating a domical structure within Aram Crater [Glotch and Christensen, 2005; Oosthoek et al., 2007; Masse et al., 2008b]. The layered deposits have experienced significant differential wind erosion, revealing stratigraphic layers of differing morphology, thermal inertia, and mineral composition (including gray crystalline hematite, nanophase ferric oxides (npOx), and hydrated sulfates materials) [Gendrin et al., 2005; Glotch and Christensen, 2005; Glotch and Rogers, 2007; Masse et al., 2008b; Noe Dobrea et al., 2008]. The erosion was driven by winds trending from the northwest which formed elongated plateaus of partially eroded sedimentary materials running NW-SE (Figures 4.1 and 4.2) [Oosthoek et al., 2007]. As noted by Fenton and Richardson [2001], wind directions have been to first order invariant as Mars has moved through its orbital oscillations. Thus, these northwesterly winds have been active for a large fraction of geologic time.

4.3 Methodology

4.3.1 Orbital Datasets

We use an integrated data processing and geographic information system (GIS) approach using both ENVI and ArcMap commercial software packages. MOLA and HRSC topographic data, CTX images, and HiRISE images over the study area were map-

projected to an equidistant cylindrical (equirectangular) projection using a Mars radius of 3396.0 km (scales for each data set were commensurate with their intrinsic spatial resolution). The data sets were then incorporated into an ArcMap pyramid-structured database, which allowed co-visualization of the all data sets with user-selected transparency values. CRISM data (observation footprints, false-color images, and mineral detections) were added to the GIS system, and the combination of the spectral processing capability of ENVI and the map capabilities of ArcMap was used to map superposition and embayment relationships, morphologic characteristics, and mineral inferences of the various layered units superimposed on the basement chaos materials.

CRISM is a hyperspectral imager that can acquire up to 544 spectral channels between 0.39 to 3.9 μm with two detectors: a short-wavelength detector that functions between 0.39 and 1.04 μm (S-detector) and a long-wavelength detector that functions from 1.0 to 3.9 μm (L-detector) [Murchie *et al.*, 2007]. CRISM has two operational modes: a hyperspectral targeted mode (FRT) and a multispectral nadir-looking mode (MSP). The multispectral mode is designed to provide mineralogical information for as much of the surface as possible, whereas the hyperspectral mode is designed to probe the mineralogy of relatively small areas in great detail. In the hyperspectral mode, gimbaling allows the instrument to be pointed at specific locations to the left or right of the spacecraft track while acquiring data at full spectral (544 bands, 0.39-3.9 μm) resolution and either full or half spatial resolution (~ 18 or ~ 40 m/pixel, respectively) [Murchie *et al.*, 2007]. Multiple images are taken on the incoming and outgoing spacecraft track to sample different path lengths through the atmosphere, but in this paper only the center

observation is used. Targeted observations cover $\sim 1300 \text{ km}^2$ of the sedimentary deposit in Aram Chaos.

CRISM data presented in this paper were converted to I/F by dividing radiance-on-sensor by the solar radiance. Atmospheric gas band absorptions were removed by normalizing to a gas transmission spectrum. This spectrum, from data acquired over Olympus Mons where the surface spectra are dominated by dust signatures, is obtained by dividing I/F values at the base of Olympus Mons by values at the summit. The variation in atmospheric path length from the base to the top of the volcano provides a transmission spectrum which can then be used to remove gas features from other spectra. This method has been used extensively in reduction of hyperspectral data [*Langevin et al.*, 2005; *Mustard et al.*, 2005; *Lichtenberg et al.*, 2007], and here is applied to L-detector data only because that is the spectral region in which atmospheric gas bands are present. At wavelengths shorter than $\sim 1 \mu\text{m}$, atmospheric effects are dominated by aerosols and we did not correct for these effects. Both L- and S-detector observations were photometrically corrected by dividing by the cosine of the incidence angle for each observation. Spectra of candidate mineral locations were also divided by a spectrum from within the same CRISM data set that is spectrally neutral in order to suppress remaining instrument artifacts. Specifically, the denominator spectra were chosen from nearby regions that are spectrally flat between 1 and $2.5 \mu\text{m}$. For reference, Figure 4.4 shows the end member spectra for each of our units identified from CRISM data, along with the neutral spectra used to generate ratioed spectra. For comparison purposes, the figure also presents the ratioed versions of the spectra along with laboratory analogs discussed in a subsequent section of this paper.

Initial mineral detections were made using CRISM summary products generated with the ENVI plug-in CRISM Analysis Tool (CAT) [Pelkey *et al.*, 2007]. The spectral parameter summary products take advantage of unique absorptions or combinations of spectral features that some minerals have in the visible/near-infrared wavelengths, and are a first-order tool for identifying locations to explore in greater detail with the full wavelength range of the data set. For example, most hydrated sulfates have a spectral feature at 2.4 μm [Cloutis *et al.*, 2006], and, therefore, a mathematical expression which takes into account the overall slope of the spectrum in that wavelength region and the actual absorption at 2.4 μm can be used to identify the possible signature of sulfates in a spectrum [Pelkey *et al.*, 2007]. Multiple parameters can be used together to identify monohydrated sulfates (absorptions at both 2.1 and 2.4 μm) or polyhydrated sulfates (absorptions at 1.4, 1.9, and 2.4 μm). Initial detections of hydrated minerals within the layered deposits were made over Aram Chaos using the spectral parameters or combinations of spectral parameters indicated in Table 1. A new parameter algorithm was developed after examination of both I/F and ratioed data showed the presence in some locations of a sharp and relatively deep band at 2.2318 μm . The parameter to map the depth of this band was defined as follows:

$$BD2230 = 1 - \frac{R_{2.2318}}{\left(0.468 \times \frac{(R_{2.2120} + R_{2.1988})}{2} + 0.532 \times \frac{(R_{2.2583} + R_{2.2517})}{2}\right)}$$

where $R(\lambda)$ is the reflectivity at wavelength λ . This band depth parameter (BD2230¹) is now incorporated into the spectral summary parameters in CAT versions 6.5 and above.

¹ The parameter should be called BD2232 (the actual band is at 2.2318 micrometers), but it is called BD2230 for historical reasons.

Detections of specific minerals were confirmed by examining the wavelength range between 0.4 and 2.6 μm of the atmospherically- and photometrically-corrected hyperspectral data over each detection and comparing the spectra to laboratory-based mineral spectra resampled to CRISM band passes in the visible-NIR wavelength range. As already noted, Figure 4.4 presents I/F spectra for end members retrieved from CRISM data, along with the spectrally “neutral” spectrum used to generate ratio presentations. Also shown in this figure are ratioed data for the L-detector spectral range and laboratory spectra of likely analogs. The end member spectra were extracted from the CRISM spectra by inspection of band parameter maps and detailed examination of a large number of I/F and ratioed spectra where parameter maps indicated a relatively high abundance of a given mineral species.

The imaging and spectral data sets were used in tandem to generate maps that show the locations of mineral identifications with CRISM data, mineral identifications with OMEGA and TES data from previous work, and geologic units that contain the specific mineral signatures (Figures 4.2a and b). Gridded global topography data from MOLA (1 m vertical resolution) [Smith *et al.*, 2003] and digital elevation maps generated from stereo HRSC data (20-100 m vertical resolution) [Ansan *et al.*, 2008] were used in conjunction with the other datasets to define embayment and superposition relationships among the various units and to define the map units and stratigraphic relationships shown in Figures 4.2b and 4.3.

4.3.2 Laboratory Measurements

To support spectral identification of sulfate-bearing minerals, visible and near-infrared (VNIR), Mössbauer (MB), and powder X-ray diffraction (XRD) measurements were acquired for synthetic melanterite ($\text{FeSO}_4 \cdot 7\text{H}_2\text{O}$; Fisher Scientific) heated in air at 80, 110, 130, 150, 200, and 240°C for 2, 3, 18, 21, 21, 18 hr, respectively. An Analogue Spectral Devices FieldSpec RS³ spectrometer with a Muglight option was used to obtain VNIR spectra at room temperature. Transmission Mössbauer spectra were obtained at room temperature and with a Ranger Scientific spectrometer (Model MS-1200) using a $^{57}\text{Co}(\text{Rh})$ source and analyzed using the methods outlined by *Morris et al.* [2000]. The values of the doublet Mössbauer parameters isomer shift ($\delta = (v_1 + v_2)/2$) and quadrupole splitting ($\Delta E_Q = v_1 - v_2$) were calculated from the center positions (v_1 and v_2 with $v_2 > v_1$) of the two peaks. The value of δ is reported relative to the center position of the spectrum of metallic iron foil at room temperature. A Scintag XDS 2000 X-ray diffractometer using $\text{CuK}\alpha$ radiation and a step size of $0.02^\circ 2\theta$ was employed to obtain X-ray diffraction powder patterns ($\sim 293\text{ K}$). On the basis of XRD patterns, the powders obtained by thermal decomposition of synthetic melanterite at 80 and 240°C are synthetic szomolnokite ($\text{FeSO}_4 \cdot \text{H}_2\text{O}$) and ferric hydroxysulfate ($\text{Fe}(\text{OH})\text{SO}_4$), respectively. VNIR and MB spectra of the synthetic melanterite, szomolnokite, and ferric hydroxysulfate are shown in Figure 4.5. As will be shown in the next section of this paper, melanterite is an example of a polyhydrated phase that matches CRISM-based spectra and szomolnokite is a match for the monohydrated phase in Aram Chaos. $\text{Fe}(\text{OH})\text{SO}_4$ can be identified as a specific phase based on detailed comparison of CRISM-based and our laboratory data, as shown in Figure 4.4.

4.4 Stratigraphy and Mineralogy of Sedimentary Deposits

Two major stratigraphic units unconformably overlying the basaltic basement chaos terrain were mapped in detail as part of our work (Figures 4.2b-4.3). The chaos terrain beneath and surrounding the sedimentary deposits was described elsewhere in detail and will not be covered in this paper [Glotch and Christensen, 2005; Oosthoek *et al.*, 2007; Masse *et al.*, 2008b; Noe Dobrea *et al.*, 2008]. CRISM spectra for the chaos surfaces are consistent with the presence of nanophase ferric oxides variably mixed with basaltic materials. Descriptions for the two overlying sedimentary units incorporate both the results of this study and previous work in this area and are described in this section from oldest to youngest. As already noted, a schematic cross-section showing the current topographic relationships of the sedimentary units and basement chaos materials is shown in Figure 4.3.

4.4.1 Ferric Hydroxysulfate, Monohydrated Sulfate, and Nanophase Ferric Oxide Unit

The first of the two sedimentary units has three distinctly different stratigraphic horizons. From oldest to youngest these are monohydrated sulfates with ferric hydroxysulfate, monohydrated sulfates, and monohydrated sulfates with nanophase ferric oxides. The changing mineralogy represents a facies change and likely temporal evolution in the environments of deposition and/or alteration.

Ferric Hydroxysulfate, Monohydrated Sulfates: The sedimentary section sitting directly and unconformably on the chaos bedrock surface is spectrally dominated by monohydrated sulfate-bearing materials, but together with ferric hydroxysulfate-bearing materials exposed in a number of areas (Figures 4.2b, 4.3, and 4.4). Examination of these

exposures with HRSC DEM data shows that these deposits in total are 50 to 75 m thick. The $\text{Fe}^{+3}(\text{OH})\text{SO}_4$ -bearing material occurs in small exposures that are intercalated with deposits of monohydrated sulfate (Figure 4.6). In the CRISM observations in which this signature is detected at the edge of the sedimentary deposit (FRT8EB6 and FRT98B2), the material is found in contact with both the basement chaos blocks and monohydrated sulfate (Figure 4.6a; FRT8EB6 not shown). In the CRISM observations over the interior of the sedimentary deposit (HRL646A and FRT7FA4; Figure 4.6b), the $\text{Fe}^{+3}(\text{OH})\text{SO}_4$ signature is only detected in areas where erosion has exposed the contacts between the sedimentary material and the underlying basement chaos surfaces. Examination of HiRISE data (Figure 4.7) shows that areas with the $\text{Fe}^{+3}(\text{OH})\text{SO}_4$ signature correspond to dark material that is cracked on a several-meter scale and superimposed by the light-toned, monohydrated sulfate-bearing material. Although the $\text{Fe}^{+3}(\text{OH})\text{SO}_4$ -bearing unit occurs in only four of the targeted CRISM observations over Aram Chaos, areas with similar morphology in CTX data not covered by CRISM observations suggest that its occurrence is more extensive.

The $\text{Fe}^{+3}(\text{OH})\text{SO}_4$ interpretation above is based on a spectral absorption at 2.238 μm , coupled with minor absorptions at 1.49, 1.82, and 2.38 μm (Figure 4.4). The 2.238 μm absorption is accompanied by a distinct spectral shape just shortward of 2.24 μm . The non-detection of a band centered at 1.40 μm indicates that structural H_2O is not present at detectable levels. This material was previously mapped by both *Masse et al.* [2008b] and *Lichtenberg et al.* [2008] and interpreted to be an Al-OH bearing mineral by *Masse et al.* [2008a]. As noted previously in this paper, synthetic melanterite ($\text{Fe}^{+2}\text{SO}_4 \cdot 7\text{H}_2\text{O}$) was heated in laboratory air at $\sim 240^\circ\text{C}$ for 21 hours, resulting in

production of H₂O and H₂ by-products, Fe⁺³ from oxidation of Fe⁺², and formation of Fe⁺³(OH)SO₄. VNIR laboratory spectrum of the synthetic Fe⁺³(OH)SO₄ is shown compared to the ratioed CRISM spectrum of this material in Figure 4.4. Figure 4.5 shows the synthetic melanterite, szomolnokite (Fe⁺²SO₄·H₂O), and ferric hydroxysulfate VNIR spectra along with Mössbauer spectra confirming the transition from Fe⁺² from synthetic melanterite to Fe⁺³ as the sample was heated and converted to ferric hydroxysulfate. The VNIR spectra also show the shift of the ~1.9 μm absorption due to H₂O in the melanterite to ~2.1 μm in the szomolnokite. The spectra of the ferric hydroxysulfate in Aram Chaos are similar to the spectra of dehydrated ferricopiapite (Fe⁺³(SO₄)₆(OH)₂·20H₂O) reported by *Milliken et al.* [2008] and *Bishop et al.* [2009], although their data show neither an absorption at 1.82 μm nor the distinctive spectral structure shortward of 2.24 μm. The Aram Chaos ferric hydroxysulfate is also distinct from the ferric-bearing sulfates found at Gusev crater and Meridiani planum on the basis of Mössbauer data (Figure 4.5 and *Morris et al.*[2006a; 2006b; 2008]).

Monohydrated Sulfates: Above approximately 75 m above the contact with the underlying chaos bedrock, the sedimentary deposit transitions without any major unconformities to a monohydrated sulfate-dominated material (Figures 4.2b, 4.3, and 4.4). This material, similar to the monohydrated sulfate signatures lower in the section, is characterized by spectral absorptions at ~2.1 and 2.4 μm and is dominated by flat, layered terrains with occasional scalloped textures due to wind erosion. This material is laterally extensive throughout the sedimentary deposit, covering approximately 1200 km². Although the spectral absorptions correspond most strongly with exposures of light-toned, scalloped material (Figure 4.7) the distinctive signatures are also apparent in flat-

lying places of medium albedo (Figure 4.8). Based on examination of CTX data, these areas are most likely outcrops of the light-toned monohydrated sulfate-bearing material covered with a thin aeolian cover of basaltic sands [Glotch and Christensen, 2005]. The widespread but sporadic occurrence of this unit throughout the sedimentary deposit suggests it may be more common than indicated, but exposed by erosion only in certain places and obscured by basaltic sands in other locations. The total thickness of this monohydrated sulfate unit ranges from 75 to 100 m.

Gendrin et al. [2005] identified this material as the magnesium monohydrated sulfate kieserite ($\text{Mg}(\text{SO}_4)\cdot\text{H}_2\text{O}$) based on the lack of an Fe absorption between 0.6 and 1.0 μm . However, an absorption at $\sim 1.0 \mu\text{m}$ in the non-ratioed spectrum (Figure 4.4) suggests a possible iron-bearing sulfate such as szomolnokite, an interpretation that we prefer. The ferric hydroxysulfate that is spectrally a match to the material we see in Aram Chaos was formed by dehydration and oxidation of szomolnokite, lending credence to the presence of szomolnokite in the region.

Monohydrated Sulfates and Nanophase Ferric Oxides: The monohydrated sulfate signature transitions to a cliff-forming section that attains a thickness of between 175 and 350 m and forms a capping plateau $\sim 4600 \text{ km}^2$ in area, partially covered with basaltic sands. The exposed walls of this unit are light-toned and indurated, with erosional scars down the sides where material has undergone gravity-induced slumping and sliding (Figure 4.9). Chaos bedrock can be seen as “kipukas” standing above and surrounded by these deposits in the southwest corner of Aram Chaos (Figure 4.2), and in certain places this material has been deeply eroded to reveal the basement chaos terrain [Glotch and Christensen, 2005]. The spectral signature of the light-toned cliffs is dominated by

nanophase ferric oxides [Morris *et al.*, 2006a; 2006b; Masse *et al.*, 2008b], but minor absorptions at 2.1 and 2.4 μm indicate that the material also contains monohydrated sulfates [Masse *et al.*, 2008b].

HiRISE images covering this unit (Figure 4.9) show that the exposed walls of this deposit are finely layered, with thicknesses similar to those inferred from the middle or monohydrated sulfate portion of the deposit. In fact, in CRISM observation FRT7FA4 up to twelve distinct layers are exposed within the monohydrated sulfate (middle) unit, forming a stair step pattern with some of the layers traceable to beneath the cliff-forming deposits.

4.4.2 Polyhydrated Sulfates, Hydrated Materials, and Hematite Deposits

This second sedimentary unit is 75-100 m thick and is characterized by an absorption at 1.9 μm indicating the presence of one or more polyhydrated minerals and a plateau-like morphology. Compared to the monohydrated sulfates, the polyhydrated materials are darker and smoother and appear more indurated and resistant to weathering than the monohydrated deposits. Previous work in Aram Chaos with OMEGA data has shown that one of the hydrated minerals is most likely a polyhydrated sulfate based on an additional absorption at 2.4 μm [Gendrin *et al.*, 2005; Noe Dobrea *et al.*, 2008].

Examination of the locations where the 1.9 μm band depth is present in CRISM data over the plateau (Figure 4.10) shows that polyhydrated minerals are present, but that their locations are not ubiquitous throughout the region as mapped by OMEGA (Figure 4.2a).

This unit also coincides spatially with the detection of crystalline hematite (Fe_2O_3), identified from Thermal Emission Spectrometer data [Christensen *et al.*, 2001;

Glotch and Christensen, 2005; Noe Dobrea et al., 2008]. Using OMEGA data *Masse et al.* [2008b] showed that goethite ($\text{Fe}^{+3}\text{O}(\text{OH})$), ferrihydrite ($\text{Fe}_2^{+3}\text{O}_3 \cdot 0.5\text{H}_2\text{O}$), or schwertmannite ($\text{Fe}_8^{+3}\text{O}_8(\text{SO}_4)(\text{OH})_6$) may also be present in this unit along with hematite. These ferric oxides are not expected to be stable under present day Martian conditions; *Masse et al.* [2008b] suggest that their continued existence can be explained by very slow transformation kinetics. The strongest ferric-oxide and enhanced-hydration detections occur on the slightly raised plateau in the northeast part of the deposit (Figures 4.2a and b), although hematite is detected in lower concentrations at slightly lower elevations due to erosion and transport onto lower-lying regions [*Glotch and Christensen, 2005*].

In contrast to previous work, the analysis of high resolution MRO data shows that this unit is unconformably superimposed on the monohydrated-sulfate-bearing sedimentary section described in the previous section of this paper. We see no evidence for polyhydrated signatures in these older deposits and we see no morphologic evidence that the polyhydrated deposits are beneath or included in the older deposits. For example, CRISM observations that cover parts of the older cliff-forming deposits (FRTC14E, FRTBE2D, and FRT7FA4) do not show spectral indications of polyhydrated sulfates in the wall exposures (Figure 4.9). In addition, examination of the cliff walls in CTX and HiRISE images show no indications of a low-albedo layer which might indicate the presence of polyhydrated/hematite/iron oxide material 4 (Figure 4.11). Thus, even though this material is topographically below the cliff-forming unit (monohydrated sulfates and nanophase ferric oxides), we conclude the monohydrated-sulfate-bearing unit was already emplaced and differentially eroded by the time the polyhydrated deposits

formed. This inference is also consistent with mapping the spatial distribution of these materials using OMEGA data, morphology, and albedo [*Gendrin et al.*, 2005; *Noe Dobrea et al.*, 2008]. We infer that the polyhydrated deposits formed in local topographic lows after formation and differential erosion of the older, monohydrated-sulfate-bearing sedimentary unit.

4.5 Summary and Implications

Our work shows that the sedimentary deposits in Aram Chaos first formed with intercalated ferric hydroxysulfate ($\text{Fe}^{+3}(\text{OH})\text{SO}_4$) and monohydrated sulfates (likely, szomolnokite) at the base of the section, followed by monohydrated sulfates, followed by a mix of monohydrated sulfates and nanophase ferric oxides. The data show that these deposits were then differentially eroded by wind, after which polyhydrated materials (e.g. polyhydrated sulfates) with hematite and other ferric oxides were deposited in low lying areas during a second depositional event. Work by *Wang and Freeman* [2009] shows that relative humidity is a critical factor in determining hydration/dehydration states of forming Mg-sulfates. In conjunction with their work, our work indicates a possible change in environmental humidity between depositional events in Aram Chaos, beginning with the formation of ferric hydroxysulfate and monohydrated sulfate under relatively dry conditions and ending with the formation of polyhydrated materials under relatively wet conditions.

We favor a formation mechanism involving groundwater recharge/evaporation and multiple wetting events to explain the stratigraphic section observed in the sedimentary deposits in Aram Chaos. Regional-scale groundwater distribution modeling

by *Andrews-Hanna et al.* [2007] predicts Aram Chaos to have one of the thickest evaporite deposits in the region. A regional-scale groundwater system would link the deposits in Aram Chaos to those in Meridiani Planum to the east and Valles Marineris to the west, so evaporite deposits in these regions should show similarities to the deposits in Aram Chaos. Analysis of sulfate deposits in Meridiani [*Wiseman et al.*, 2009] show that mono and polyhydrated sulfate species in the northern valley are likely separated from the main Meridiani sequence by erosion, indicating a pause between depositional events in this area too. The sequence of polyhydrated sulfates overlying monohydrated sulfates is mimicked to the west in Candor Chasma, where *Murchie et al.* [2009] found that polyhydrated materials in Candor Chasma are younger than the monohydrated sulfates and occupy topographic lows. Both the sequence of polyhydrated materials overlying intercalated ferric hydroxysulfate and monohydrated sulfates and the unconformable contact between them signifying a period of erosion between depositional events in multiple locations throughout this region indicate that a plausible formation method is a series of groundwater upwelling events fed by groundwater recharge, as modeled by *Andrews-Hanna et al.* [2007].

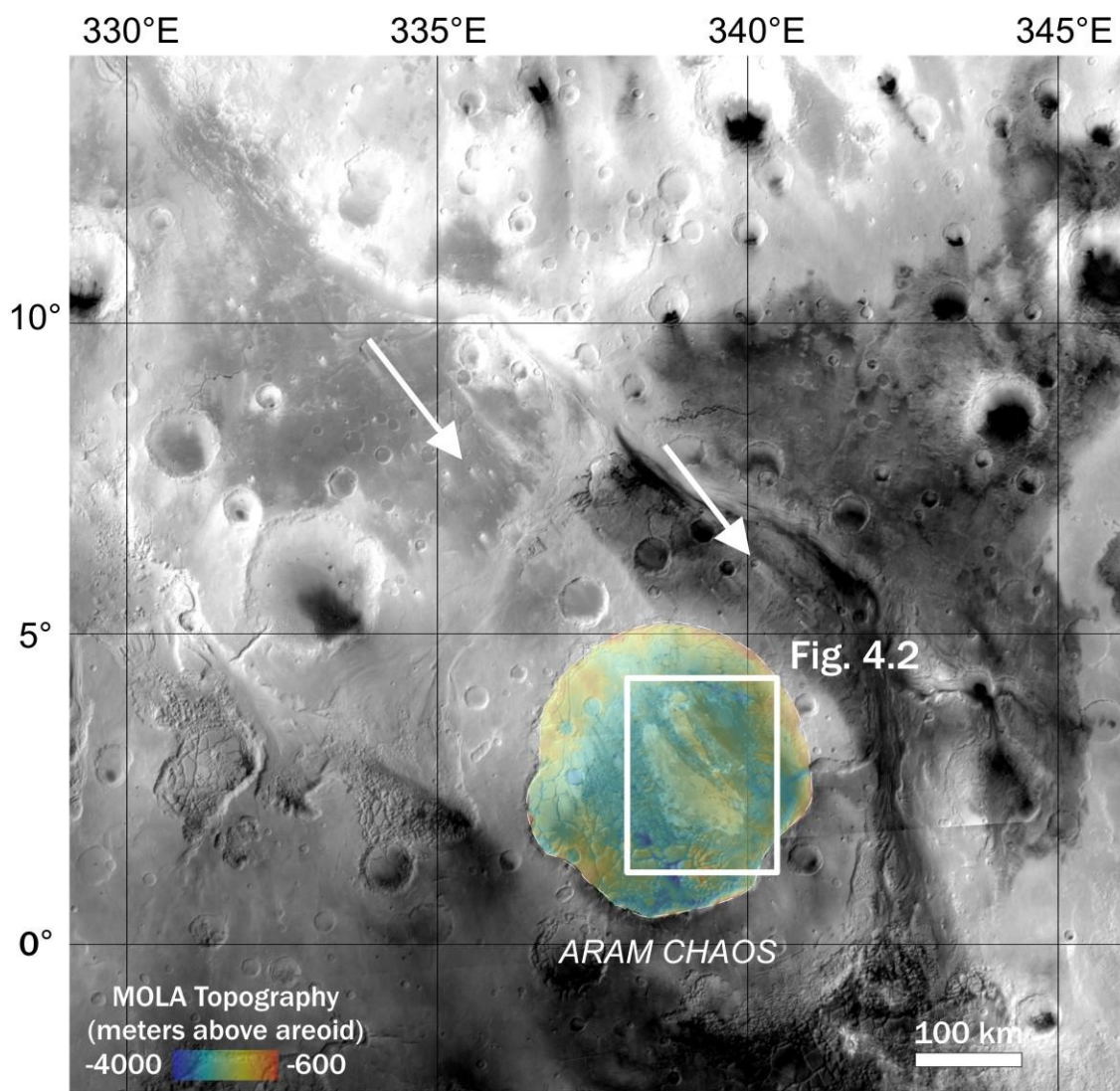


Figure 4.1. MOC-based mosaic of northern Xanthe Terra (231.55 m/pixel). White arrows indicate small craters with wind streaks trending to the southeast, showing the dominant wind direction in this area. The sedimentary unit within Aram Chaos is located in the white box; this is also the area shown in Figure 4.2. Other chaos regions can be seen to the west and south of Aram Chaos.

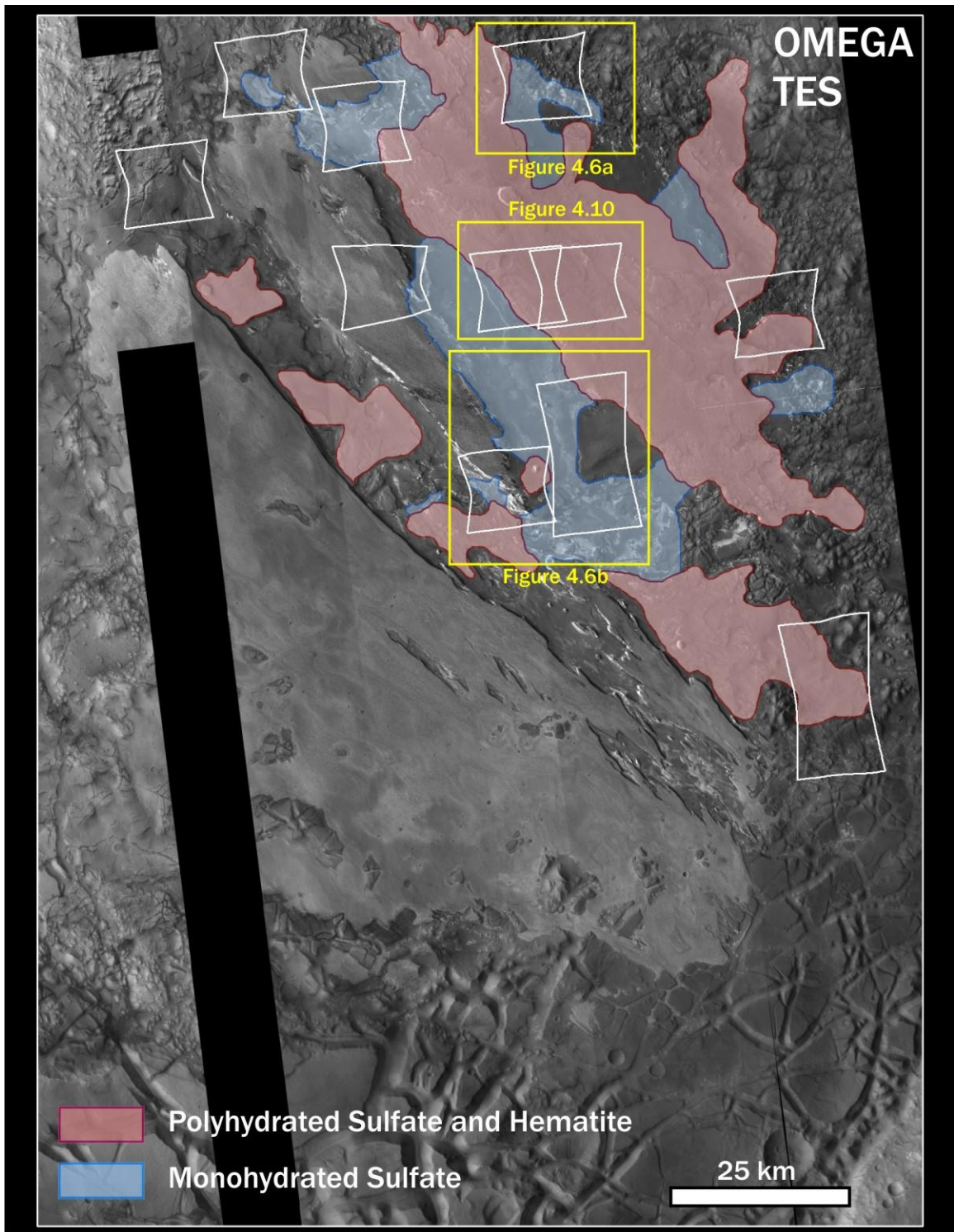


Figure 4.2a. The extent of the layered sedimentary deposits in Aram Chaos is illustrated in this CTX-based mosaic. Locations of OMEGA- and morphologically-identified extents of mono- and polyhydrated sulfates. CRISM targeted observations are indicated with white outlines; locations of Figures 4.6a, 4.6b, and 4.10 are indicated with yellow boxes.

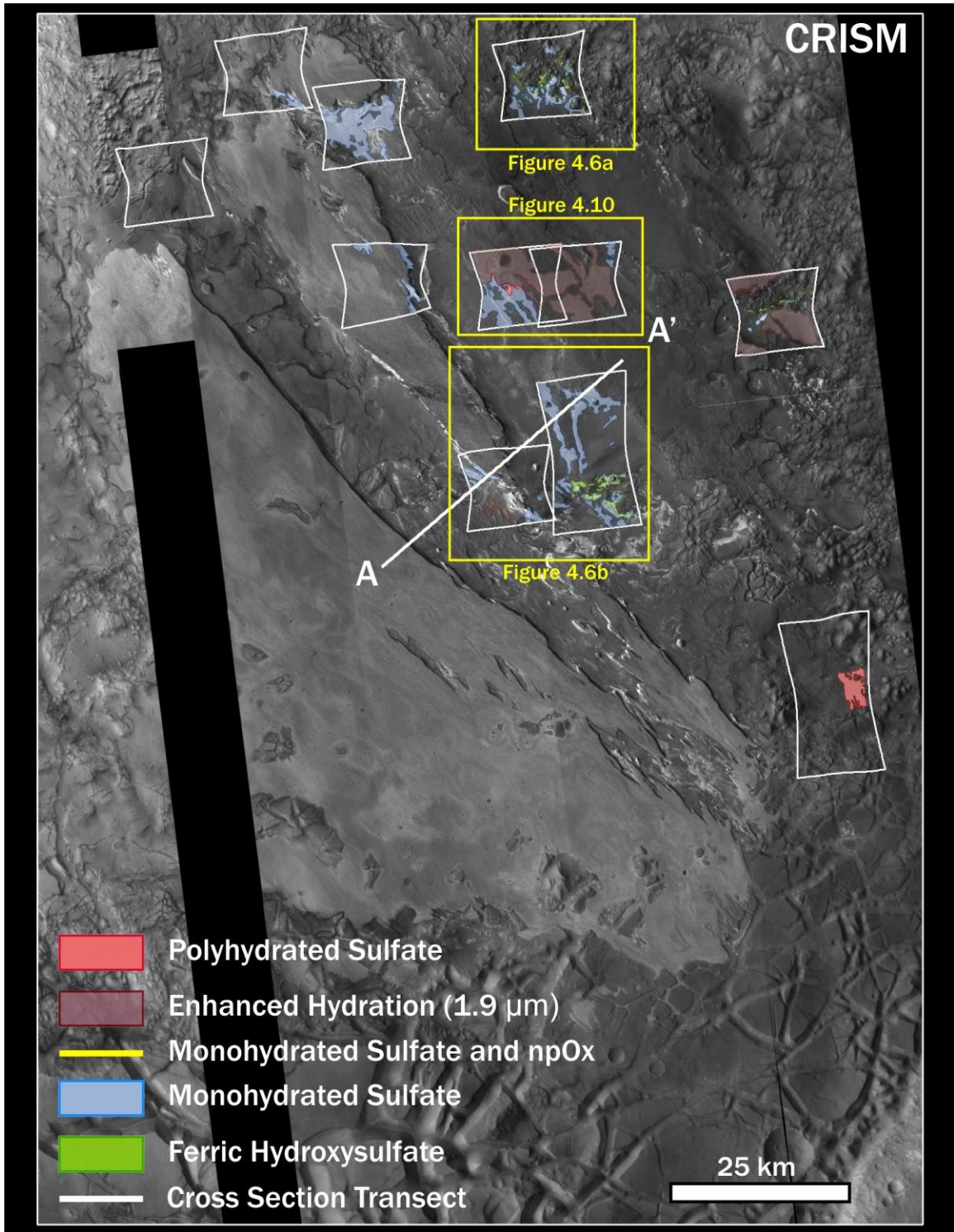


Figure 4.2b. The extent of the layered sedimentary deposits in Aram Chaos is illustrated in this CTX-based mosaic. Same area as 4.2a, but with CRISM-based mineral detections. Key is as follows: 1.9 and 2.4 μm absorptions indicative of polyhydrated sulfates (red); 1.9 μm absorption indicating enhanced hydration but without a corresponding 2.4 μm absorption indicating hydrated sulfate (light red); 2.1 and 2.4 μm absorptions indicative of monohydrated sulfates (blue); 2.23 μm absorption indicative of ferric hydroxysulfates (green). The cross-section in Figure 4.3 is indicated by the white line (A to A').

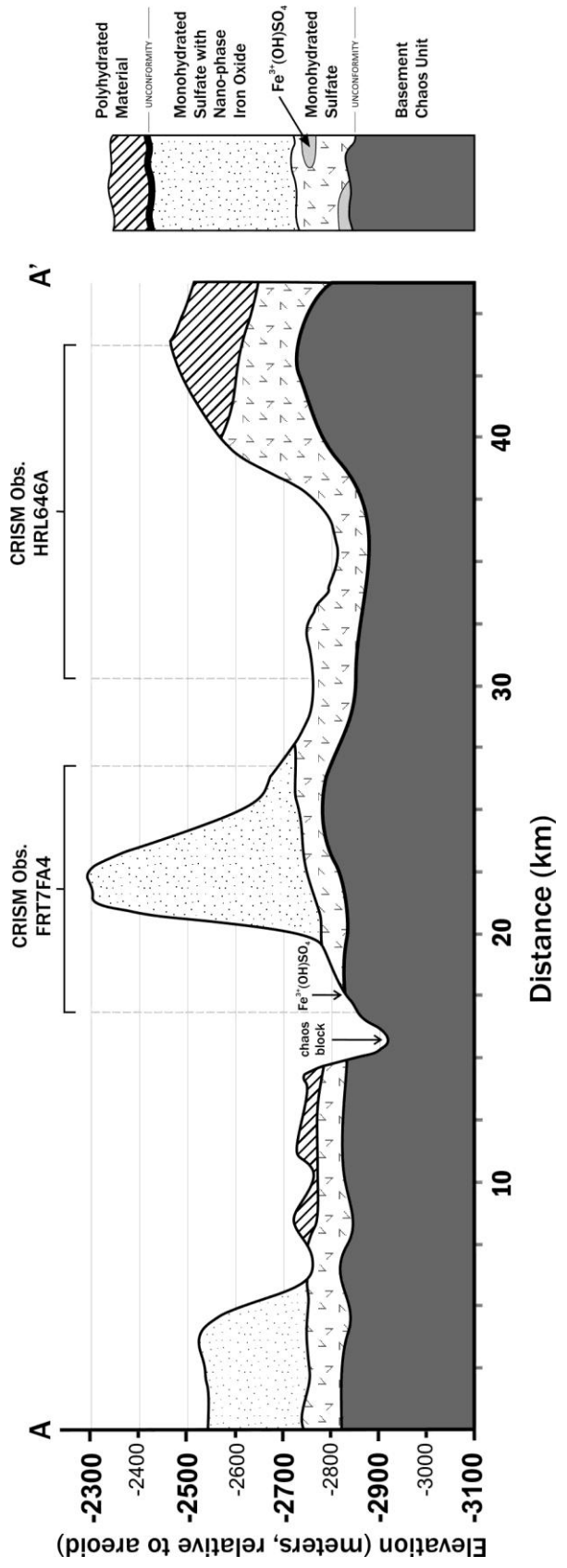


Figure 4.3. Schematic cross-section derived from mineralogic, morphologic, and topographic data and covering all described units of the sedimentary deposit. MOLA elevations are in meters below reference areoid. The monohydrated sulfate and ferric hydroxysulfate are shown in the stratigraphic column as discrete deposits, but the contact between them is likely gradational. On the other hand, the boundary with the polyhydrated material is an unconformity separated by a period of erosion.

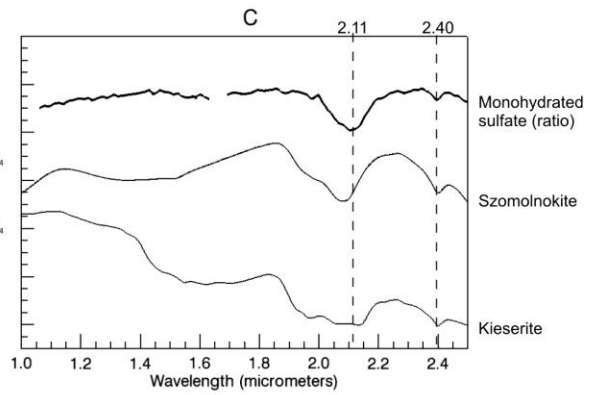
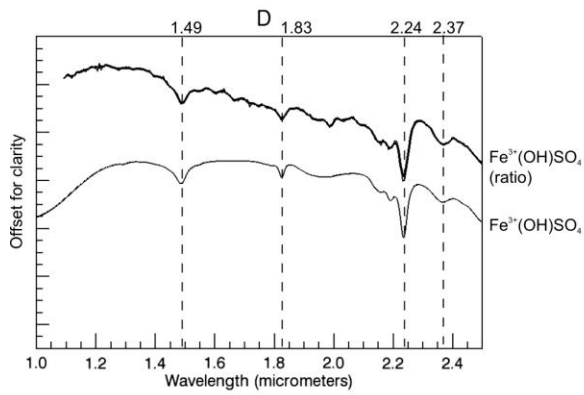
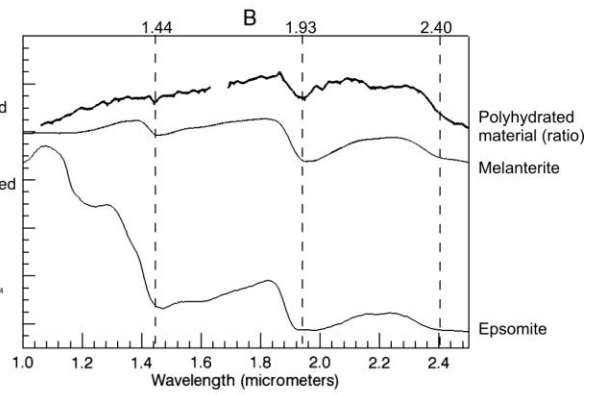
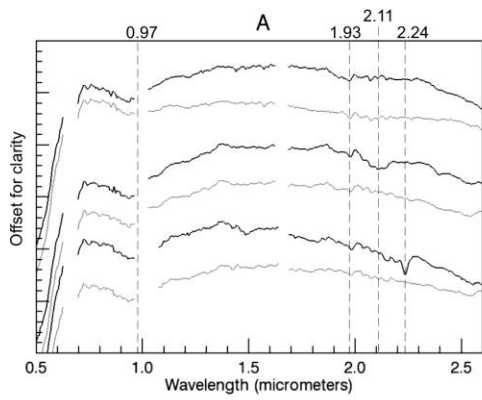


Figure 4.4. Spectral reflectance characteristics of the sedimentary deposits. Wavelengths shorter than 1.0 μm are not shown for the ratioed spectra since there are no neutral spectra in this wavelength region. Spectra in A are offset; spectra in B, C, and D are scaled and offset for clarity. Numbers above the plots are in micrometers and indicate indentifying absorptions. Clockwise from top left: (A) atmospherically- and photometrically-corrected numerator and denominator spectral pairs for the ferric hydroxysulfate, monohydrated sulfate, and polyhydrated sulfate; numerators are shown in black and denominators are shown in gray from 0.5 to 2.5 μm . Data not shown at around 1.0 μm (detector boundary) and 1.65 μm (known instrument artifact). (B) Polyhydrated sulfate ratioed spectrum (numerator/denominator) and lab spectra for candidate minerals melanterite $[\text{Fe}(\text{SO}_4)\cdot 7\text{H}_2\text{O}]$ and epsomite $[\text{Mg}(\text{SO}_4)\cdot 7\text{H}_2\text{O}]$. (C) Monohydrated sulfate ratioed spectrum and candidate minerals szomolnokite $[\text{Fe}^{+2}(\text{SO}_4)\cdot \text{H}_2\text{O}]$ and kieserite $[\text{Mg}(\text{SO}_4)\cdot \text{H}_2\text{O}]$. The kieserite spectrum presented here may have water contamination as evidenced by the absorption at $\sim 1.9 \mu\text{m}$. (D) Ferric hydroxysulfate ratioed spectrum and laboratory-created ferric hydroxysulfate $[\text{Fe}(\text{SO}_4)\text{OH}]$; the CRISM band with the minimum around 2.24 μm is at 2.238 μm , which is the closest CRISM band to 2.4 μm . The melanterite, szomolnokite, and ferric hydroxysulfate spectra are from laboratory experiments presented in the text and are also shown in Figure 4.5; the epsomite and kieserite spectra are from the CRISM spectral library.

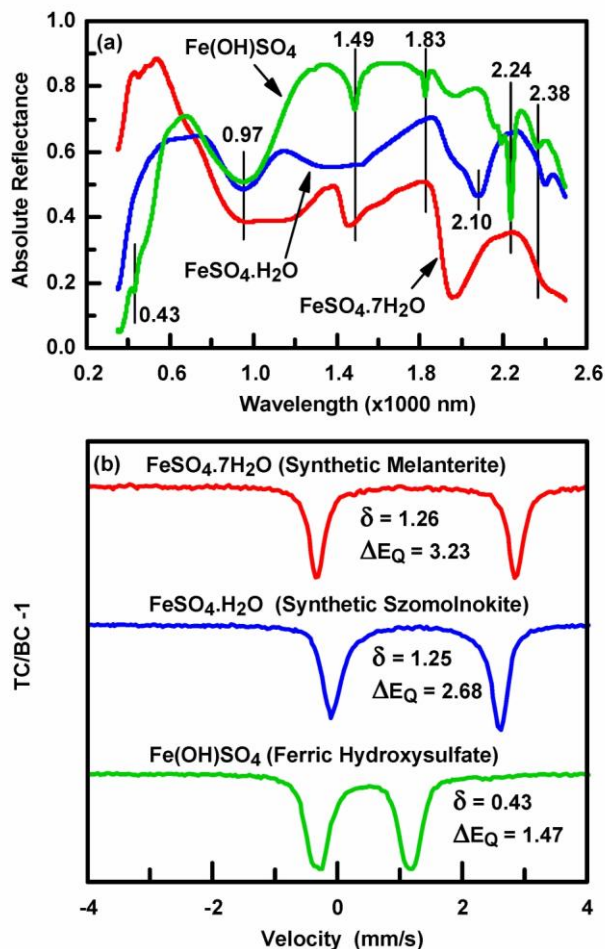


Figure 4.5. (a) VNIR and (b) Mössbauer spectra at room temperature for synthetic melanterite [FeSO₄·7H₂O], szomolnokite [FeSO₄·H₂O], and ferric hydroxysulfate [Fe(OH)SO₄] were obtained by thermal decomposition of FeSO₄·7H₂O in air at 80 and 240°C, respectively. For Fe(OH)SO₄ in (a), the spectral features at 1.49, 1.83, 2.24, 2.38 μm are associated with Fe³⁺-OH vibrations, and the spectral features at 0.43 and 0.97 μm are associated with Fe³⁺ electronic transitions. The Mössbauer parameters (δ and ΔE_Q) in (b) are characteristic of octahedrally-coordinated Fe²⁺ (FeSO₄·7H₂O and FeSO₄·H₂O) and octahedrally-coordinated Fe³⁺ (Fe(OH)SO₄)

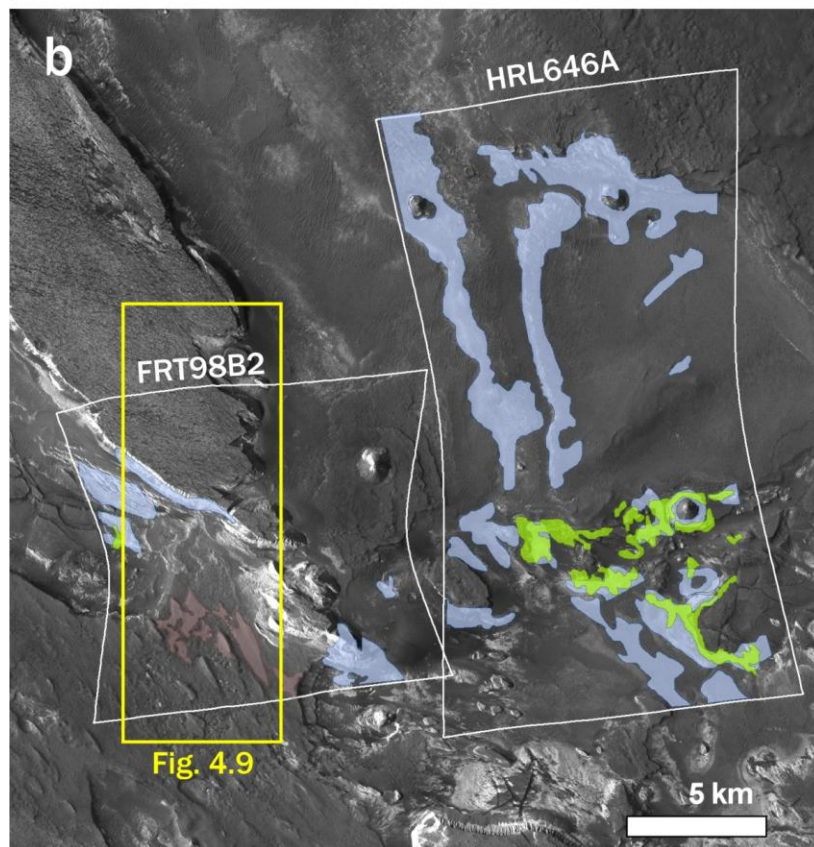
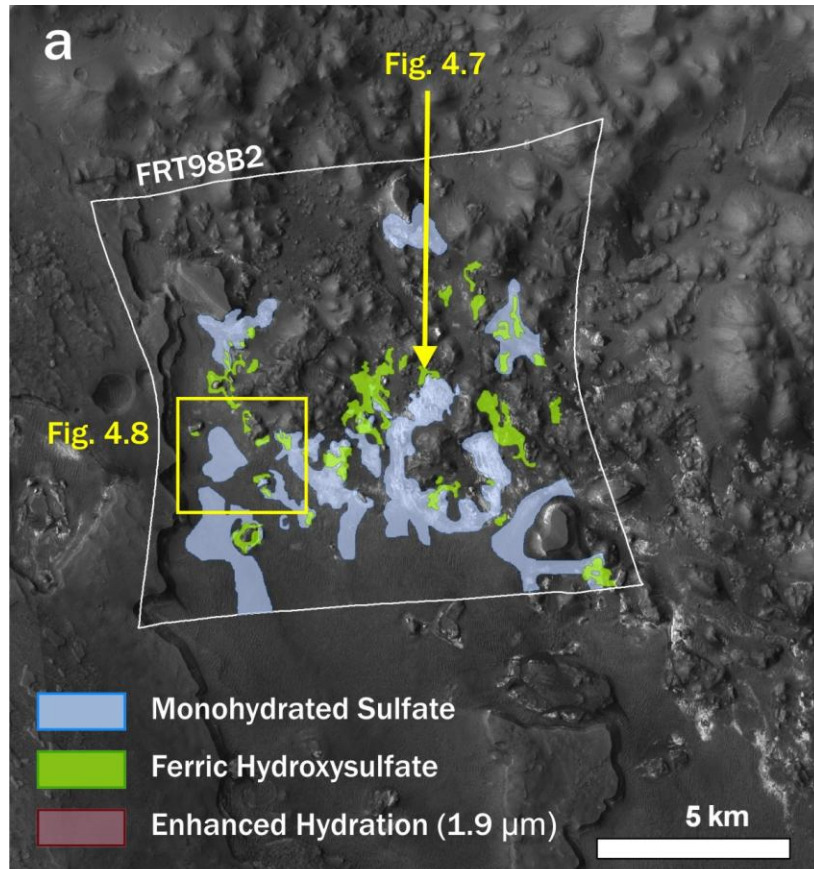


Figure 4.6. Locations of monohydrated sulfate (indicated by absorptions at 2.1 and 2.4 μm , shown in blue) and ferric hydroxysulfate (indicated by an absorption at 2.238 μm , shown in green) in three CRISM targeted observations. The location of Figure 4.7 is indicated by the yellow arrow. The locations of the HiRISE close-ups in Figures 4.8 and 4.9 are indicated with yellow boxes. (a) Monohydrated sulfate and ferric hydroxysulfate at the edge of the depositional unit, (b) monohydrated sulfate and ferric hydroxysulfate in the interior of the sedimentary deposits where the deposits have been significantly eroded, exposing blocks of the chaos bedrock.

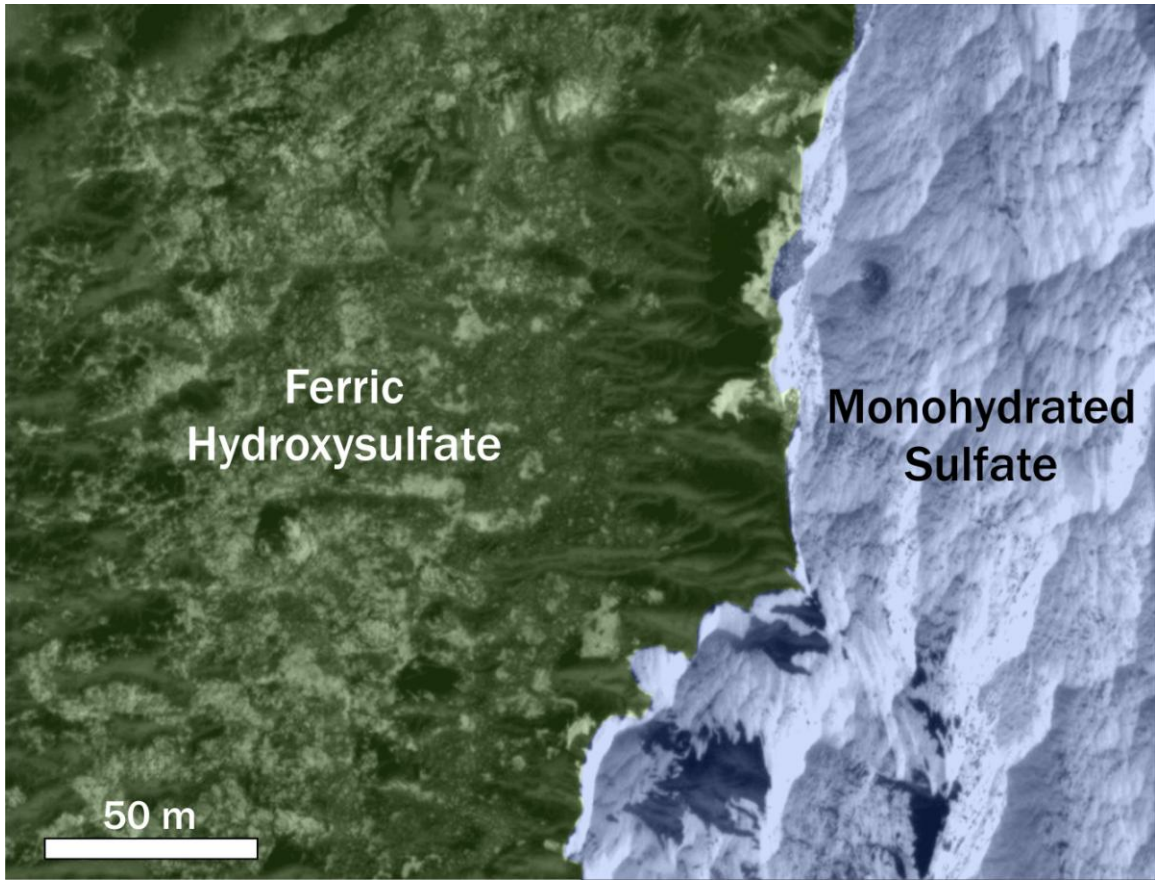


Figure 4.7. Subset of HiRISE image PSP_006953_1840 showing the contact between material exhibiting the monohydrated sulfates (light-toned scalloped area, right) and material showing absorptions indicative of the ferric hydroxysulfate (dark material, left).

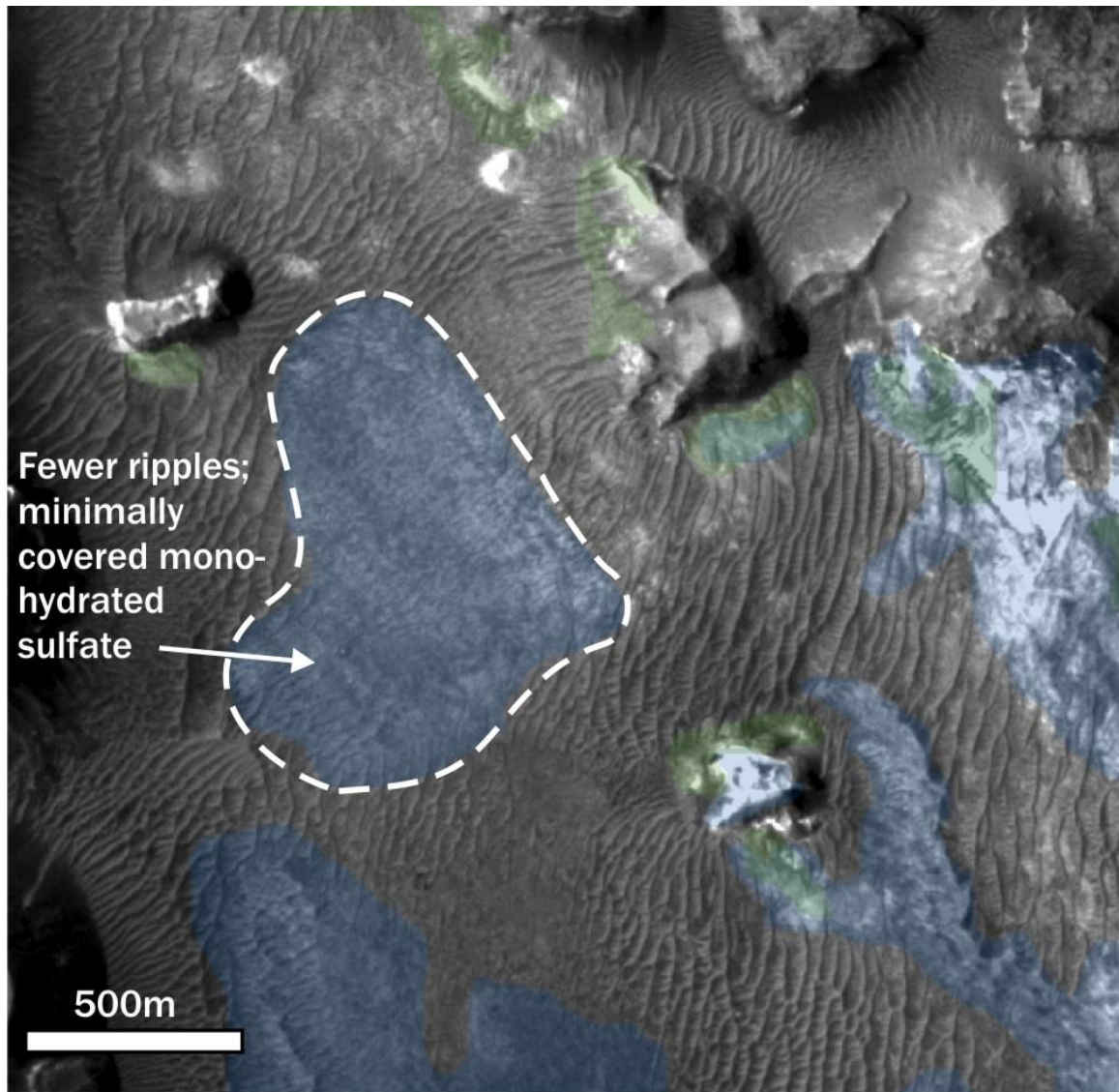


Figure 4.8. CTX mosaic over an area with strong 2.1 and 2.4 μm absorptions indicative of monohydrated sulfate. Blue shaded areas indicate the presence of monohydrated sulfate; green shaded areas indicate the presence of the ferric hydroxysulfate. Although most of the material that exhibits strong monohydrated sulfate signatures has a high albedo (Figure 4.7), the area enclosed by the dashed line does not, although some brighter material can be seen at the right edge. We interpret this to be an exposure of the monohydrated-sulfate-bearing material in Figure 4.7 that is minimally covered with wind-blown sands.

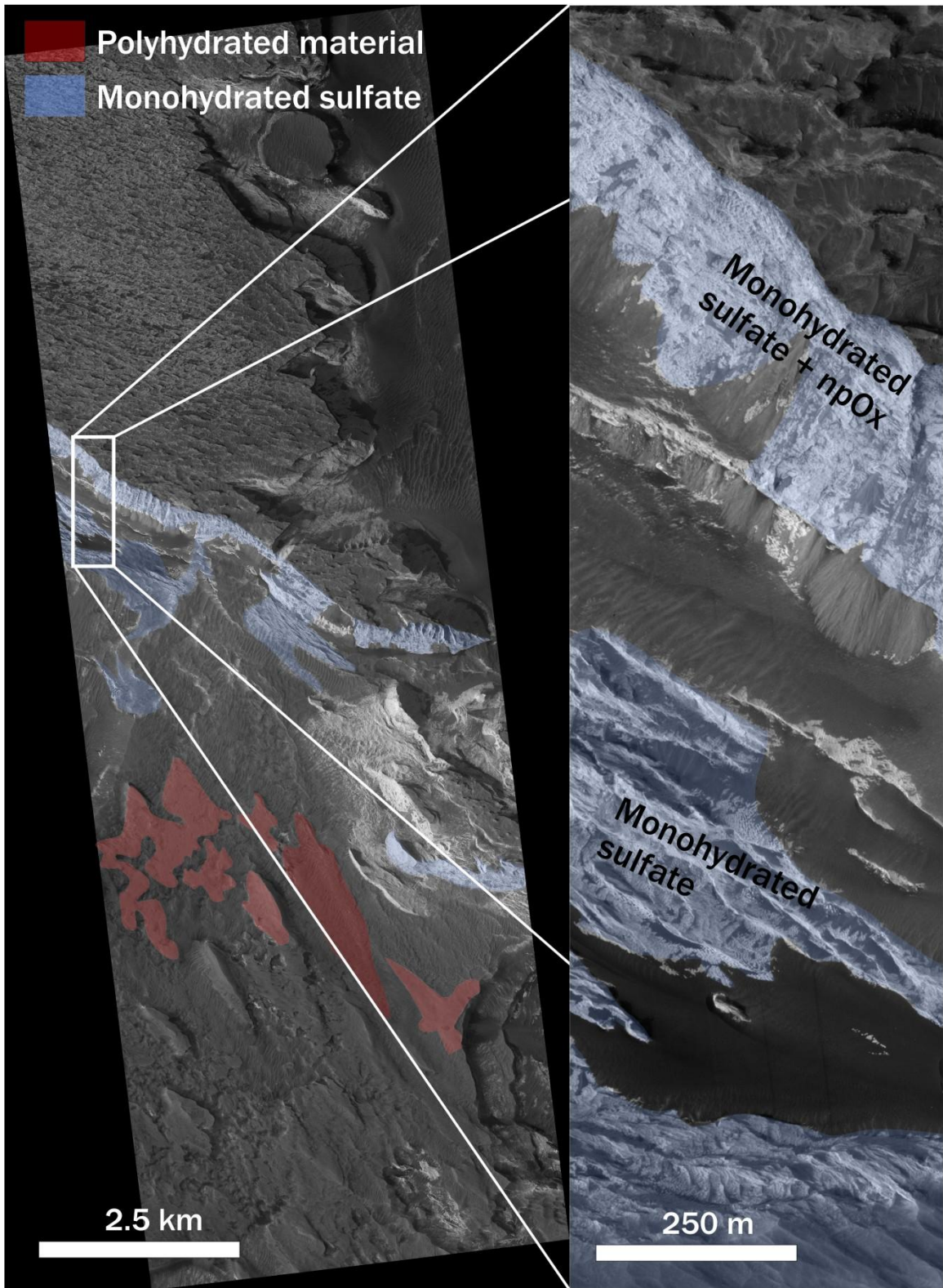


Figure 4.9. HiRISE image PSP_003406. The spectral signature of the walls is dominated by nanophase ferric oxides, but also has faint absorptions at 2.1 and 2.4 μm indicating the presence of monohydrated sulfates. Locations of strong 2.1 and 2.4 absorptions (indicating the material is dominated by monohydrated sulfates) are shown here just below the cliff. The layered nature of both the monohydrated sulfate + npOx material and the monohydrated sulfate material is visible in the blow-up on the right. The outcrop of ferric hydroxysulfate in this area is not covered in this HiRISE observation.

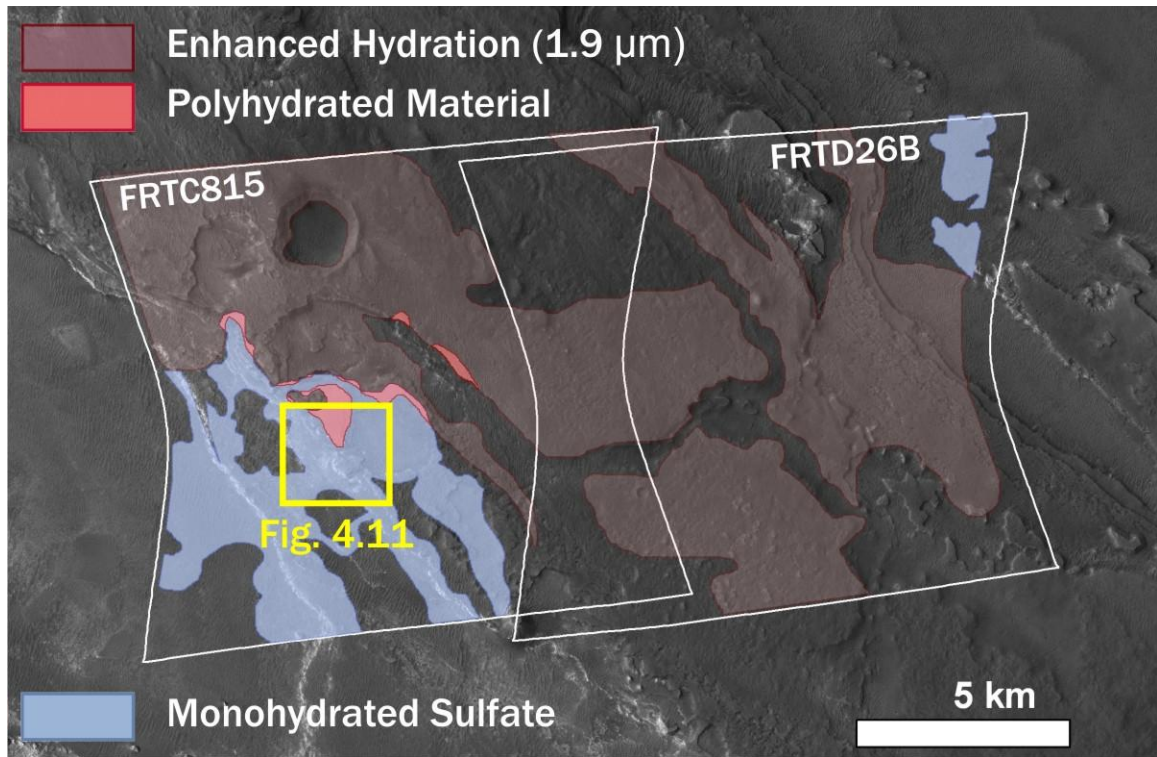


Figure 4.10. Detections of monohydrated sulfate, polyhydrated material, and enhanced hydration in CRISM observations FRTC815 and FRTD26B showing the transition from the monohydrated state at the base to a polyhydrated state in the upper section. The location of Figure 4.11 is indicated by a yellow box.



Figure 4.11. Subset of HiRISE image PSP_010025_1835 (center is at 3.39°N, 339.42°E). The monohydrated sulfate-bearing material is in layers at the base of the polyhydrated/hematite/ferric oxide unit. Aeolian ripples lying on top of the monohydrated material show an absorption at 1.9 μm , suggesting that it is material that has been eroded off the polyhydrated/hematite/ferric oxide unit. The ripples visible at the bottom of the image are trending SW-NE and are indicative of winds blowing predominantly from the northwest.

Tables

Table 4.1 Summary parameter mineral indicators.

Material	Primary indicators (μm)	Secondary indicators (μm)
Monohydrated sulfate	2.1 + 2.4	
Polyhydrated mineral	1.9	1.4
Polyhydrated sulfate	1.9 + 2.4	1.4
Ferric hydroxysulfate	2.238 (2.24)	1.48, 1.82, 2.38

Table 4.2 CRISM targeted observations used in this paper, listed in chronologic order.

Observation ID	Type	Day of Year	Center Lat/Lon	Ls
HRL0000646A	Half resolution long	2007_169	2.99N, 339.62E	259.9
FRT00007FA4	Full resolution targeted	2007_274	2.91N, 339.42E	323.3
HRL000087E6	Half resolution long	2007_302	2.40N, 340.21E	338.5
FRT00008EB6	Full resolution targeted	2007_357	3.34N, 340.08E	6.8
FRT00009496	Full resolution targeted	2008_008	3.92N, 338.82E	14.8
FRT000098B2	Full resolution targeted	2008_020	3.92N, 339.50E	20.1
FRT0000AB75	Full resolution targeted	2008_126	3.66N, 338.58E	67.6
FRT0000C14E	Full resolution targeted	2008_231	3.41N, 339.12E	114.6
FRT0000C815	Full resolution targeted	2008_259	3.41E, 339.44E	127.6
FRT0000D26B	Full resolution targeted	2008_303	3.41N, 339.59E	149.4

Table 4.3 Unit characteristics.

Compositional Information	Extent of coverage with CRISM data	Extent of coverage with OMEGA data
polyhydrated sulfate ^a ; crystalline hematite ^b ; enhanced hydration; ferric oxides	170 km ²	2770 km ²
nanophase ferric oxides; monohydrated sulfate ^a	--	4600 km ²
monohydrated sulfate ^a	200 km ²	1185 km ²
ferric hydroxysulfate monohydrated sulfate ^a	18 km ²	--

^aalso detected with OMEGA data

^bdetected with TES data (Christensen et al. 2001; Glotch and Christensen 2005)

References

- Andrews-Hanna, J.C., R.J. Phillips, and M.T. Zuber (2007), Meridiani Planum and the global hydrology of Mars, *Nature*, *446*, 163-166, doi:10.1038/nature05594.
- Ansan, V., N. Mangold, P. Masson, and G. Neukum (2008), The Topography of Valley Networks on Mars: Comparison Between Valleys of Different Ages, *Lunar and Planetary Science XXXIX*, Houston, TX.
- Arvidson, R.E., F. Poulet, R.V. Morris, J.-P. Bibring, J.F. Bell III, S.W. Squyres, P.R. Christensen, G. Bellucci, B. Gondet, B.L. Ehlmann, W.H. Farrand, R.L. Fergason, M. Golombek, J.L. Griffes, J.P. Grotzinger, E. Guinness, K.E. Herkenhoff, J.R. Johnson, G. Klingelhofer, Y. Langevin, D.W. Ming, K. Seelos, R.J. Sullivan, J.G. Ward, S.M. Wiseman, and M. Wolff (2006), Nature and origin of the hematite-bearing plains of Terra Meridiani based on analyses of orbital and Mars Exploration rover data sets, *J. Geophys. Res.*, *111*, E12S08, doi:10.1029/2006JE002728.
- Bishop, J.L., M. Parente, C. Weitz, E.Z. Noe Dobrea, L.H. Roach, S.L. Murchie, P. McGuire, N.K. McKeown, C.M. Rossi, A.J. Brown, W.M. Calvin, R.E. Milliken, and J.F. Mustard (2009), Mineralogy of Juventae Chasma: Sulfates in the Light-toned Mounds, Mafic Minerals in the Bedrock, and Hydrated Silica and Hydroxylated Ferric Sulfate on the Plateau, *J. Geophys. Res.*, *In Press*.
- Carr, M.H. (1979), Formation of Martian Flood Features by Release of Water from Confined Aquifers, *J. Geophys. Res.*, *84*, B6, 2995-3007.

- Christensen, P.R., R.V. Morris, M.D. Lane, J.L. Bandfield, and M.C. Malin (2001), Global mapping of Martian hematite mineral deposits: Remnants of water-driven processes on early Mars, *J. Geophys. Res.*, *106*, E10, 23873-23885, doi:10.1029/2000JE001415.
- Cloutis, E.A., F.C. Hawthorne, S.A. Mertzman, K. Krenn, M.A. Craig, D. Marcino, M. Methot, J. Strong, J.F. Mustard, D.L. Blaney, J.F. Bell III, and F. Vilas (2006), Detection and discrimination of sulfate minerals using reflectance spectroscopy, *Icarus*, *184*, 121-157, doi:10.1016/j.icarus.2006.04.003.
- Fenton, L.K., and M.I. Richardson (2001), Martian surface winds: Insensitivity to orbital changes and implications for aeolian processes, *J. Geophys. Res.*, *106*, E12, 32,885-32,902.
- Gendrin, A., N. Mangold, J.-P. Bibring, Y. Langevin, B. Gondet, F. Poulet, G. Bonello, C. Quantin, J.F. Mustard, R.E. Arvidson, and S. Le Mouelic (2005), Sulfate in Martian Layered Terrains: The OMEGA/Mars Express View, *Science*, *307*, 1587-1591, doi: 10.1126/science.1109087.
- Glotch, T.D., and P.R. Christensen (2005), Geologic and mineralogic mapping of Aram Chaos: Evidence for a water-rich history, *J. Geophys. Res.*, *110*, E09006, doi:10.1029/2004JE002389.
- Glotch, T.D., and A.D. Rogers (2007), Evidence for aqueous deposition of hematite- and sulfate-rich light-toned layered deposits in Aureum and Iani Chaos, Mars, *J. Geophys. Res.*, *112*, E06001, doi:10.1029/2006JE002863.
- Grotzinger, J.P., R.E. Arvidson, J.F. Bell III, W.M. Calvin, B.C. Clark, D.A. Fike, M. Golombek, R. Greeley, A. Haldemann, K.E. Herkenhoff, B.L. Jolliff, A.H. Knoll,

- M.C. Malin, S.M. McLennan, T. Parker, L.A. Soderblom, J.N. Sohl-Dickstein, S.W. Squyres, N.J. Tosca, and W.A. Watters (2005), Stratigraphy and sedimentology of a dry to wet eolian depositional system, Burns formation, Meridiani Planum, Mars, *EPSL*, 240, 11-72, doi:10.1016/j.epsl.2005.09.039.
- Langevin, Y., F. Poulet, J.-P. Bibring, and B. Gondet (2005), Sulfates in the north polar region of Mars detected by OMEGA/Mars Express, *Science*, 307, 1584-1586, doi:10.1126/science.1109091.
- Lichtenberg, K.A., R.E. Arvidson, J.L. Bishop, T.D. Glotch, E.Z. Noe Dobrea, S.L. Murchie, J.F. Mustard, L.H. Roach, and T.C. Team (2008), Mg- and Fe-Sulfate Layers in Aram Chaos, Mars, *American Geophysical Union, Fall Meeting 2008*, San Francisco, CA, Abstract # P44A-09.
- Lichtenberg, K.A., R.E. Arvidson, F. Poulet, R.V. Morris, A. Knudson, J.F. Bell III, G. Bellucci, J.-P. Bibring, W.H. Farrand, J.R. Johnson, D.W. Ming, P.C. Pinet, A.D. Rogers, and S.W. Squyres (2007), Coordinated analyses of orbital and Spirit Rover data to characterize surface materials on the cratered plains of Gusev Crater, Mars, *J. Geophys. Res.*, 112, E12S90, doi:10.1029/2006JE002850.
- Malin, M.C., J.F. Bell III, B.A. Cantor, M.A. Caplinger, W.M. Calvin, R.T. Clancy, K.S. Edgett, L. Edwards, R.M. Haberle, P.B. James, S.W. Lee, M.A. Ravine, P.C. Thomas, and M. Wolff (2007), Context Camera Investigation on board the Mars Reconnaissance Orbiter, *J. Geophys. Res.*, 112, E05S04, doi:10.1029/2006JE002808.
- Masse, M., O. Bourgeois, S. Le Mouelic, L. Le Deit, C. Verpoorter, J.P. Combe, C. Sotin, J.-P. Bibring, B. Gondet, Y. Langevin, and The OMEGA Team (2008a),

Sulfates, Ferric Oxides, and Al-OH Bearing Minerals in Aram Chaos:
Comparison of OMEGA and CRISM data, *Martian Phyllosilicates: Recorders of
Aqueous Processes*, Paris, France, Abstract # 7002.

Masse, M., S. Le Mouelic, O. Bourgeois, J.P. Combe, L. Le Deit, C. Sotin, J.-P. Bibring,
B. Gondet, and Y. Langevin (2008b), Mineralogical composition, structure,
morphology, and geological history of Aram Chaos crater fill on Mars derived
from OMEGA Mars Express data, *J. Geophys. Res.*, *113*, E12006,
doi:10.1029/2008JE003131.

McEwan, A.S., E.M. Eliason, J.W. Bergstrom, N.T. Bridges, C.J. Hansen, W.A.
Delamere, J.A. Grant, V.C. Gulick, K.E. Herkenhoff, L. Kreszhelyi, R.L. Kirk,
M.T. Mellon, S.W. Squyres, N. Thomas, and C. Weitz (2007), Mars
Reconnaissance Orbiter's High Resolution Imaging Science Experiment, *J.
Geophys. Res.*, *112*, E05S02.

Milliken, R.E., G.A. Swayze, R.E. Arvidson, J.L. Bishop, R.N. Clark, B.L. Ehlmann,
R.O. Green, J.P. Grotzinger, R.V. Morris, S.L. Murchie, J.F. Mustard, and C.
Weitz (2008), Opaline silica in young deposits on Mars, *Geology*, *36*, *11*, 847-
850, doi: 10.1130/G24967A.1.

Morris, R.V., D.C. Golden, J.F. Bell III, T.D. Shelfer, A.C. Scheinost, N.W. Hinman, G.
Furniss, S.A. Mertzman, J.L. Bishop, D.W. Ming, C.C. Allen, and D.T. Britt
(2000), Mineralogy, composition, and alteration of Mars Pathfinder rocks and
soils: Evidence from multispectral, elemental, and magnetic data on terrestrial
analogue, SNC meteorite, and Pathfinder samples, *J. Geophys. Res.*, *105*, 1757-
1817.

Morris, R.V., G. Klingelhofer, C. Schroder, I. Fleischer, D.W. Ming, A. Yen, R. Gellert, R.E. Arvidson, D.S. Rodionov, L. Crumpler, B.C. Clark, B.A. Cohen, T.J. McCoy, D.W. Mittlefehldt, M.E. Schmidt, P.A. deSouza, and S.W. Squyres (2008), Iron mineralogy and aqueous alteration from Husband Hill through Home Plate at Gusev Crater, Mars: Results from the Mössbauer instrument on the Spirit Mars Exploration Rover, *J. Geophys. Res.*, *112*, E12S42, doi:10.1029/2008JE003201.

Morris, R.V., G. Klingelhofer, C. Schroder, D.S. Rodionov, A. Yen, D.W. Ming, P.A. de Souza Jr., I. Fleischer, T. Wdowiak, R. Gellert, B. Bernhardt, E.N. Evlanov, B. Zubkov, J. Foh, U. Bonnes, E. Kankeleit, P. Gutlich, F. Renz, S.W. Squyres, and R.E. Arvidson (2006a), Mössbauer mineralogy of rock, soil, and dust at Gusev crater, Mars: Spirit's journey through weakly altered olivine basalt on the plains and pervasively altered basalt in the Columbia Hills, *J. Geophys. Res.*, *111*, doi:10.1029/2005JE002584.

Morris, R.V., G. Klingelhofer, C. Schroder, D.S. Rodionov, A. Yen, D.W. Ming, P.A. de Souza Jr., I. Fleischer, T. Wdowiak, R. Gellert, B. Bernhardt, U. Bonnes, B.A. Cohen, E.N. Evlanov, J. Foh, P. Gutlich, E. Kankeleit, T. McCoy, D.W. Mittlefehldt, F. Renz, M.E. Schmidt, B. Zubkov, S.W. Squyres, and R.E. Arvidson (2006b), Mössbauer mineralogy of rock, soil, and dust at Meridiani Planum, Mars: Opportunity's journey across sulfate-rich outcrop, basaltic sand and dust, and hematite lag deposits, *J. Geophys. Res.*, *111*, doi:10.1029/2006JE002791.

Murchie, S.L., R.E. Arvidson, P. Bedini, K. Beisser, J.-P. Bibring, J.L. Bishop, J. Boldt, P. Cavender, T. Choo, R.T. Clancy, E.H. Darlington, D. Des Marais, R. Espiritu, D. Fort, R.O. Green, E. Guinness, J. Hayes, C. Hash, K. Heffernan, J. Hemmler, G. Heyler, D. Humm, J. Hutcheson, N. Izenberg, R. Lee, J. Lees, D. Lohr, E. Malaret, T. Martin, J.A. McGovern, P. McGuire, R.V. Morris, J.F. Mustard, S. Pelkey, E. Rhodes, M. Robinson, T. Roush, E. Shaefer, G. Seagrave, F. Seelos, P. Silvergate, S. Slavney, M. Smith, W.J. Shyong, K. Strohbehn, H. Taylor, P. Thompson, B. Tossman, M. Wirzburger, and M. Wolff (2007), Compact Reconnaissance Imaging Spectrometer for Mars (CRISM) on Mars Reconnaissance Orbiter (MRO), *J. Geophys. Res.*, *112*, E05S03, doi:10.1029/2006JE002682.

Murchie, S.L., L.H. Roach, F.P. Seelos, R.E. Milliken, J.F. Mustard, R.E. Arvidson, S.M. Wiseman, K.A. Lichtenberg, J.C. Andrews-Hanna, J.-P. Bibring, J.L. Bishop, M. Parente, and R.V. Morris (2009), Evidence for the origin of layered deposits in Candor Chasma, Mars, from mineral composition and hydrologic modeling, *J. Geophys. Res.*, *114*, E00D05, doi:10.1029/2009JE003343.

Mustard, J.F., F. Poulet, A. Gendrin, J.-P. Bibring, Y. Langevin, B. Gondet, N. Mangold, G. Bellucci, and F. Altieri (2005), Olivine and pyroxene diversity in the crust of Mars, *Science*, *307*, 1594-1597, doi:10.1126/science.1109098.

Neukum, G., R. Jaumann, and t.H.C.-I. Team (2004), HRSC--The High Resolution Stereo Camera of Mars Express, *Special Publication SP-1240*, 17-35.

- Noe Dobrea, E.Z., F. Poulet, and M.C. Malin (2008), Correlations between hematite and sulfates in the chaotic terrain east of Valles Marineris, *Icarus*, 193, 516-534, doi:10.1016/j.icarus.2007.06.029.
- Nummedal, D., and D.B. Prior (1981), Generation of Martian chaos and channels by debris flows, *Icarus*, 45, 1, 77-86, doi:10.1016/0019-1035(81)90007-5.
- Oosthoek, J.H.P., T.E. Zegers, A. Rossi, B. Foing, G. Neukum, and the HRSC Co-Investigator Team (2007), 3D Mapping of Aram Chaos: A Record of Fracturing and Fluid Activity, *Lunar and Planetary Science Conference XXXVII*, Houston, Texas, Abstract # 1577.
- Pelkey, S.M., J.F. Mustard, S.L. Murchie, R.T. Clancy, M. Wolff, M. Smith, R.E. Milliken, J.-P. Bibring, A. Gendrin, F. Poulet, Y. Langevin, and B. Gondet (2007), CRISM multispectral summary products: Parameterizing mineral diversity in Mars from reflectance, *J. Geophys. Res.*, 112, E08S14, doi:10.1029/2006JE002831.
- Roach, L.H., J.F. Mustard, S.L. Murchie, J.-P. Bibring, F. Forget, K.W. Lewis, O. Aharonson, M. Vincendon, and J.L. Bishop (2009), Testing evidence of recent hydration state change in sulfates on Mars, *J. Geophys. Res.*, 114, E00D02, doi:10.1029/2008JE003245.
- Rodriguez, J.A.P., S. Sasaki, R.O. Kuzmin, J.M. Dohm, K.L. Tanaka, H. Miyamoto, K. Kurita, G. Komatsu, A.G. Fairen, and J.C. Ferris (2005), Outflow channel sources, reactivation, and chaos formation, Xanthe Terra, Mars, *Icarus*, 175, 36-57, doi:10.1016/j.icarus.2004.10.025.

- Smith, D.E., G.A. Neumann, R.E. Arvidson, E. Guinness, and S. Slavney (2003), Mars Global Surveyor Laser Altimeter Mission Experiment Gridded Data Record, pp. MGS-M-MOLA-5-MEGDR-L3-V1.0, NASA Planetary Data System.
- Smith, D.E., M.T. Zuber, H.V. Frey, J.B. Garvin, J.W. Head, D.O. Muhleman, G.H. Pettengil, R.J. Phillips, S.C. Solomon, H.J. Zwally, W.B. Banerdt, T.C. Duxbury, M. Golombek, F.G. Lemoine, G.A. Neumann, D.D. Rowlands, O. Aharonson, P.G. Ford, A.B. Ivanov, C.L. Johnson, P.J. McGovern, J.B. Abshire, R.S. Afzal, and X. Sun (2001), Mars Orbiter Laser Altimeter: Experiment summary after the first year of global mapping of Mars, *J. Geophys. Res.*, *106*, E10, 23689-23722, doi:10.1029/2000JE001364.
- Squyres, S.W., R.E. Arvidson, J.F. Bell III, J. Bruckner, N.A. Cabrol, W.M. Calvin, M.H. Carr, P.R. Christensen, B.C. Clark, L. Crumpler, D. Des Marais, D. d'Uston, T. Economou, J. Farmer, W.H. Farrand, W. Folkner, M. Golombek, S. Gorevan, J.A. Grant, R. Greeley, J.P. Grotzinger, L. Haskin, K.E. Herkenhoff, S. Hviid, J.R. Johnson, G. Klingelhofer, A.H. Knoll, G. Landis, M. Lemmon, R. Li, M.B. Madsen, M.C. Malin, S.M. McLennan, H.Y. McSween, D.W. Ming, J. Moersch, R.V. Morris, T. Parker, J.W. Rice Jr, L. Richter, R. Rieder, M. Sims, M. Smith, P. Smith, L.A. Soderblom, R.J. Sullivan, H. Wanke, T. Wdowiak, M. Wolff, and A. Yen (2004), The Opportunity Rover's Athena Science Investigation at Meridiani Planum, Mars, *Science*, *306*, 1698-1703, doi: 10.1126/science.1106171.
- Tosca, N.J., and S.M. McLennan (2006), Chemical divides and evaporite assemblages on Mars, *EPSL*, *241*, 21-31, doi:10.1016/j.epsl.2005.10.021.

Wang, A., and J.J. Freeman (2009), Pathways and rates of Mg-sulfate dehydration and rehydration on Mars, *Lunar and Planetary Science Conference XXXX*, Houston, TX.

Wiseman, S.M., R.E. Arvidson, R.V. Morris, F. Poulet, J.C. Andrews-Hanna, J.L.

Bishop, S.L. Murchie, F. Seelos, D. Des Marais, and J.L. Griffes (2009), Spectral and stratigraphic mapping of hydrated sulfate and phyllosilicate-bearing deposits in northern Sinus Meridiani, Mars, *J. Geophys. Res.*, *In Press*.

Kimberly A. Lichtenberg

Department of Earth and Planetary Sciences
Washington University in St. Louis
Campus Box 1169
St. Louis, MO 63130

(314) 935-8594 (work)
(314) 255-7252 (cell)
lichtenberg@wunder.wustl.edu

EDUCATION

B.S. 1998, University of Virginia (Engineering Science)
A.M. 2006, Washington University in St. Louis (Earth and Planetary Science)
Ph.D. 2010, Washington University in St. Louis (Earth and Planetary Science)

POSITIONS

Athena Student Collaborator, Mars Exploration Rover Mission, 2006-2010

Research Assistant, Washington University in St. Louis, 2005-2010

Teaching Assistant, Washington University in St. Louis, 2007

Teaching Assistant, Dartmouth College, 2003-2004

Systems Engineer, Johns Hopkins University Applied Physics Laboratory
Integration and Operations Group, Space Department, 2001-2002

- Administrator of the CONTOUR, MESSENGER, STEREO, and New Horizons Command and Telemetry Definition databases.
- Conducted 24-hour operational software tests on the CONTOUR spacecraft while in thermal/vacuum at NASA Goddard Space Flight Center and pre-flight at Kennedy Space Center.

Air Defense Systems Engineering Group, Air Defense Department, 1998-2001

- Conducted system-level analyses for the Navy Aegis Weapon System Sensor Integration project and predicted real-time ship performance against modeled threats using modeling and simulation tools
- Designed and administrated the Combat System Database

RESEARCH INTERESTS

1. Geology and surface properties of Mars using visible and near-infrared spectroscopy; in particular, reconnaissance, stratigraphy, and mapping of hydrated sulfates using multiple orbital data sets (CRISM, OMEGA, THEMIS, TES, CTX, HiRISE).
2. Automated terrain analysis and terramechanics modeling.

PUBLICATIONS AND PRESENTATIONS (selected)

Lichtenberg, K. A. et al. (2010) Stratigraphy of hydrated sulfates in the sedimentary deposits of Aram Chaos, Mars, *J. Geophys. Res.*, doi:10.1029/2009JE003353, in press.

Lichtenberg, K. A. et al (2009) Stratigraphy and relationship of hydrated minerals in the layered deposits of Aram Chaos, Mars, *40th Lunar and Planetary Science Conference*, Abstract #2326, Houston TX.

Morris, R. V. et al (as a contributing author) (2009) Visible and near-IR reflectance spectra for smectite, sulfate, and perchlorate under dry conditions for

- interpretation of Martian surface mineralogy, *40th Lunar and Planetary Science Conference*, Abstract #2317, Houston TX.
- Murchie, S. et al (as a contributing author) (2009) Evidence for the origin of layered deposits in Candor Chasma, Mars, from mineral composition and hydrologic modeling, *J. Geophys. Res.*, 114, E00D05, doi:10.1029/2009JE003343.
- McGuire, P. C. et al (as a contributing author) (2008) MRO/CRISM retrieval of surface lambert albedos for multispectral mapping of Mars with DISORT-based radiative transfer modeling: Phase I -- Using historical climatology for temperatures, aerosol optical depths, and atmospheric pressures, *IEEE Transactions on Geoscience and Remote Sensing*, Vol. 46(12), doi:10.1109/TGRS.2008.2000631.
- Lichtenberg, K. A.** et al. (2008) Structural and Geologic Relationships Between Igneous Rocks and their Alteration Products, *39th Lunar and Planetary Science Conference*, Abstract #1390, Houston TX.
- Roach, L. H., et al (as a contributing author) (2008) Sulfate Mineral Stratigraphy in Valles Marineris Interior Layered Deposits, *39th Lunar and Planetary Science Conference*, Abstract #1891, Houston TX.
- Lichtenberg, K. A.** et al. (2007), Coordinated analyses of orbital and Spirit Rover data to characterize surface materials on the cratered plains of Gusev Crater, Mars, *J. Geophys. Res.*, 112, E12S90, doi:10.1029/2006JE002850.
- Lichtenberg, K. A.** et al. (2007) Structural, Stratigraphic, and Mineralogic Mapping of Noachian and Hesperian Aged Crust in Xanthe Terra, Mars, *Eos Trans. AGU*, 88(52), Fall Meeting Supplement.
- Morris, R. V. et al. (as a contributing author) (2007) Initial Results from the MRO-CRISM Hyperspectral Imaging Spectrometer for the Columbia Hills in Gusev Crater on Mars, *38th Lunar and Planetary Science Conference*, Abstract #1469, Houston TX.
- Lichtenberg, K. A.**, W. B. McKinnon, and A. C. Barr (2006) Heat Flux from Impact Ring Graben on Europa, *37th Lunar and Planetary Science Conference*, Abstract #2399, Houston TX.
- Lichtenberg, K. A.** and L. J. Sonder (2004) Dynamics of block rotations in strike-slip fault zones; a perspective from distinct element modeling, *Eos Trans. AGU*, 85(47), Fall Meeting Supplement.

PROFESSIONAL ACTIVITIES AND SERVICE

- Co-chair, "Geochemistry, Stratigraphy, and Evolution of Sulfates on Mars", American Geophysical Union Fall Meeting, 2008
- Co-Head, Peer Mentors organization, Washington University EPSc Dept., 2007-2009
- Graduate Student Fellowship, McDonnell Center for the Space Sciences, 2004-2007
- JPL NASA Planetary Science Summer School, Pasadena, CA, 2007
- Presented on Venus Exploration to the NRC NOSSE committee, Oct. 2007
- Science outreach to local schools and organizations, St. Louis MO, 2004-present
- Professional societies:
 - American Geophysical Union
 - Geological Society of America
 - AAAS
 - Association of Women in Science